

Nanostructures based on graphene and functionalized carbon nanotubes

Grafén és szén nanocső alapú nanoszerkezetek előállítása és jellemzése

Nemes – Incze Péter



Eötvös Loránd Tudományegyetem – Természettudományi Kar

Fizika Doktori Iskola, vezetője: Prof. Dr. Csikor Ferenc

Anyagtudomány és Szilárdtestfizika Program, programvezető: Prof. Dr. Lendvai
János

Témavezető: Prof. Dr. Biró László Péter, DSc

Magyar Tudományos Akadémia Természettudományi Kutatóközpont

Műszaki Fizikai és Anyagtudományi Intézet

Table of contents

1. Introduction	5
1.1. Motivation	6
1.2. Discovery, physical properties and the importance of carbon nanostructures	7
1.2.1. The discovery of sp^2 carbon nanostructures	8
1.2.2. Electronic properties of graphene	10
1.2.3. Electronic properties of carbon nanotubes.....	15
1.3. Production of carbon nanotubes and graphene	19
1.3.1. Carbon nanotubes	19
1.3.2. Graphene.....	21
1.4. Tailoring the electronic properties of carbon nanotubes and graphene	23
1.4.1. Carbon nanotube functionalization.....	24
1.4.2. Graphene nanoribbons and other graphene nanostructures	27
1.4.3. Preparation of GNRs	32
2. Methods	35
2.1. Scanning tunneling microscopy	35
2.2. Atomic force microscopy	40
3. Results and Discussion	42
3.1. Mapping of functionalized sites on carbon nanotubes	42
3.1.1. Challenges in STM measurement of functionalized CNTs.....	43
3.1.2. Methods, sample preparation and initial characterization.....	44
3.1.3. Mapping of functionalized CNTs by CITS.....	48
3.2. Measurement artefacts in AFM imaging of graphene	54
3.2.1. Anomalous graphene thickness measurements.....	55
3.2.2. Experimental methods.....	56
3.2.3. Experimental investigation of the source of the artefacts.....	56
3.2.4. A model for the tip – surface interaction and measurement regimes	62

3.2.5.	Reproducible thickness measurements of FLG	70
3.3.	Preparing graphene nanoarchitectures with zigzag edges.....	74
3.3.1.	Sample preparation and experimental methods.....	75
3.3.2.	Controlled patterning of graphene.....	79
3.3.3.	Revealing the orientation of the etch pits	80
3.3.4.	Crystallinity and edge roughness.....	82
4.	Summary	88
5.	Thesis points	90
6.	List of publications	92
6.1.	Publications used to compose the thesis points.....	92
6.2.	Other publications.....	92
7.	Acknowledgements.....	95
References	95

Abbreviations:

ADC:	amplitude – distance curve
AFM:	atomic force microscope/microscopy
ATR-IR:	attenuated total reflectance infrared
CITS:	current imaging tunneling spectroscopy
CNT:	carbon nanotube
CVD:	chemical vapor deposition
DMT:	Derjaguin-Muller-Toporov (model)
DOS	density of states
FET:	field effect transistor
FLG:	few layer graphite
GNR:	graphene nanoribbon
HOPG:	highly ordered pyrolytic graphite
LDOS:	local density of states
MWCNT:	multiwall carbon nanotube
SEM	scanning electron microscope/microscopy
STM:	scanning tunneling microscope/microscopy
STS:	scanning tunneling spectroscopy
SWCNT:	single walled carbon nanotube
TAFM:	tapping mode AFM
TEM:	transmission electron microscopy

1. Introduction

Throughout human history, technology and the gathering of scientific knowledge seems to have progressed in a more or less exponential, self enhancing manner. This has certainly been true after the enlightenment when in the western world, the gain in scientific knowledge and technological mastery that has been enabled by it has spurred on the development of the natural sciences, this itself helping to create new technologies to better exploit our resources and create new opportunities. From the early days of cross ocean ship travel, through the industrial revolution in the latter part of the XVIIIth century to the internet age, the frequency of technological revolutions has increased and will likely increase further through the XXIst century, global resources permitting. Today, we stand at the beginning of what looks like another scientific and technological revolution: the age of nanotechnology. This holds the promise of enabling us to manipulate materials at the nanometer scale, resulting in tools and technologies never dreamt of in earlier centuries, from nanoparticle based cancer therapy [1] to high performance composites [2, 3], nanotechnology opens up new frontiers for innovation in medicine, electronics, materials, etc. [4].

A leading thread in the unfolding story of nanotechnology are carbon nanostructures, the discovery and research of which has significantly contributed to shaping the route that science at the nanoscale has taken. These carbon nanostructures include: fullerenes, carbon nanotubes and recently prepared single layers of graphite: graphene [5]. All of these nanostructures are composed entirely of sp^2 hybridized carbon atoms forming various structures, from the soccer ball like fullerene (C_{60}) to the single atom thick plane of carbon called graphene, to the “rolled up”, tubular sheets of graphene: carbon nanotubes (see Figure 1). The physical properties of these materials, although all of them being composed of sp^2 carbon, are as varied as their atomic structure. From the earliest theoretical investigation in the 40's into the electronic properties of graphene and graphite, it became ever clearer that graphite has some unusual properties, for example a difference of around 100 in the in plane and out of plane electrical conductivity [6]. Later, more and more properties of graphite, graphene and CNT have come to light, for example the high charge carrier mobility of graphene and carbon nanotubes [7, 8, 9], exceptional mechanical properties, such as a

Young's modulus higher than 1 TPa [10] for CNTs and similar values for graphene [11], the soccer ball-like cage structure of the C_{60} fullerene, etc. With the discovery of more and more of their exotic properties the incentive for further research and the promise of practical applications of these materials became ever greater.

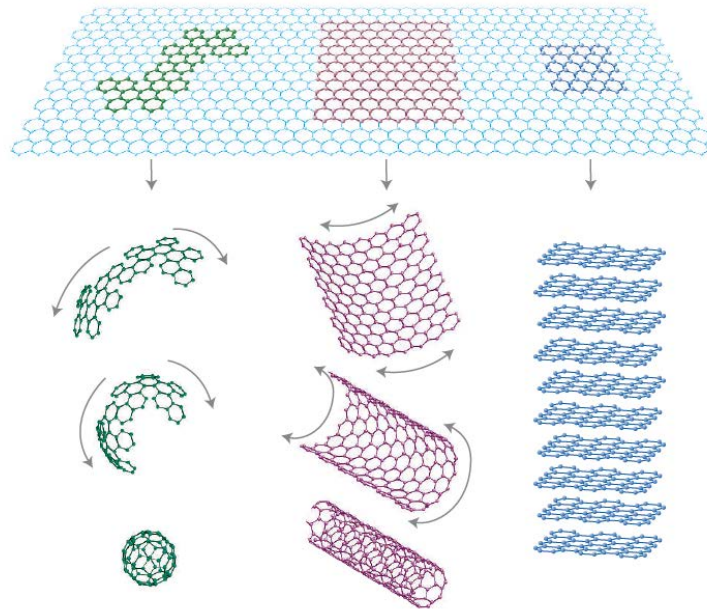


Figure 1. (from left to right) A C_{60} fullerene molecule, a carbon nanotube and graphite. Graphene, a single sheet of graphite, can be considered as a building block of all these carbon structures. Image reproduced from ref 12.

The evolution of the research into carbon nanostructures has also shown a self enhancing character, in part due to the highly interconnected character of this field of research and the fact that experts and research groups in the field work on various carbon nanostructures simultaneously. This way the discovery of fullerenes in 1985 [13] paved the way and provided the context for the discovery of carbon nanotubes [14] and later the discovery of graphene [5, 15]. In the following chapters I will briefly describe the evolution of this field of research, the physical properties of these carbon nanostructures, in order to provide an overall picture of the research field and to place my own results into context.

1.1. Motivation

The challenges of nanotechnology and of carbon nanostructure research in particular can be addressed on two fronts, one of them being the preparation of nanostructures, the other the investigation of their physical properties. In order to explore and harness the rich physics

of graphene and carbon nanotubes, new methods are required to tailor their properties and current methods of sample investigation need to be adapted. This thesis is a contribution to the advancement of both of these goals, through the following studies:

- Exploring a novel route of nanostructuring sheets of graphene in a crystallographically selective manner.
- Introducing a sample preparation technique that solves the sample stability issues plaguing the scanning tunneling microscopy investigation of functionalized carbon nanotubes.
- Investigating the anomalous and sometimes contradictory size measurements of graphene by the dynamic atomic force microscopy method.

In the introductory chapters the physical properties of graphene, carbon nanotubes and functionalized carbon nanotubes will be presented, as well as relevant experimental investigation methods. I will delve into the challenges faced in the investigation of the above three topics and the answers I was able to give to them during my research.

1.2. Discovery, physical properties and the importance of carbon nanostructures

Carbon in the form of coal has been the driving force of the industrial revolution. Today, carbon nanostructures are a significant part of another technological and scientific revolution: nanotechnology. Fibrous carbon materials are already part of everyday life in the form of carbon fiber reinforced composites [16]. During the 1960s and 1970s carbon fibers have started out on the road to becoming an important industrial material [16, 17] and today they have found uses from sports equipment to vehicle parts, anywhere where low weight and high strength is required. Carbon nanotubes and graphene promise even greater benefits if their extraordinary properties could be harnessed.

In the following sections an introduction to the physical properties of carbon nanotubes and graphene will be given. Since the electronic properties of carbon nanotubes can be derived from that of graphene I will discuss the properties of graphene first.

1.2.1. The discovery of sp^2 carbon nanostructures

The successful isolation of graphene came in a time when research into other forms of carbon nanostructures, namely fullerenes and carbon nanotubes was already a well established field of research (see publication data in Figure 2). This fact helped spur on the rapid development of graphene research.

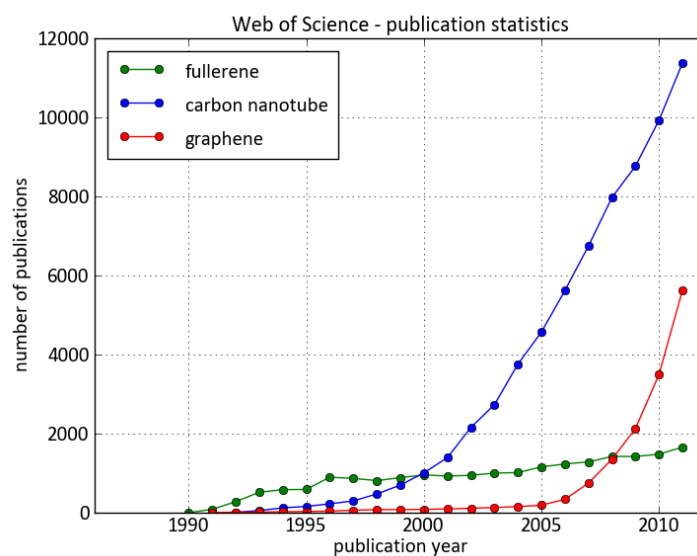


Figure 2. Publication data from Web of Science (Thomson - Reuters) database.

The discovery of fullerenes in 1985, was purely by chance, a typical case of a scientist setting out to explore a particular problem and in the process stumbling on something completely unexpected. Researchers at Rice University were investigating the formation of carbon chains in interstellar space, by using a laser beam to evaporate graphite targets [13]. In the beam formed by the vaporized carbon species, they have found a remarkably stable carbon cluster, consisting of 60 carbon atoms. They have proposed a truncated icosahedron structure (similar to a soccer ball) which later turned out to be the correct structure of this molecule. Curiously, later research has revealed that fullerenes actually exist in interstellar space [18].

Not a decade has passed after the discovery of fullerenes and carbon nanotubes have entered the scientific stage in 1991, when Sumio Iijima published transmission electron microscopy (TEM) images of cylindrical graphitic carbon structures. This publication has sparked the imagination of a scientific community already involved in the research of

fullerenes, eager to look into the properties of “buckytubes” [19]. It is worth mentioning at this point that even though the research into carbon nanotubes has been kicked off in the early 90s, following the paper of Iijima, TEM images of carbon nanostructures very similar to nanotubes have been reported as early as 1952 [20], though their importance was not recognized at that time. In the years following the discovery of Iijima, the properties of carbon nanotubes have come to light: extraordinary charge carrier mobility, with a band gap dependent on the specific ordering of carbon atoms in the nanotube, Young’s modulus and tensile strength in the 1 TPa and 200 GPa range respectively, the maximal supported electrical current density is $>10^9$ A/cm² (~100 times greater than for copper wires) [21, 22, 23], etc. The fact that a lot of these properties are dependent on the chirality, seemed at first to be an exciting benefit of CNT, but it has later turned out to be an hindrance to their application. The task of producing samples containing CNT of a specific chirality has proven to be a difficult endeavor [24]. Furthermore, separating the different chiralities from one another has only recently shown some success, with the ability to enrich a sample in semiconducting or metallic nanotubes [24, 25]. This ability to synthesize or to produce CNT with a particular chirality is needed to obtain any useful application which is based on the electronic or optical properties of the nanotubes [24]. In this respect, graphene looks promising because various methods present themselves to tailor its electronic properties [26, 27, 28], with a novel procedure being one of the main subjects of the present thesis. In the case of carbon nanotubes, various forms of chemical doping and addition of functional groups offer a way to tailor their electronic properties to a certain degree. I will give a brief description of these methods in the following sections.

Graphene as a thin film grown on metallic substrates has been obtained and studied since the 1970s when Blakely and colleagues reported single layer graphite growth on various transition-metal substrates [29, 30, 31]. Even before these experiments, the separation of the graphene layers in graphite in the form of graphite intercalation compounds, exfoliated graphite and so called graphene oxide has been studied [32, 33]. The term graphene was proposed by Boehm et al. in 1986 to describe a single atomic sheet of graphite [34]. However during this time it was thought that graphene cannot exist outside of a 3D crystalline matrix, much like monolayers of atomic species grown as thin films [35]. Later this thinking was proven wrong by Novoselov and Geim. In 2004 their research group has

prepared single atomic layers of graphene by mechanical exfoliation from bulk graphite [5]. This method produces samples of very high crystallinity and purity, which makes possible the exploration of the very specific transport properties of graphene. Following this discovery, Novoselov et al. [36, 37], Zhang et al. [38] and Berger et al. [39] have shown that graphene has very unique properties, not found in bulk graphite.

1.2.2. Electronic properties of graphene

Graphene consists of carbon atoms arranged in a honeycomb lattice having two atoms in the unit cell (see Figure 3). These two atoms make up two non-equivalent sublattices in graphene, the atoms forming the trigonal σ bonds with each other, with an interatomic nearest neighbor separation of $a_{cc} = 1.42 \text{ \AA}$. The σ bonding sp^2 orbitals are formed by the superposition of the s , p_x and p_y orbitals of atomic carbon leaving the p_z orbital unhybridized. The geometry of the hybridized orbital is trigonal planar. This is the reason why each carbon atom within graphite has three nearest neighbors in the graphite sheet. The p_z -orbitals of neighboring carbon atoms overlap and form the distributed π -bonds that reside above and below each graphite sheet. This leads to the delocalized electron π bands, much like in the case of benzene, naphthalene, anthracene and other aromatic molecules. In this regard graphene can be thought of as the extreme size limit of planar aromatic molecules. Covalent σ bonds are largely responsible for the mechanical strength of graphene and other sp^2 carbon allotropes. The σ electronic bands are completely filled and have a large separation in energy from the π bands and thus their effects on the electronic behavior of graphene can be neglected in a first approximation. It needs to be mentioned that in a real sample the graphene layer is not strictly a 2D crystal, as it becomes rippled when suspended [40] or adheres to the corrugation of its supporting substrate [41]. In such a situation a mixing of the σ and π orbitals occurs, which may have to be taken into consideration when calculating the electronic properties of graphene [42, 43].

One of the simplest evaluations of the band structure and therefore the electronic properties of graphene can be given by examining the π bands in a tight binding approximation. The first account of this band structure calculation was given by Wallace in 1947 [6]. The lattice vectors forming the basis of the unit cell are: $\vec{a}_1 = a/2(3, \sqrt{3})$ and

$\vec{a}_2 = a/2(3, -\sqrt{3})$, while the reciprocal lattice vectors can be written as: $\vec{b}_1 = 2\pi/3a(1, \sqrt{3})$ and $\vec{b}_2 = 2\pi/3a(1, -\sqrt{3})$. Here a is the nearest neighbor interatomic distance: 1.42 Å.

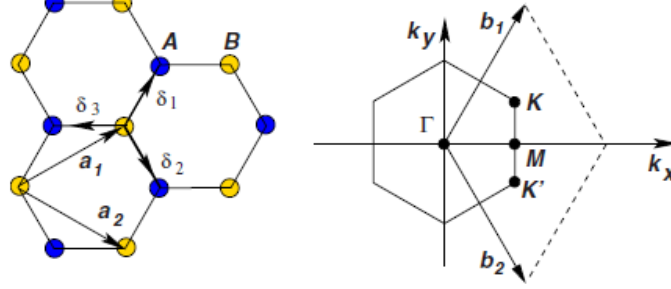


Figure 3. The honeycomb lattice of graphene showing the two sublattices marked A and B and the first Brillouin zone of graphene marking some of the high symmetry points Γ , M, K and K' . (Image reproduced from ref. 44)

Each non equivalent carbon atom in the unit cell donates one p_z electron to the lattice, thus when writing the wave function, this becomes a linear combination of the p_z electron wavefunctions originating in sites A and B within the unit cell (ϕ_A, ϕ_B):

$$(I). \quad \psi_{\vec{k}}(\vec{r}) = \frac{1}{\sqrt{N}} \sum_{\vec{R}} [\phi_A(\vec{k})\phi_A(\vec{r} - \vec{R}) + \phi_B(\vec{k})\phi_B(\vec{r} - \vec{R} - \vec{d})] e^{i\vec{k}\vec{R}},$$

$$\vec{d} = (\vec{a}_1 + \vec{a}_2)/3$$

with ϕ_A and ϕ_B the coefficients needed to be determined and N the number of unit cells.

Using this wave function in the Schrödinger equation $\hat{H}\psi_{\vec{k}}(\vec{r}) = E(\vec{k})\psi_{\vec{k}}(\vec{r})$ and writing it in matrix form, we obtain:

$$(II). \quad H \begin{bmatrix} \phi_A \\ \phi_B \end{bmatrix} = E(\vec{k})S \begin{bmatrix} \phi_A \\ \phi_B \end{bmatrix}, \text{ where } H = \begin{bmatrix} H_{AA} & H_{AB} \\ H_{AB}^* & H_{AA} \end{bmatrix} \text{ and } S = \begin{bmatrix} S_{AA} & S_{AB} \\ S_{AB}^* & S_{AA} \end{bmatrix}$$

We can determine the eigenvalues of this equation from:

$$(III). \quad \det \begin{bmatrix} H_{AA} - S_{AA}E(\vec{k}) & H_{AB} - S_{AB}E(\vec{k}) \\ H_{AB}^* - E(\vec{k})S_{AB}^* & H_{AA} - S_{AA}E(\vec{k}) \end{bmatrix} = 0$$

$$E^\pm(\vec{k}) = \frac{2E_0 - E_1 \pm \sqrt{(E_1 - 2E_0)^2 - 4E_2E_3}}{2E_3}$$

where $E_0 = H_{AA}S_{AA}$, $E_1 = S_{AB}H_{AB}^* + H_{AB}S_{AB}^*$, $E_2 = H_{AA}^2 - H_{AB}H_{AB}^*$ and $E_3 = S_{AA}^2 - S_{AB}S_{AB}^*$.

A fairly simple treatment and one that which gives a good approximation of the band structure calculated from first principles [45], is if we consider a first nearest neighbor interaction, not neglecting the overlap matrix elements S . The diagonal elements of the Hamiltonian are $H_{AA} = \varepsilon_0$, while the off diagonal elements $H_{AB} = \gamma_0 \left(1 + \exp(-i\vec{k}\vec{a}_1) + \exp(-i\vec{k}\vec{a}_2)\right)$. Similarly, the elements of the overlap matrix elements, assuming the atomic wave functions to be normalized, are: $S_{AA} = 1$, $S_{AB} = s_0 \left(1 + \exp(-i\vec{k}\vec{a}_1) + \exp(-i\vec{k}\vec{a}_2)\right)$. The values of the onsite energy $\varepsilon_0 = \langle \varphi_A | \hat{H} | \varphi_A \rangle$, the nearest neighbor hopping integral $\gamma_0 = \langle \varphi_A | \hat{H} | \varphi_B \rangle$ and $s_0 = \langle \varphi_A | \varphi_B \rangle$ can be used as fitting parameters or can be calculated starting from first principles. Using these expressions the eigenvalues become:

$$(IV). \quad E^\pm(\vec{k}) = \frac{\varepsilon_0 \pm \gamma_0 \sqrt{f(\vec{k})}}{1 \pm s_0 \sqrt{f(\vec{k})}}$$

where $f(\vec{k}) = 3 + 2 \cos \vec{k}\vec{a}_1 + 2 \cos \vec{k}\vec{a}_2 + 2 \cos \vec{k}(a_1 - a_2)$.

The 2D nature of graphene allows us to plot the $E(\vec{k})$ relationship in the whole first Brillouin zone (Figure 4). Curiously in the case of graphene the bottom of the conduction band and the top of the valence band is not at the Γ point as is the case with a lot of metals and semiconductors, but at another high symmetry point at the boundary of the first Brillouin zone, at the so called K points (see Figure 4). Here the valence and conduction bands meet, but do not overlap, with zero number of states just at the K points themselves. Because of this, graphene is called a zero band gap semiconductor or semimetal. The first Brillouin zone contains two non equivalent K points called K and K'. In the vicinity of these points the $E(\vec{k})$ relationship becomes linear (see Figure 4c), which has significant consequences for the electronic transport and optical properties of graphene.

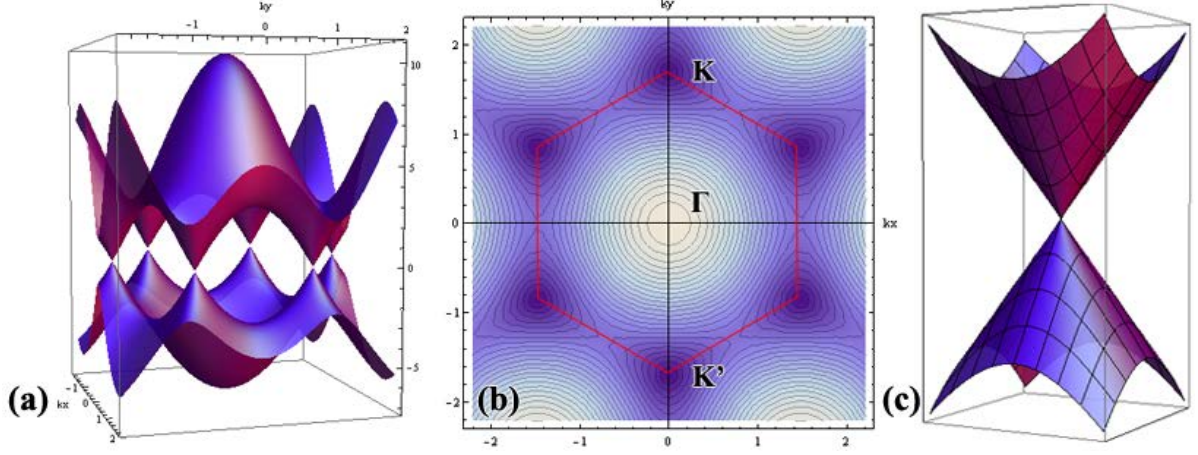


Figure 4. (a) The $E(k)$ relationship and (b) contour plot of the energy ($E^-(\vec{k})$) of graphene in the first Brillouin zone (red hexagon) setting $\epsilon_0=0$. The parameters used were: $\gamma_0=-2.84$ eV and $s_0 = 0.07$ [45]; the Fermi energy is at 0. The valence and conduction bands touch at the six K points or valleys. (c) The energy around the K and K' points has a linear dependence on \vec{k} .

Taking the first order expansion of the off diagonal elements of the Hamiltonian around the K point, we find that $H_{AB} \cong \hbar v_F (k_x + ik_y)$, while around the K' point $H'_{AB} \cong \hbar v_F (k_x - ik_y)$, v_F being the Fermi velocity. This way the energy eigenvalues for states around K can be obtained from:

$$(V). \quad \hbar v_F \begin{bmatrix} 0 & k_x + ik_y \\ k_x - ik_y & 0 \end{bmatrix} \begin{bmatrix} \phi_A \\ \phi_B \end{bmatrix} = E \begin{bmatrix} \phi_A \\ \phi_B \end{bmatrix},$$

while around the K' point we have:

$$(VI). \quad \hbar v_F \begin{bmatrix} 0 & k_x - ik_y \\ k_x + ik_y & 0 \end{bmatrix} \begin{bmatrix} \phi'_A \\ \phi'_B \end{bmatrix} = E \begin{bmatrix} \phi'_A \\ \phi'_B \end{bmatrix},$$

where ϕ_A , ϕ_B and ϕ'_A , ϕ'_B are the wave function amplitudes around K and K' points respectively. The above two equations bear a striking resemblance to the Dirac equation in which the mass of the particle and the z component of the momentum is set to zero, this is why the K points are sometimes referred to as “Dirac points”. These equations can be written in a more concise form using the Pauli matrices $\vec{\sigma} = (\sigma_x, \sigma_y)$ and the momentum operator $\vec{p} = -i\hbar(\partial/\partial x, \partial/\partial y)$ as: $v_F \vec{p} \cdot \vec{\sigma} \Phi = E \Phi$. The operator $v_F \vec{p} \cdot \vec{\sigma}$ acts on the two

component spinor $\Phi = (\phi_A, \phi_B)$ made up of the wave function amplitudes of the A and B sublattices. From a mathematical perspective the states A and B behave like spins, but have nothing to do with the spin state of the electrons, they are a kind of valley degree of freedom called pseudospin [46] or isospin [47]. Taking the states from both the K and K' valleys we can construct the full four dimensional Dirac equation:

$$(VII). \quad \begin{bmatrix} v_F \vec{p} \cdot \vec{\sigma} & 0 \\ 0 & v_F \vec{p} \cdot \vec{\sigma} \end{bmatrix} \begin{bmatrix} \Phi \\ \Phi' \end{bmatrix} = E \begin{bmatrix} \Phi \\ \Phi' \end{bmatrix}$$

It has been suggested that this extra degree of freedom could be utilized much like the real spin of the charge carriers in spintronics, in a kind of valley-tronics, where one could confine the charge carriers to a specific valley [48]. This limit of the graphene bands was discussed and was well known before the discovery of graphene [49], and is the starting point for theoretical investigations into the low energy excitations of graphene. It is important to note here, that the above Dirac equation holds for massless $\frac{1}{2}$ spin particles, which means that at low energies the electrons (and holes) in graphene have zero effective mass and travel at the “speed of light” the analogue of which is the Fermi velocity v_F . The energy around the K points can be written as $E = \hbar v_F |\vec{k}|$. This linear $E(\vec{k})$ dependence is a hallmark of graphene and is in stark contrast to the behavior of electrons near the band edges in most semiconductors, which if expressed in an effective mass approximation yields a quadratic relationship: $E(k) \approx \hbar^2 k^2 / 2m_{eff}$.

This Dirac physics of the charge carriers is the root cause of a lot of interesting physics observed in graphene. Starting from the very first observation of an anomalous, so called half integer, quantum Hall effect in graphene [37, 38] where the sequence of steps in the Hall conductivity is shifted with $\frac{1}{2}$, with respect to the classical quantum Hall effect. Another consequence of the gapless linear bands is the peculiar scattering properties of the charge carriers, which for certain incidence angles on electrostatic potential barriers can have a transmission probability of 1 [46]. This, so called Klein tunneling makes for the charge carriers in graphene to be unhindered by electrostatic potentials that vary smoothly on the atomic scale and that localization to be very weak in graphene [37]. The massless Dirac quasiparticles also affect the optical behavior of graphene, one interesting consequence

being, the almost constant absorption of light, in the visual frequency range, equal to $\pi\alpha$, α being the fine structure constant, so roughly $3.14/137$ [50]. Perhaps the most interesting aspect of graphene physics is that the band structure and physical properties of this material may be influenced by nanostructuring, functionalizing, mechanically straining, etc., yielding rich new physics to be studied and exploited [8, 12, 84].

1.2.3. Electronic properties of carbon nanotubes

As their name implies, CNTs are tubular nanostructures and can be thought of as sheets of graphene rolled up along a specific crystallographic direction (Figure 1). We can define a chiral vector (\vec{C}_h), which characterizes this specific wrapping of the nanotube (see Figure 5). This vector can be expressed as a linear combination of the basis vectors $\vec{C}_h = n\vec{a}_1 + m\vec{a}_2$, where n and m are integers. The structure of CNTs can be described by these two indices. For example, the diameter of the nanotube is just the length of C_h divided by π . As a function of the wrapping direction of the nanotubes two special circumstances are sometimes considered. One is when both n and m are equal, the other when n or m is zero, these two special cases are called armchair and zigzag nanotubes. The names themselves result from the special arrangement of carbon atoms along the nanotube circumference (Figure 5). The zigzag and armchair type nanotubes are sometimes referred to as achiral, while the nanotubes with any other chirality are called chiral.

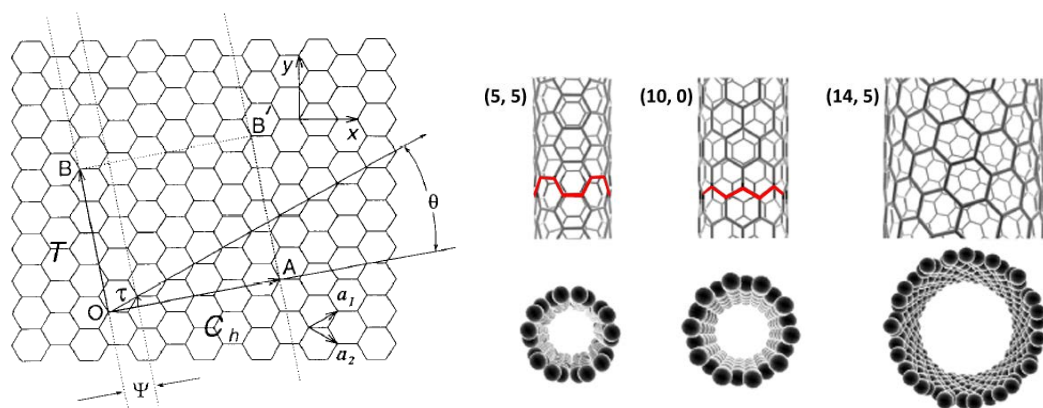


Figure 5. Scheme depicting how the wrapping direction influences the structure of carbon nanotubes. Reproduced from ref. 51. Sometimes the wrapping of the nanotube is described by the angle Θ . Examples of nanotubes having different chiral vectors.

The values of n and m have significant consequences regarding the electronic properties of CNTs. This was first predicted by Saito et al. closely after the discovery of CNTs [52, 53] and later directly measured, using scanning tunneling microscopy (STM) by Wildöer et al. [54]. They have shown that the band structure of SWCNTs is determined entirely by the specific chiral vector (\vec{C}_h) of the nanotube in question. They have found that depending on the choice of this vector the $1/3^{\text{rd}}$ of the nanotubes are metallic and $2/3^{\text{rd}}$ of them are semiconducting. Armchair nanotubes are always metallic, while other chiralities can be metallic or semiconducting. The band structure of CNTs can be deduced from that of graphene and the dependence on the chiral indexes can be explained by considering the boundary conditions imposed on the charge carriers in graphene. As a consequence of the tubular structure, only certain \vec{k} states can exist along the circumference of the nanotube. Thus, by “rolling up” a graphene sheet, a periodic boundary condition is imposed on the charge carriers in the direction of \vec{C}_h . This can be visualized by considering that only the states which have a phase of a multiple of 2π can exist along the tube circumference. This condition can be expressed as the quantization relation $\vec{C}_h \cdot \vec{k} = 2\pi q$, where q is an integer. It is interesting that in the case of CNTs the periodic boundary condition of solid state physics has a very exact physical meaning. Contrary to the circumferential direction there is no constraint on the states along the nanotube axis.

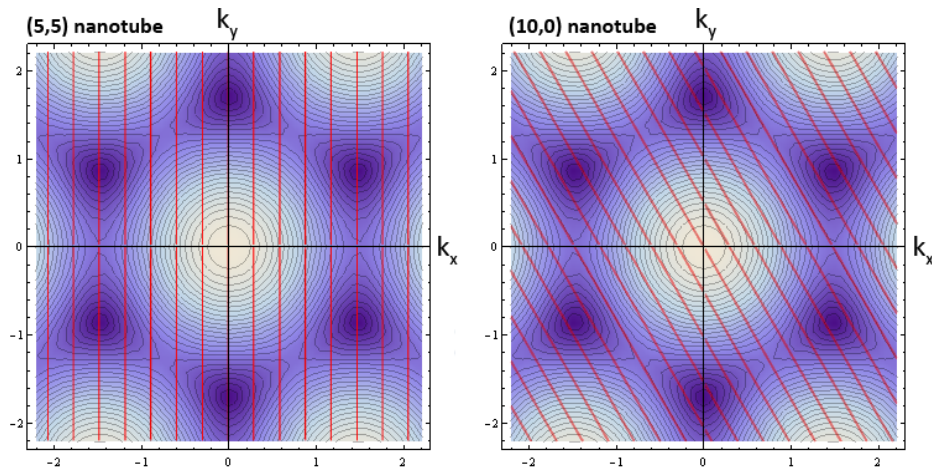


Figure 6. Contour plot of the $E(\vec{k})$ relationship of graphene showing the cutting lines (red) imposed by the periodic boundary condition, turning the 2D graphene system into a 1D CNT. The examples shown here are for a (5,5) metallic and a (10,0) semiconducting nanotube.

Thus, the band structure of CNTs is derived from that of graphene, plus the boundary condition. This results in the quantization of the graphene states shown in Figure 6, with red lines showing the allowed states. For a (5,5) nanotube the K points fall on the red lines, meaning that it has states around the Fermi level. In the case of the (10,0) nanotube, none of the allowed K points cross the allowed states, resulting in a band gap. The nanotube bands can be calculated using this so called zone folding method [52] in the tight binding approximation [55]. These bands are plotted in Figure 7 for both nanotubes.

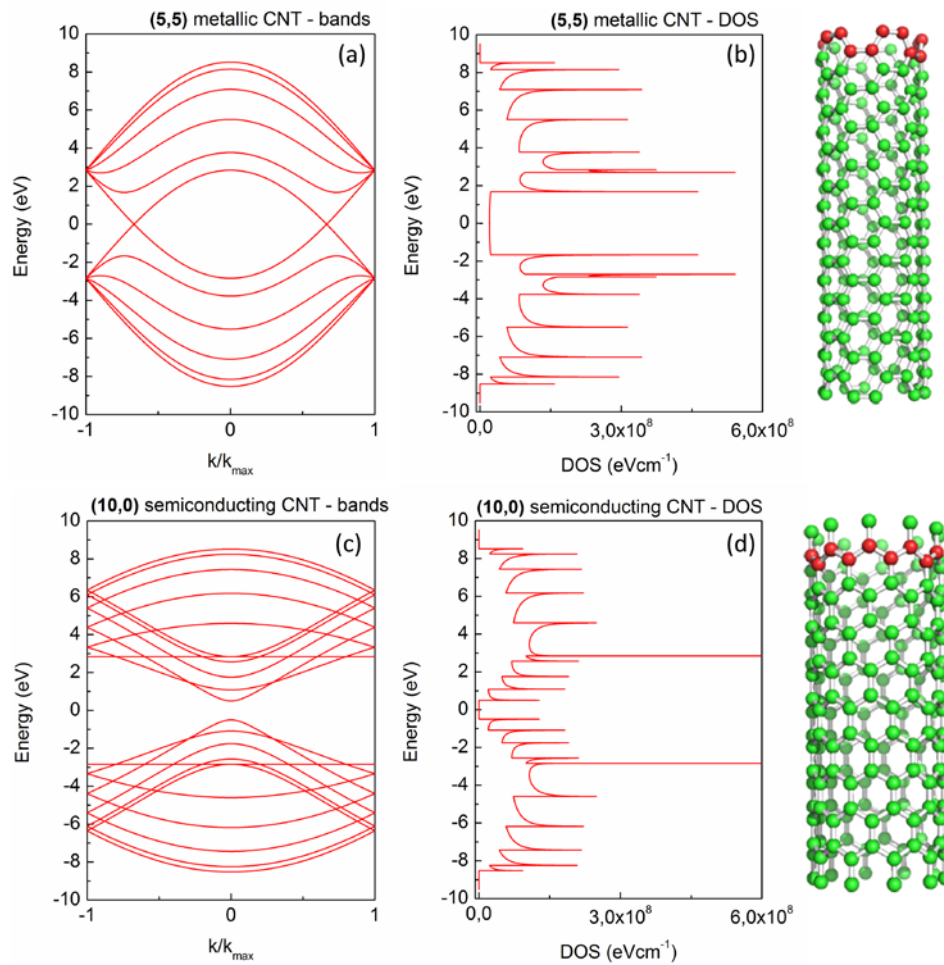


Figure 7. Bands and density of states (DOS) for a (5,5) metallic (a, b) and a (10,0) semiconducting nanotube (c, d), calculated using the tight binding approximation for $s_0 = 0$ [55]. The bands are plotted along the \vec{k} vector parallel to the tube axis. The (10,0) semiconducting nanotube has a band gap of roughly 1 eV. Van Hove singularities appear in the DOS, at the minimum and maximum points of the tube bands. The structural model of the (5,5) armchair (top) and (10,0) zigzag (bottom) nanotubes can be seen on the right.

A general rule is that a nanotube is metallic if the chiral indexes n and m obey the following relation: $2n + m = 3p$, where p is an integer [52]. In the case of semiconducting nanotubes,

the band gap scales inversely with the tube diameter: $E_{gap} = (2/\sqrt{3})\gamma_0 a / d_t$, where d_t is the CNT diameter. The density of states of nanotubes shows a series of sharp peaks, so called Van Hove singularities [56]. These peaks determine the charge transport properties and the transitions between these states, the optical properties of CNTs [57].

The simple picture used above to describe the band structure can be further refined by taking into account the curvature of the nanotubes, where the mixing of the sp and π bonds modifies the above description. This effect is significant in the case of small diameter nanotubes [58, 59].

Another type of nanotube, are the so called multiwalled CNTs (MWCNT). In the case of a MWCNT individual, concentric graphene tubes are stacked one into the other (Figure 8).

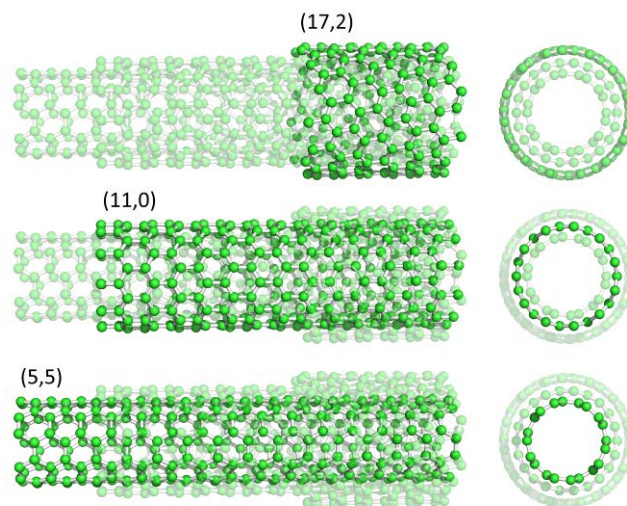


Figure 8. A multiwalled carbon nanotube composed of single walled tubes of different chiralities. The interlayer spacing of the nanotubes is roughly the same as the layer to layer spacing of graphite. (Image rendered using nanohub.org [55])

It was MWCNTs that were described in the landmark paper by Iijima [14], using TEM to reveal the structure of these tubes (Figure 9). The discovery of SWCNTs came later in 1993 by two teams publishing in the same issue of the journal Nature [60, 61]. The interlayer spacing between the concentric nanotube shells is slightly larger than the interlayer spacing in graphite: 0.335 nm and its exact value depends on the chiral indices of the individual tubes forming the MWCNT, having an average value of 0.339 nm [62]. Another important feature of MWCNTs is that while SWCNTs can have diameters of only up to 2 nm,

multiwalled tubes can have diameters in the range of tens of nanometers and in some cases even more than 100 nm [63, 64]. Since graphite can be considered a MWCNT of infinite diameter, such very large diameter nanotubes behave much like graphite under certain circumstances.

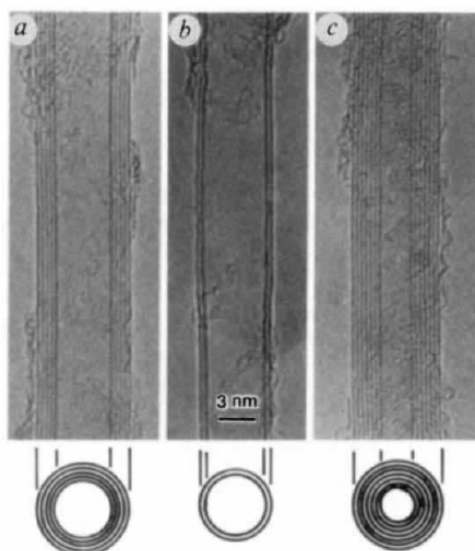


Figure 9. Transmission electron microscopy (TEM) image of MWCNTs published by S. Iijima. The individual nanotube walls can be resolved by electron microscopy. Reproduced from ref. [14]

1.3. Production of carbon nanotubes and graphene

1.3.1. Carbon nanotubes

The method used by Iijima [14] and adopted by other early investigators was that of arc discharge between two graphite electrodes in an inert atmosphere [14, 60, 65, 66, 68]. To prepare SWCNTs, the graphite electrodes are loaded with a metallic catalyst (Fe, Co, Ni, Y, Mo) and in the high temperature plasma that forms in the electric arc, the graphite electrodes are vaporized along with the catalyst and the carbon condenses in the form of nanotubes. In later years the laser ablation method used to produce fullerenes [13] was adapted for the production of CNTs, mostly SWCNT [65, 66]. Successful as these methods may be, none of them can be used to produce CNTs in the large scales required by the modern CNT industry. The breakthrough technique that enabled CNTs to become an industrial material was a route that involved chemical vapor deposition (CVD).

The catalytic decomposition of hydrocarbons was used well before the discovery of CNTs for the production of certain kinds of carbon fiber [67] and it was Yakaman et al. that successfully used this technique to obtain CNTs [68]. This synthesis route makes possible the production of CNTs in a continuous manner and enables a kind of control over the nanotube parameters that other techniques do not offer [23, 69, 70, 71], including: the patterned growth of nanotubes [72]; the growth of centimeter long nanotubes [73]; doped CNTs [74], etc. Since CVD was used to prepare the nanotubes investigated in this work, I will introduce this method in more detail.

CVD growth involves the use of a transition metal nanoparticles as catalyst (usually Fe, Ni, Co, Mo) either in the pure form or as an alloy [75, 76]. This catalyst is introduced into a furnace as a metal-organic precursor or supported on a substrate in the form of metallic nanoparticles and heated to a temperature in the range of 500°C to 1200°C [77]. Carbon nanotube synthesis begins on the nanoparticles if a suitable source of carbon is introduced. The carbon source is usually a hydrocarbon (methane, ethane, ethanol, benzene, etc) or CO as in the case of the HiPCO method [78]. The hydrocarbon gas is catalytically decomposed at the metallic nanoparticles, it diffuses through the bulk or surface of the nanoparticle finally forming graphitic shells. The graphitic material precipitating on the catalyst nanoparticle follows the morphology of the particle, forming the graphitic cylinders of single- or multiwalled nanotubes (Figure 10).

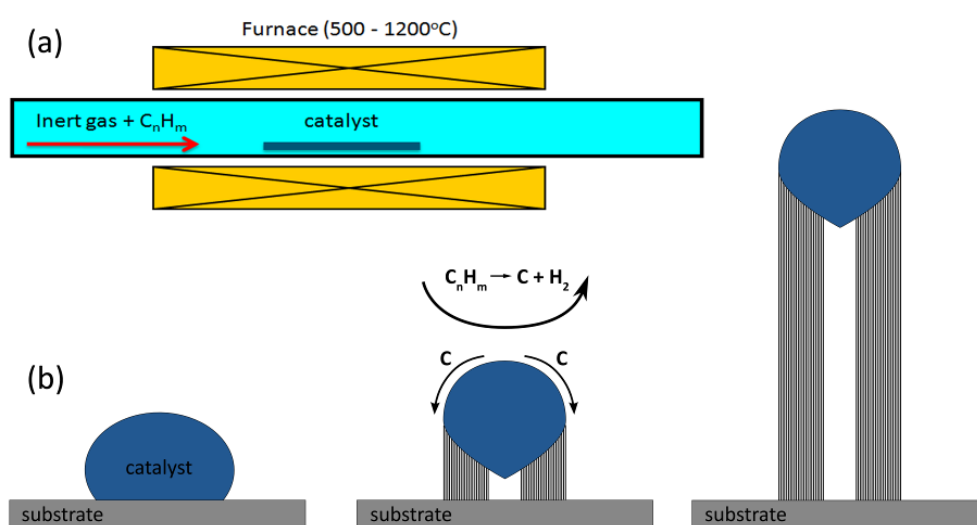


Figure 10. (a) Schematic of the CVD nanotube growth process. (b) The role of metallic nanoparticles during MWCNT growth.

The reaction mechanism briefly described above is much more complex and is still not completely understood [77]. The complete process involves the subtle interplay between nanoparticle dynamics, surface and bulk diffusion of carbon and the energetics of the metal surface – graphene – gas phase system.

1.3.2. Graphene

The method by which single layer graphene flakes were isolated from bulk graphite for the first time is still the most widely used technique to obtain graphene layers for research purposes. In 2004 Novoselov et al. used ordinary “scotch” tape to peel off layers of graphite from HOPG, a highly crystalline form of graphite produced synthetically [5]. This so called micromechanical cleaving technique consists of repeated peeling of the graphite crystallites stuck to the scotch tape, during which ever thinner crystals are produced on the tape surface. The graphite crystals separate very easily because the individual graphene planes in graphite are bound only by weak Van der Waals forces. After peeling, the tape is pressed against the surface of a silicon wafer having either a 90 or 300 nm of SiO₂ capping layer. While the tape is removed from the surface of the wafer the crystallites sticking to the SiO₂ surface cleave one last time and the result is an assortment of graphite crystals with varying thicknesses on the SiO₂ (Figure 11b). One of the most important factors that enabled the discovery of single layer graphite among these crystallites is that even graphene, not to mention bilayer graphene, can be seen with a conventional optical microscope on top of a wafer with carefully chosen SiO₂ thickness. This effect arises because graphene has a certain opacity and it also adds to the optical path of the light traversing the SiO₂ capping layer [79]. Together, these effects are enough to give graphene a well discernible contrast in an optical microscope.

The graphene samples investigated in this work have all been prepared by the method described above. The reason this technique is preferred for many research purposes is because of the ease of preparation, the ability to prepare graphene flakes with large lateral size (even up to 1 mm) and that the graphene layers are nearly free of crystal defects. Nevertheless, micromechanical cleaving is not the only method available.

Another important graphene preparation technique, also published in 2004 [39], involves the formation of graphene layers on either the silicon or carbon face of SiC single crystals.

The SiC wafer is heated to temperatures in the 1200-1400°C range allowing the removal of surface silicon, leaving a carbon rich phase which forms graphene layers at these high temperatures. This process is ideally suited for future electronics purposes, because the graphene covers the entire surface of the SiC wafer and the substrate. However, the graphene prepared this way has more crystal defects than cleaved graphene [80].

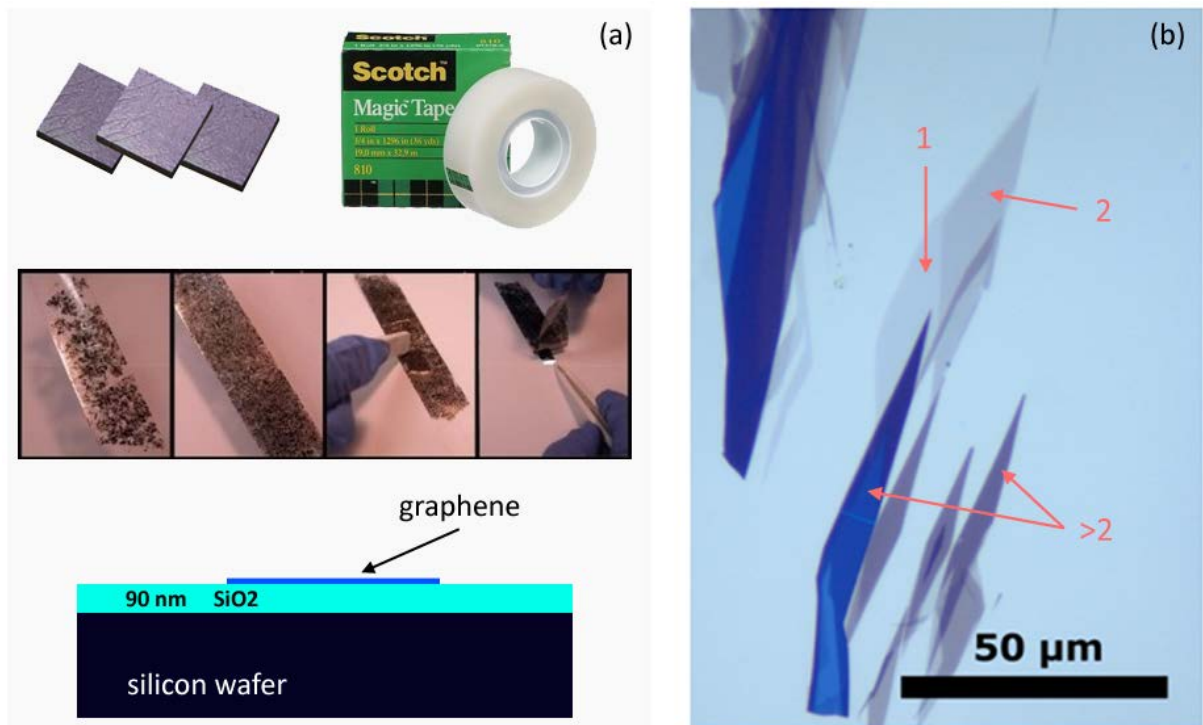


Figure 11. (a) Process of preparing graphene. In this “top-down” process, some highly crystalline graphite, like HOPG is repeatedly peeled using sticky tape. (b) Optical microscopy image of single layer graphene on 90 nm thick SiO₂. Single, bi- and multi layered graphite is highlighted by the red arrows.

Similarly to the case of CNTs, CVD methods have evolved to becoming one of the most important methods of graphene preparation, enabling the growth of graphene samples of macroscopic size [81]. Especially important is the growth of graphene layers on copper, pioneered by the group of Rodney S. Ruoff [82]. During this process a flow of hydrocarbons (usually methane) at low partial pressure is passed above a transition metal poly- or single crystal, heated to ~1000°C. Depending on the CVD parameters (pressure, temperature, cooling rate) single or multilayer graphene is deposited on the metal surface, which can be etched away and the graphene transferred to arbitrary substrates [81, 82]. Using this growth process, the size of the graphene is limited only by the size of the metal substrate, but it is important to mention that the graphene prepared this way is not a single crystal. During

growth multiple nucleation sites form on the metal surface, making the graphene a patchwork of grains a few 100 nm to a few microns in size [83]. Controlling this microstructure of CVD grown graphene remains a challenge.

1.4. Tailoring the electronic properties of carbon nanotubes and graphene

Since 2004 and the milestone papers describing some of the exciting properties of graphene [5, 36, 38, 39], the research into its basic properties has expanded in an almost exponential manner (Figure 2) [84]. The industrial use of graphene seems to be following suit, with some niche applications almost ready for market, most notably the use of graphene in displays, due to the fact that graphene has begun to match and in some sense to outperform indium-tin-oxide as a transparent electrode material [81]. But one of the biggest potentials for applications lies in exploiting the superior electronic properties of graphene in electronics. For example: it has high carrier mobility, for a wide interval of the value of the chemical potential [7, 8]; large charge carrier saturation speed [85]; high thermal conductivity [86] and in transistors: the smallest possible (one atom thick) channel thickness [87]; flexibility [81], etc. These properties make graphene based field effect transistors (FET) a candidate for future electronics applications. From among these properties, large charge carrier mobility is required for high speed devices, while high thermal conductivity $30\text{-}50\text{ W cm}^{-1}\text{ K}^{-1}$ (about 10x the value for copper) aides heat dissipation in devices [87]. In recent years, very promising radio frequency transistors have been prepared, which use graphene as a channel material. These devices have a cut-off frequency (the frequency at which the transistor is still usable in RF applications) of 100 GHz [88], exceeding the performance of Si based, and approaching that of GaAs based high electron mobility transistors of similar gate lengths [87].

On the other hand, despite the proposals made for graphene based logic FET devices [89], this kind of application still eludes us, due to the high on/off current ratios ($10^4\text{-}10^7$) required for such applications. The crux of the problems is the lack of a band gap in graphene. However this “deficiency” can be addressed by various means of “band gap tailoring” [8].

In the case of CNTs the lack of a band gap is seemingly not a problem, as one of the interesting properties of nanotubes is that their electronic structure can be tuned by changing the chirality of the nanotubes. The band gap can vary from a metallic state to large

gap values in the 1 eV range. However, “tuning” is a misnomer. To be able to tune the properties, one would need to be able to synthesize CNTs with a specific chirality, or be able to separate a single chirality from among many in a sample. Research effort in this direction has begun to bear fruit [24, 25] but there are other, depending on application, more convenient routes to tailor the properties of CNTs through the attachment of chemical groups to the nanotube sidewall.

1.4.1. Carbon nanotube functionalization

The chemical modification of the nanotube sidewalls enables the tuning of the interaction of the tubes with their environment and tailoring of the nanotube properties [90, 91], while allowing researchers to employ the vast possibilities offered by chemical methods in tackling these problems. The attachment of chemical groups to the nanotube sidewalls (functionalization) can be used to alter the nanotube electronic properties [90, 92, 93, 94, 95, 96] and may be used to tune the interaction of the nanotubes with their surrounding [3, 97] and each other, for example to achieve their self assembly into device architectures [98].

Various forms of functionalization exist, depending on the nature of the chemical bond between nanotube and chemical group [90], for example physisorption of molecules can have influence on the CNT properties [99]. However, in the present work I explore the properties of CNTs, which have functional groups attached to their sidewalls by covalent bonds. As such, I introduce these systems in more detail.

The addition of functional groups to the nanotubes usually takes place at defect sites in the CNTs or at the end caps. This is due to the lower activation energy for chemical reactions at defect sites (vacancy, non hexagonal arrangement of C atoms, etc.). The defect concentration on CNTs is in the order of 1-3% of the carbon atoms [100], so the functional group concentration will have a similar value. Only very harsh conditions, such as fluorination, allow the addition of chemical species directly to the sidewalls [101]. Thus, usually before the functionalization reactions are implemented, further defect sites are generated by oxidation [102]. After defect creation the nanotube sidewall can be functionalized by a variety of chemical groups [91], a very common option being carboxylic groups, which can be introduced by exposing the CNTs to nitric acid (Figure 12) [91, 100].

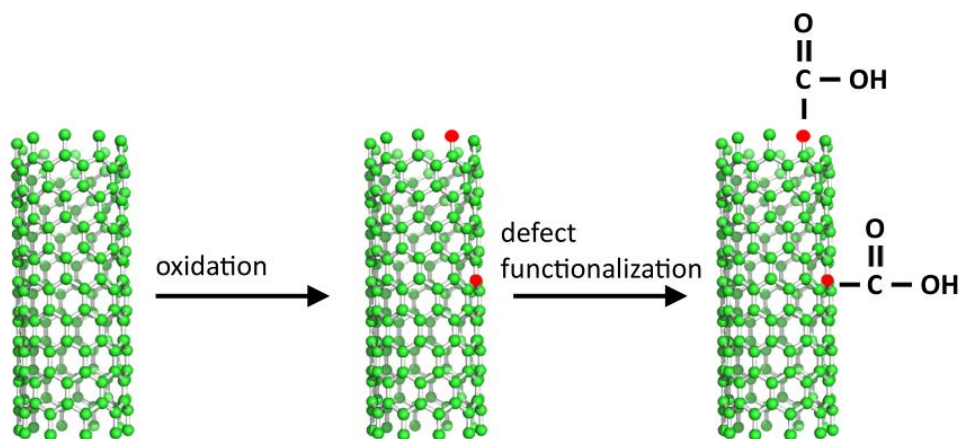


Figure 12. A flow-chart of CNT functionalization. A usual route is the introduction of defects into the nanotube sidewall and ends (red circles). This is followed by the addition of chemical species to the as obtained defect sites, in this case carboxyl groups, using nitric acid treatment.

After the addition of the functional groups (in our case carboxylic groups), a wide range of chemical modifications can be performed on them, allowing the coupling of other molecules by covalent bonds [76, 90, 91, 102, 103, 104].

The changes induced by functionalization in the nanotube electronic structure is a strong function of functional group concentration and type. At very high functionalization degrees and random distribution of functional groups, the translational symmetry of the nanotube will be broken and we can no longer talk about the CNT band structure, as such. If a high concentration of functional groups are arranged in an ordered and periodic fashion on the nanotube sidewall the band structure changes dramatically [105]. However, this kind of ordering has not yet been achieved experimentally and the distribution of functional groups in samples studied to date can be considered random [90]. At low functional group concentrations discussed in this work (a few % of the C atoms) the influence of the functional groups can be considered as a perturbation of the nanotube band structure. This perturbation manifests itself in many forms. The addition of functional groups can change in the Fermi level of the nanotube, often referred to as doping, for example in the case of the addition of dichlorocarbene [94] or the physisorption of nitric acid on the tube sidewall [99]. During functionalization, as in the specific case of carboxyl group addition, the sp^2 carbon in the tube sidewall transforms into a sp^3 type atom. This change in the hybridization has significant influence on the charge transport properties of the CNT [95]. These effects are a kind of global influence, effecting the whole of the nanotube sample. More localized types of

perturbation are changes induced by specific chemical groups in the local electronic structure of the nanotube. The addition of functional groups creates additional states in the CNT band structure. Such changes are specific to the kind of functional group producing them, and are localized around the chemical group [92] (Figure 13).

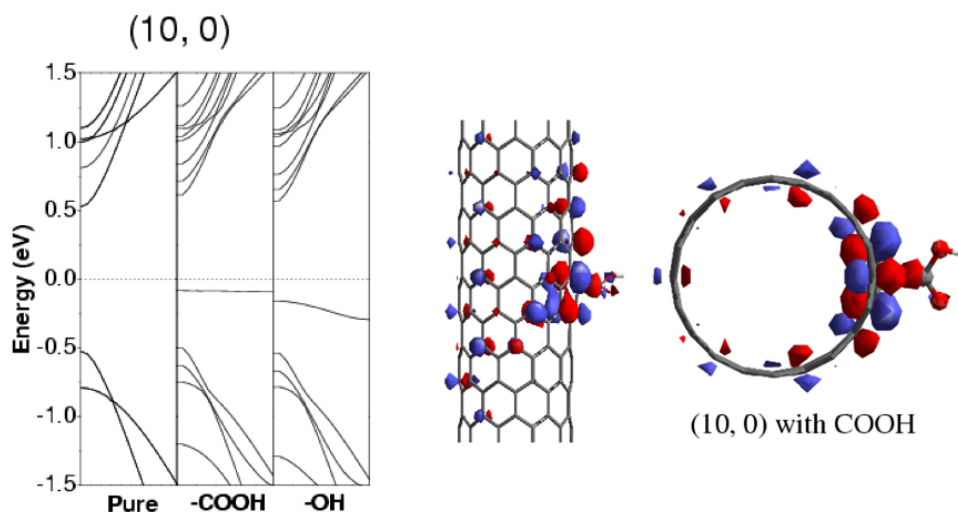


Figure 13. (Left) States induced in a (10,0) nanotube by carboxyl and hydroxyl groups, calculated from first principles. (Right) Iso plot of the impurity wave function induced by a carboxyl group. Reproduced from ref. 92.

Other changes in the CNT band structure as a result of functionalization are the observation of band gap opening in the case of metallic nanotubes and a suppression of the optical transitions between the nearest van Hove singularities [94]. Of course the ultimate goal of CNT functionalization is the exploitation of the nanotubes with tailor made properties in various applications. In Table 1 a list of such possible applications is given.

Characterization of the functional groups and the changes in the CNT electronic structure are predominantly investigated by optical spectroscopic methods [90]. Part of my work has been focused on enabling the visualization and characterization of functional sites on CNTs by scanning probe methods, specifically scanning tunneling microscopy (STM), which yield significant new information and complement existing spectroscopic techniques. In the chapters to come I will describe advantages of STM and new insights gained.

Table 1. Potential applications of functionalized CNTs, adapted from ref. 91.

(Potential) Application	Function of the covalently bonded chemical group
Nanostructured electronic devices	Local modification of the electronic band structure
Mechanically reinforced composites	Chemical coupling with a matrix
(Bio-) chemical sensors	Selective recognition of analyte molecules
Catalyst supports	Anchoring of molecules or metal nanoparticles
Chemically sensitive tips for scanning probe microscopy	Selective chemical interaction with surfaces
Field emission	Reduction of the work function for electrons at the tube ends
Artificial muscles	Mechanical stabilization of nanotube films through covalent cross-linking
Controlled drug release	Biocompatibility; recognition of biological fingerprints
Directed cell growth on surfaces	Specific interactions with cell surfaces
Pharmacology	Enzyme inhibition or blocking of ionic channels in the cell

1.4.2. Graphene nanoribbons and other graphene nanostructures

One of the most interesting features of graphene is the rich physics encountered when various nanostructures of graphene are considered. One type of nanostructuring was considered even before the discovery of exfoliated graphene. In 1996 Nakada et al. have theoretically explored the properties of graphene strips of a few nanometers width [106] (Figure 14). This lateral confinement has a similar effect on the electrons as the periodic

boundary condition in the case of CNTs. In a first approximation, the bands of such a graphene nanoribbon (GNR) can be obtained by applying the same kind of zone folding on the graphene band structure as in the case of CNTs and using the tight binding approximation [55, 106, 107] (Figure 14).

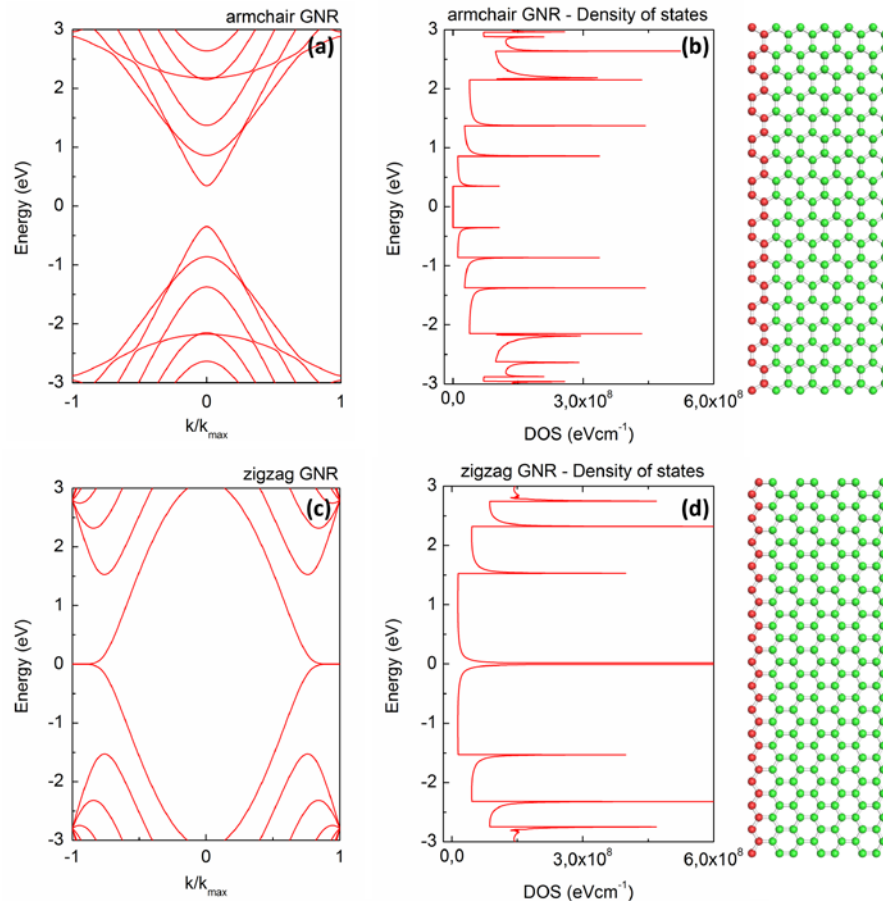


Figure 14. Band structure plotted along the wave vector parallel to the GNR axis (a, c) and density of states (b, d) for a armchair (top) and zigzag (bottom) type GNR. Structural models of the ribbons can be seen on the right. The bands are calculated using the tight binding approximation [55], neglecting the edge states of the ribbons. This particular armchair GNR has a band gap of almost 0.7 eV. A peculiar feature of the zigzag GNR bands is the flat bands at the Fermi level, which result in a sharp peak in the DOS.

We can analyze the case of GNRs with one of the two most stable edge geometries, either zigzag or armchair type. Analogous to the case of CNTs the bands of GNRs depend very strongly on the crystallographic orientation of the GNRs, with zigzag edged GNRs being metallic in character and some armchair type GNRs having a band gap. The size of this band gap scales roughly as a power law with the width of the nanoribbon (roughly $1/\text{width}$). Zigzag edged GNRs have states all the way through the Fermi energy, making them metallic.

They also have a very flat band right at the Fermi energy, which results in a sharp peak in the density of states (Figure 14). This state is localized on the zigzag edge [106] and can be observed in scanning tunneling microscopy (STM) images of graphite edges [108]. The nanoribbons studied here are considered to have hydrogen terminated edge atoms.

Observing that atoms at the edges of the nanoribbons do not have three other neighbors as in an infinite graphene crystal, we realize that in the above description the periodic boundary condition imposed on the graphene has no real physical meaning. Thus, we need to take into account the perturbation introduced by the edges. Son et al. have calculated the bands of graphene nanoribbons using first principles [109], including these edge effects. These calculations also reproduce the particular edge state of zigzag nanoribbons, but as it turns out these ribbons also have a minute band gap (Figure 15b). The band gap arises if the spin degrees of freedom are taken into account, with a predicted ferromagnetic state at the zigzag edge and antiferromagnetic ordering between the opposing nanoribbon edges.

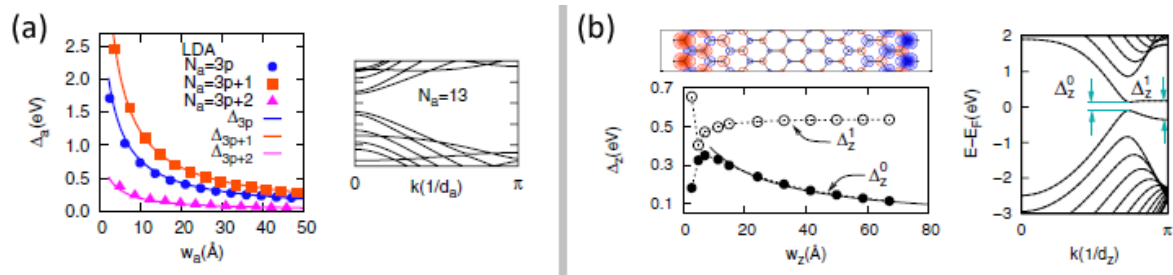


Figure 15. (a) Band gap of armchair type GNRs calculated from first principles. (b) Taking into account edge effects, even zigzag GNRs display a small band gap. Images adapted from ref. 109

Later theoretical investigation has shown that the magnetic states at the zigzag GNR edges can grant the nanoribbon a half metallic behavior if an electric field parallel to the GNR strip is applied [110]. Half metallic in the sense that the nanoribbon behaves like a metal for one spin state and as an insulator for the other. This prediction makes zigzag edged GNRs a possible candidate for use in spintronics devices, where usually d band metals are thought to be usable and not carbon, which has no intrinsic magnetism.

Beyond the spin properties of GNRs other, more exotic behavior is predicted for example in a kind of graphene nanoribbon structure seen in Figure 16a. Such a device would only admit charges from one K valley of graphene to pass through the narrow ribbon region. This would

enable the use of the valley degree of freedom in graphene for information processing, a kind of valley-tronics analogous to spintronics [111]. Going a step further, if we combine armchair and zigzag GNR structures into more complex systems, equally interesting properties can result, for example a quantum dot-like system in a zigzag nanoribbon device with armchair GNR leads (Figure 16b) [112].

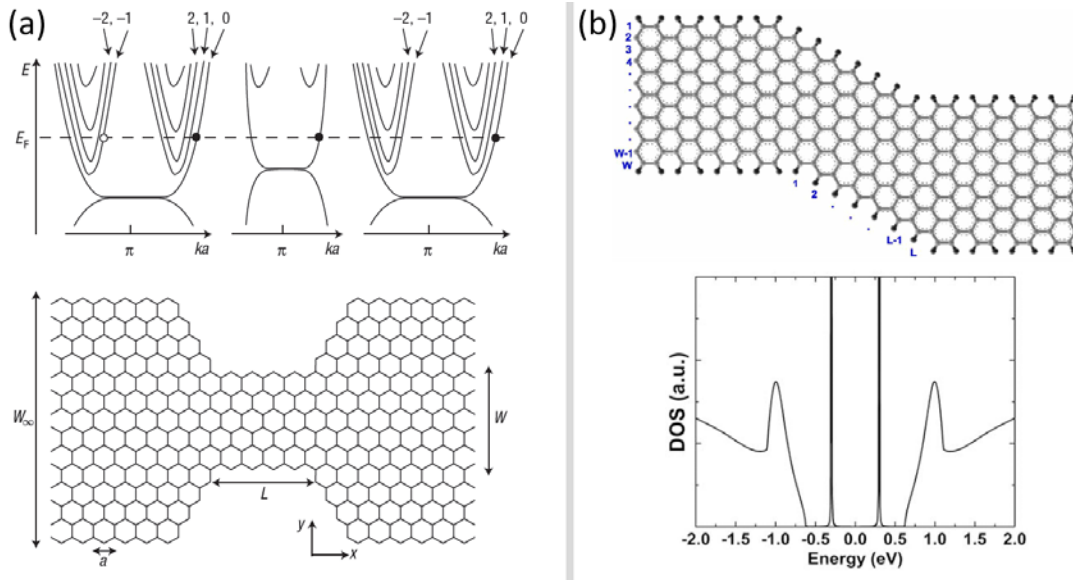


Figure 16. (a) A „valley-filter” realized in a graphene zigzag edged constriction, where the device only lets electrons from one K valley through (bands of the leads and constriction shown on the top). (b) A z shaped constriction consisting of a zigzag GNR section, with armchair GNR leads. The zigzag region shows quantum dot-like states. Image (a) reproduced from ref. 111 and (b) from ref. 112.

The predicted behavior of all the above examples, not to mention the properties of GNRs in general, rest on the assumption that the GNRs have atomically smooth edges, as shown in Figure 14. As is the case with all nanosized systems, graphene is very susceptible to the effects and interactions occurring at the surface atoms. In the case of graphene, all atoms are at the nanostructure surface or edges, thus the properties of GNRs, or of other graphene nanostructures will depend strongly on the kind of environment (supporting substrate, ambient, etc.) it is subjected to and the specific configuration of edge atoms. Real samples of GNRs and graphene will have a certain concentration of defects (vacancies, pentagon-heptagon pairs, disorder at the edges, etc.), which have a significant influence on the electronic structure and charge transport properties. It has been shown theoretically that the degree of edge functionalization [113, 114], not to mention the type of functionalizing radical [115] can have drastic effects on the charge transport mechanism [116,117] and

nanoribbon structure [118, 119]. This is one of the reasons, why the strong difference between zigzag and armchair nanoribbons, resulting from their different edge geometries, has not been detected in real systems yet [120, 121, 122]. Conventional routes of obtaining nanoribbons produce ribbons with highly disordered edges, the result of which is that the nanoribbon properties will not be dominated by the specific physics of armchair or zigzag edge terminations, but the degree of disorder [120, 122], although there have been some hints at edge specific behavior in zigzag edged graphene quantum dots [123] and the observation of possible quantum confinement effects [124].

It has been shown that in graphene nanoribbons obtained by traditional electron beam lithographic methods one finds a band gap, but this gap is not the result of the lateral confinement of the graphene [120]. It is a so called transport gap, being the result of various processes induced by disorder. Charge transport in this gap region is determined by thermally excited hopping between localized states [121]. The disorder responsible for this kind of behavior is either edge disorder in the GNR [121, 122] or charge inhomogeneity in the supporting SiO₂ substrate [125, 126]; it is most likely an interplay of both these effects (Figure 17).

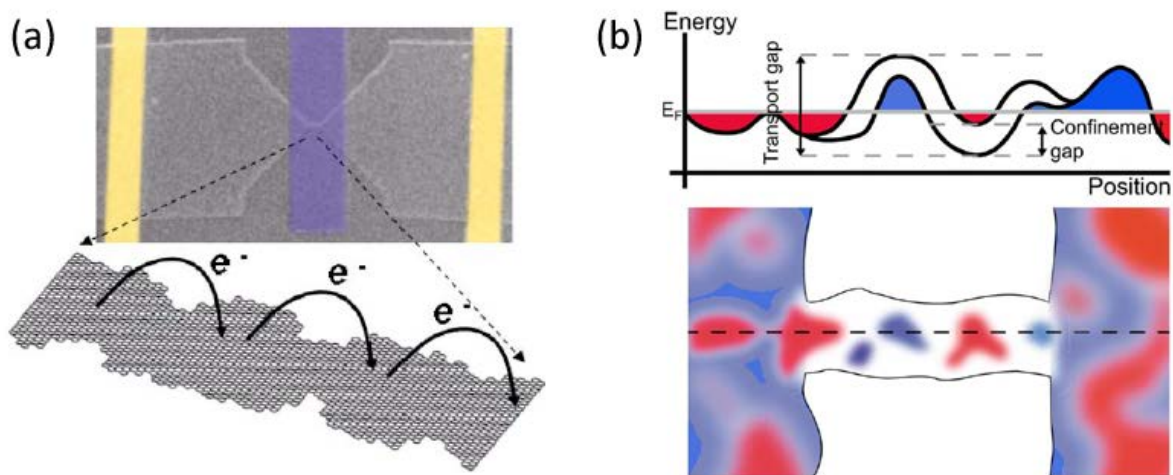


Figure 17. (a) A GNR produced by electron beam lithography. Due to edge disorder, the ribbon can be considered as a series of quantum dots, transport can be considered as a hopping of charge carriers between these. (b) Such quantum dot-like states can form as a result of charged impurities present in the SiO₂ substrate. Images reproduced from ref. 122 and 126.

Beyond charge transport experiments, optical means of differentiating between graphene's zigzag and armchair edges has proven to be a difficult endeavor. Inelastic light scattering has been proposed as a means to differentiate between the zigzag and armchair edges of graphene flakes, with a particular peak in the Raman spectra of graphene predicted to be localized on armchair edges [127]. According to theoretical considerations, this so called D peak, at 1350 cm^{-1} , should be absent on the zigzag edges. However, it has proven difficult to find such a marked difference in real graphene samples [127].

As mentioned before, the planar structure of graphene makes this material ideal for patterning it on the nanoscale. The breathtakingly fast evolution of research into graphene growth, mainly by the CVD method [81], has made possible the preparation of graphene samples of arbitrary size. Such sample production, combined with the right patterning tools could be used to tailor the graphene sheet into functional nanostructures, even whole electronic circuits [128]. However, based on the experimental results reviewed above, it is clear that observing the predicted edge specific physical phenomena in graphene nanostructures remains a challenge. The preparation of graphene nanostructures and the validation of theoretical predictions regarding specific effects arising from zigzag and armchair edges is one of the major goals of graphene research. In this thesis I describe a lithographic procedure, which allows the creation of zigzag edged graphene nanostructures and nanoribbons [T129*], opening up a new sample preparation route, bringing us one step closer the experimental validation of the predicted physical phenomena in zigzag type graphene nanostructures.

1.4.3. Preparation of GNRs

One method of graphene patterning has been used since the beginning of graphene research to pattern it into the "Hall-bar" geometries used to explore its peculiar magneto-transport properties [36, 38]. This technique relies on the creation of a polymer mask on top of graphene, by spin coating PMMA (polymethyl methacrylate) and exposing certain regions of the mask with an electron beam, making the polymer in the exposed regions selectively dissolve in a solvent. Such a mask can be used to etch certain regions of the graphene flake

* For the purpose of clarity the letter "T" is added in front of citations to articles used as a basis for writing the thesis points of the dissertation.

and to deposit metal contacts to the graphene structures defined this way. This is by far the most widely used technique to prepare nanoribbons [120] (Figure 18a). On its own, this technique cannot produce graphene nanostructures with crystallographically well defined edges, because the scanning electron microscope used to expose the polymer film does not have the desired lateral resolution. Furthermore, due to the oxygen plasma etching used, the edges of the graphene are highly disordered [122].

One technique which looked promising is the etching of CNTs along the tube axis in such a way as to obtain GNRs [130, 131] (Figure 18b). This may be a promising way to prepare GNRs in large quantities, but on closer inspection, it becomes clear that the technique inherits the problems plaguing CNTs. Namely that the diameter of CNTs cannot be controlled precisely. This is because the width of the GNRs is determined by the diameter of the nanotube we're "unzipping". Furthermore, the crystallographic orientation of the GNR edges is not known, or cannot be controlled [131]. There are only some hints that the GNR edge obtained using certain techniques [130] is predominantly of the zigzag type [132].

The etching of graphite and graphene layers by metallic nanoparticles is also a promising "nanomachining" process [133]. Metallic nanoparticles (Ni, Fe, Co) are deposited on graphene flakes and annealed at $\sim 500^{\circ}\text{C}$, usually in a flow of Ar and H_2 . During this treatment the metallic nanoparticles cut trenches into the graphene, with well defined crystallographic orientation (Figure 18c). There is evidence that at least in certain cases the trench edges have zigzag orientation [134].

One method which was able to successfully pattern GNRs with a well defined crystallographic orientation and width is STM lithography [135]. The STM tip is scanned over the surface, with a tip – sample bias voltage higher than that used for imaging and as a result very narrow trenches can be carved into the surface of graphite. Crystallographic orientation control is achieved because the STM is able to resolve the atomic structure of the surface. Very narrow nanoribbons (2.5 nm in Figure 18e) can be prepared due to the high precision with which the STM tip can be positioned over the surface. One drawback is that the GNRs cannot be prepared on an insulating surface.

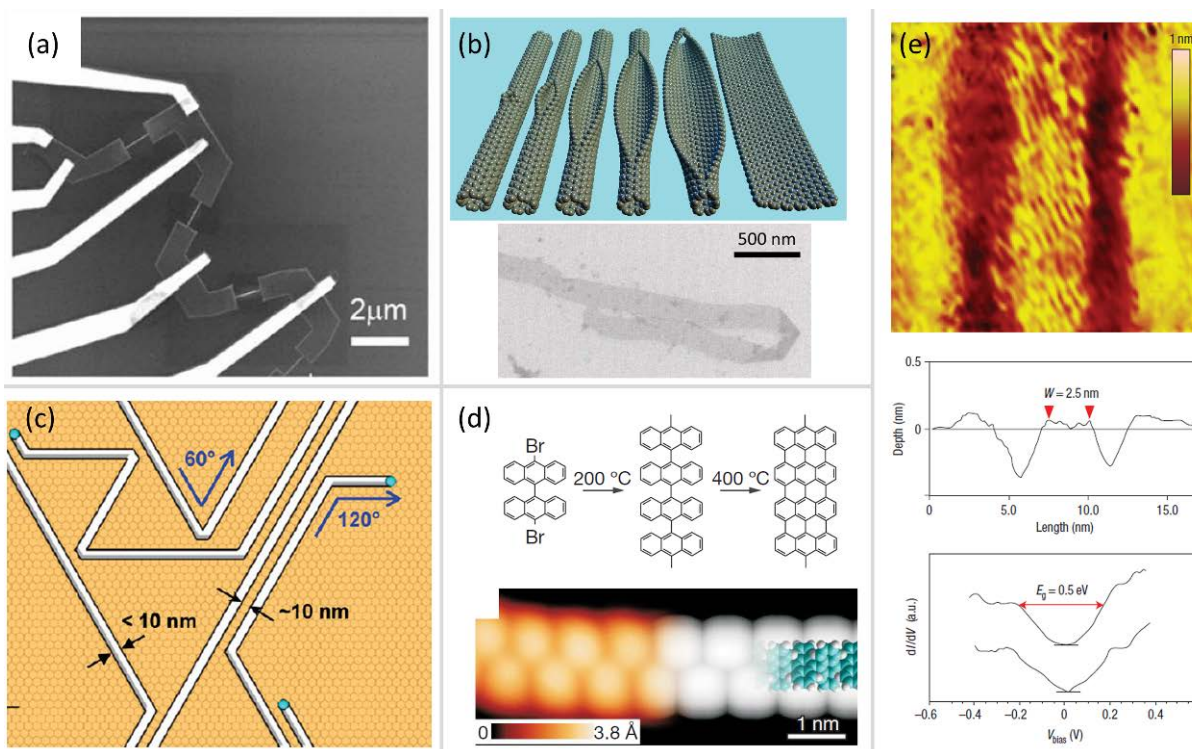


Figure 18. Methods of GNR preparation. (a) electron beam lithography; (b) „unzipping” of CNTs; (c) etching by metallic nanoparticles; (d) self assembly of aromatic molecules. (e) An armchair edged GNR patterned by STM lithography. Images adapted from ref.: 120, 130, 133, 135 and 136.

All the methods and processes of obtaining graphene nanostructures rely on some kind of nanostructuring of large area graphene layers. Alongside these top-down approaches, bottom-up processes, such as the self assembly of large aromatic molecules has been successfully applied to produce nanoribbons [136]. Chemically assembling GNRs from large organic molecules has the advantage of allowing the creation of very narrow nanoribbons (Figure 18d) , which have crystallographically well defined edges. However, the control over the width and length of the GNR and the controlled patterning or placement on a substrate has not been achieved yet. Furthermore, such self assembled graphene structures are usually grown on a metal substrate, which means that their electronic structure may be seriously perturbed by the vicinity of the metal. Table 2 compares the properties of the graphene patterning techniques discussed. These techniques are the ones most investigated and most relevant. However, over the years many different graphene patterning techniques have been developed, far too many for this work to give a completely accurate account of the field [137].

Table 2. A comparison of graphene lithographic techniques, regarding the preparation of GNRs. Each technique is classified following these criteria: 1. Whether it can produce nanostructures with well defined zigzag or armchair edges; 2. Are the nanostructure dimensions controllable; 3. Can it be performed on an insulating substrate, which would preserve the unique GNR electronic structure.

	Crystallographic selectivity	Size controllability	Insulating substrate
Electron beam lithography [120]	No	Yes	Yes
CNT “unzipping” [130]	No***	No	Yes
Etching by nanoparticles [133]	Yes	No	Yes
STM lithography [135]	Yes	Yes	No
Bottom-up / self assembly [136]	Yes	Yes*	No**

* possible (see text)

** usually grown on a metal surface.

*** this may depend on the kind of chemical process used in unzipping (see text)

2. Methods

Scanning probe microscopy, namely scanning tunneling microscopy (STM) and atomic force microscopy (AFM) have been vital to the results of this work. As such, a brief overview of these microscopy techniques needs to be given.

2.1. Scanning tunneling microscopy

STM has contributed greatly to approaching the ultimate goal of nanotechnology, i.e. to grant us the ability to manipulate and design matter at the atomic scale. It was the first tool with which surfaces could be investigated and manipulated at the atomic scale [138]. Furthermore, it allows the local measurement of the electronic structure of surfaces and molecules. STM is very different from traditional microscopy tools, in the sense that it doesn't use a photon or electron beam to image sample properties, but uses an atomically sharp tip to probe the sample. This probe, usually a metal wire with an atomically sharp tip is scanned in a raster in the vicinity of the surface and the interaction of the probe with the

sample is used to generate an image. In the case of STM the probe is usually an atomically sharp Pt or W wire. Because the tip and sample are separated only by a few angstroms, the probe-surface interaction used to map the sample is a small electrical current, due to quantum mechanical tunneling between the tip and a conductive surface. By applying a bias voltage of a few hundred millivolts between the tip and sample, the magnitude of the tunneling current is in the nA range and decays roughly exponentially with increasing the tip-sample distance, making the tunneling current highly susceptible to variations in the tip-sample distance. Using this property of the tunnel junction, we can map the sample surface very precisely, by scanning the tip across the sample and using a feedback to keep the tip sample current constant at all times. Such a (atomically) precise scanning in both the sample plane and the z direction can be achieved with piezoelectric actuators (Figure 19).

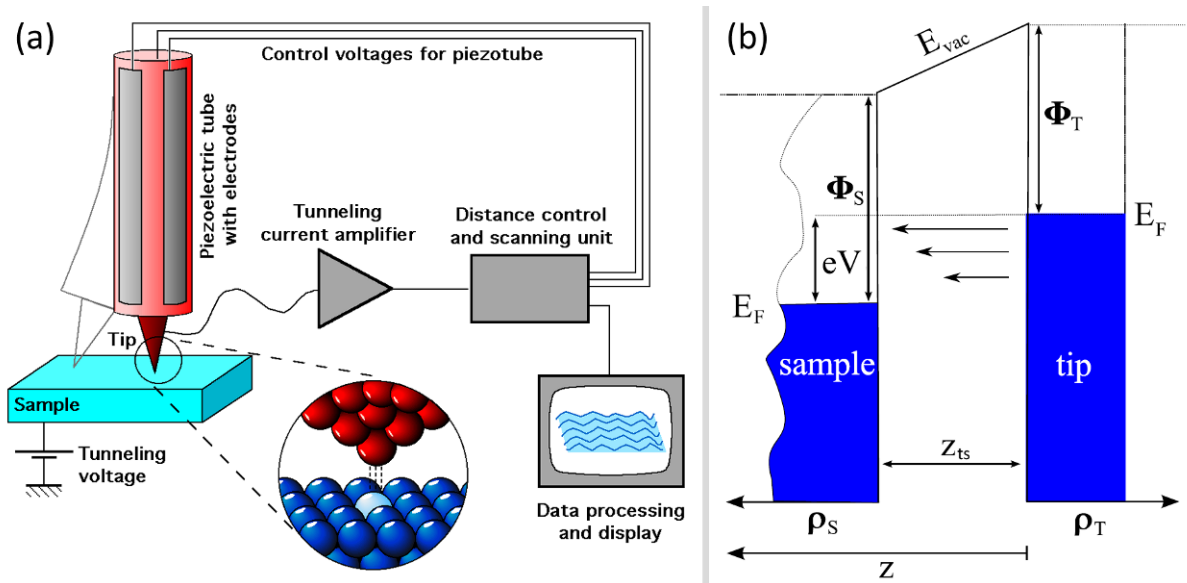


Figure 19. (a) Operating principle of STM. (b) The tunneling process. As a convention throughout this thesis, a positive bias displaces the tip states to higher energy.

To understand STM measurements, we must examine the physical processes that influence the tunneling current. The quantum mechanical tunneling process can be understood in an approximation, where we treat the tip and the sample as a metal, with all the electronic states filled up to the Fermi level. In a one dimensional model, where the two metals are separated by a vacuum gap of size z_{ts} , the voltage V between them separates the Fermi levels of the two metals by eV , so that the electrons tunneling from the tip into the sample must overcome the potential barrier formed by the work functions (Figure 19). The origin of

the exponential decay of the tunneling current is the decay of the localization probability of a tip electron in the sample, represented by state $\psi(z)$:

$$(VIII). \quad |\psi(z)|^2 = |\psi(0)|^2 e^{-2\kappa z}, \kappa = \sqrt{m_0(\Phi_s + \Phi_t - eV) / \hbar^2},$$

where Φ_s and Φ_t are the sample and tip work functions and m_0 is the free electron mass. To express the tunneling current, we have to introduce the concept of a local density of states (LDOS). This quantity measures the number of electronic states in an energy interval at a specific position in the sample:

$$(IX). \quad \rho(\vec{r}, E) = \sum_n |\psi_n(\vec{r})|^2 \delta(E_n - E)$$

Taking into account tunneling from tip to sample and from sample to tip, the current can be written as [139]:

$$(X). \quad I = 4\pi e \hbar^{-1} \int_{-\infty}^{\infty} \rho_t(E - eV) \rho_s(E) (f_t(E - eV) - f_t(E)) |M|^2 dE,$$

where $f(E) = (1 + \exp(E / k_B T))^{-1}$ is the Fermi-Dirac distribution function for the electrons. At bias voltages $V > 0$ electrons flowing from the tip into the sample are responsible for the current, while at $V < 0$ the direction of the current is reversed. Furthermore, the current is a function of the tip and sample LDOS. The above expression also depends on the tunneling matrix element M , which describes the overlap of the tip and sample wavefunctions. Beyond the simple one dimensional model, this term is hard to calculate because it is dependent on the specific tip and sample geometry (positions of the atoms) and the wavefunction of the system at the energies involved. However, using an approximation of the tunneling matrix element developed by Tersoff and Hamann [140], a picture emerges which makes the interpretation of STM images easier. They have described the STM tunneling process by treating the tip as a single atom, and use a wave function with a spherical symmetry and a constant DOS for the tip in the energy interval of interest. Furthermore, this description does not take into account inelastic tunneling, where an electron can gain or lose energy during tunneling by scattering with phonons [141]. Using

this approximation, the matrix element depends only on the sample wave functions and the tunneling current can be written as:

$$(XI). \quad I = C \rho_t \int_0^{eV} \rho_s(E) dE,$$

where C is a constant. The above expression assumes small tip – sample bias voltage and a temperature of zero Kelvin. The tip DOS being constant, drops out of the integral and the current depends only on the sample LDOS. Thus, an STM image can be considered a map of the LDOS. In spite of all the approximations, the Tersoff – Hamann approach can be used to quantitatively describe STM images [140]. In most cases the STM tip can be considered a single atom due to the exponential decay of the current with tip sample distance, meaning that the largest contribution to the tunneling current will be coming from the apex atom in the tip. Furthermore, the width of the tunneling channel is comparable to atomic distances and this channel is essentially the probe with which the sample is measured. Combine this property with picometer precision positioning of the tip above the sample and atomic resolution can be achieved.

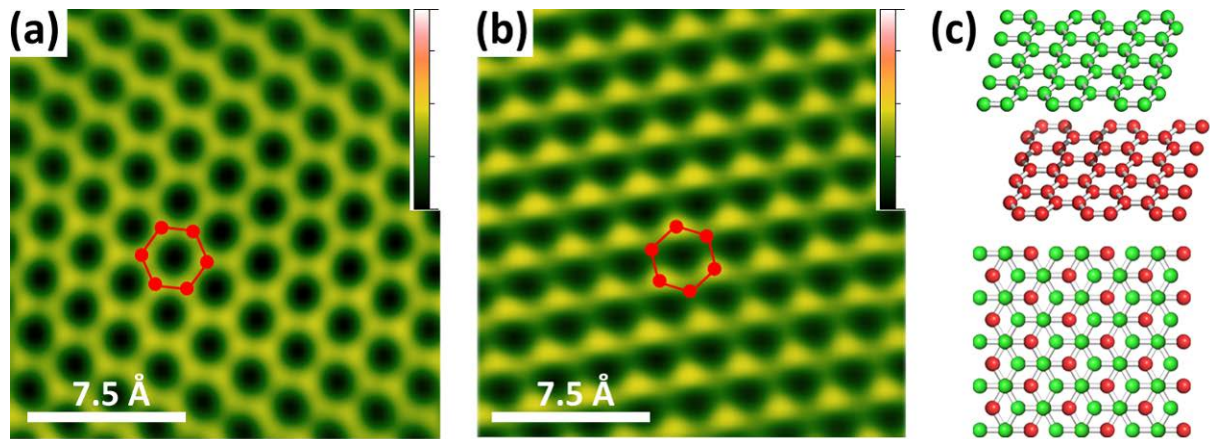


Figure 20. Atomic resolution STM images recorded under ambient conditions at room temperature. (a) Atomic resolution STM image of a single layer of graphene on SiO_2 , each atom appears with equal intensity. (b) STM image of graphite (HOPG). The corrugation of atoms on one sublattice is larger than on the other sublattice, owing to the difference in the LDOS. Positions of the carbon atoms are shown by red hexagons (Color bars span 190 pm). (c) The crystal structure of graphite, showing ABAB stacking.

The fact that the sample LDOS modulates the STM images is apparent if we compare the STM images I have recorded with the same instrument on graphene and graphite (HOPG)

(Figure 20). In the case of imaging graphene layers on an insulator (SiO_2) the honeycomb atomic lattice is clearly resolved (Figure 20a). However if we measure graphite, the atomic lattice changes considerably. The ABAB stacking of graphite is such that under one sublattice of carbon atoms (Figure 3) there is another carbon atom in the second graphene layer (Figure 20c). The overlap of the wavefunctions in these neighboring atoms slightly alters the LDOS under one sublattice, changing the apparent height in STM. Based on these two examples it becomes clear that the STM images are determined not only by the sample topography, but also the LDOS. This should be remembered when interpreting STM images.

Based on the approximation put forward by Tersoff and Hamann [140] the tunneling current is a function of the sample LDOS integrated over the energy interval, which spans the bias voltage (V) applied between the STM tip and the sample. In this picture the tunneling conductance, i.e. the derivative of the current – bias voltage (dI/dV), is directly proportional to the sample LDOS at the energy given by eV :

$$(XII). \quad \left. \frac{dI}{dV} \right|_V \sim \rho_s(eV).$$

This result assumes elastic tunneling and that the metallic LDOS of the tip and the tunneling matrix element are constant in the energy interval studied. Using this property of the STM, we can position the STM tip above a region of interest and can acquire information on the LDOS in that region by ramping the tip – sample bias voltage and recording the current. This measurement mode of STM is called scanning tunneling spectroscopy (STS). By taking the first order derivative of an $I(V)$ curve we obtain a plot of the LDOS in the selected region of the sample. An STS spectrum of graphene and its derivative can be seen in Figure 21a and b, while a plot of the graphene density of states around the Fermi level can be seen in Figure 21c. The minimum of the tunneling conductance is due to the vanishing electron states at the K points of graphene. This minimum coincides with the Fermi level in an undoped sample. The Fermi level can shift up or down in energy in the case of n or p doping respectively, shifting the position in bias voltage of the LDOS minimum. In addition to local LDOS measurements, the STS spectra can be recorded simultaneously with the STM topography. In this so called current imaging tunneling spectroscopy (CITS) measurement mode, the STM tip is scanned over the surface, mapping its topography, but in each pixel of

the CITS image the tip is stopped, feedback is switched off and an STS curve is recorded and stored together with the topography data. Using CITS data we can obtain local tunneling conductance maps of the sample by plotting the derivative of the current (dI/dV) as a function of the tip – sample bias voltage. This makes STM a powerful tool, which can give both spatial and energy resolution at the same time.

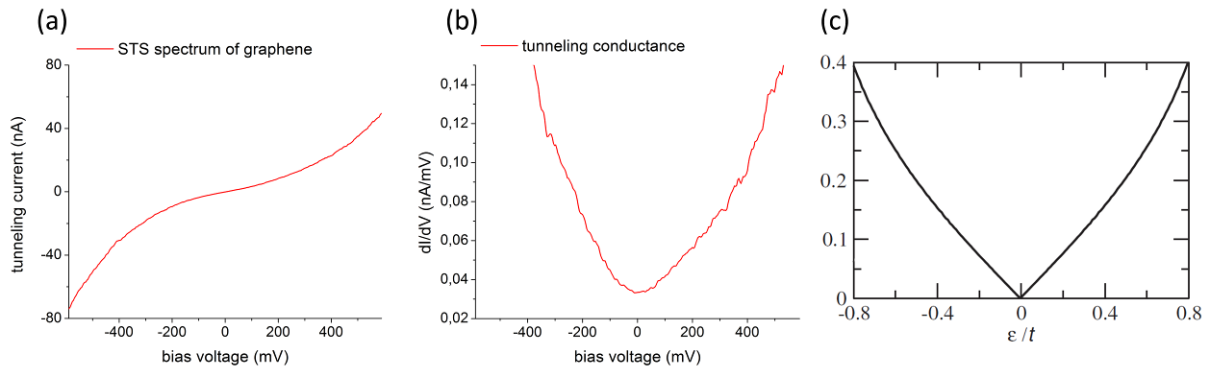


Figure 21. (a) A typical STS spectrum of graphene; (b) Plot of the tunneling conductance (dI/dV), which is proportional to the LDOS of the sample at the measurement location; (c) Plot of the DOS of graphene, calculated in the tight binding approximation. The energy scale is in units of the nearest neighbor hopping integral, the Fermi level is at 0 energy. Image (c) is reproduced from ref. 44.

2.2. Atomic force microscopy

After the invention of the STM it quickly became apparent that other physical processes could be used to map surfaces, not just a tunneling current [142]. The operation of AFM is similar to that of STM. The difference being that the physical interaction used for imaging is different. In so called contact mode AFM the scanning probe is a very sharp tip mounted on a cantilever, which is brought into contact with the sample and scanned using piezoelectric actuators. The feedback signal is the deflection of the cantilever, accurately measured using a laser spot reflected off the cantilever end (Figure 22). By keeping the tip sample force constant, which is equivalent to keeping the cantilever deflection at a constant value, the surface topography can be mapped by recording the voltages applied to the x, y, and z piezo actuators.

Developed after the invention of contact mode AFM, are the so called dynamic AFM methods [143]. These methods still use a cantilever – tip system, but the cantilever is driven to vibrate near one of its eigenfrequencies. Usually the lowest frequency eigenmode is

chosen and this vibrating tip is brought close to the sample. During an oscillation cycle, the tip experiences rapidly changing forces, which act between the tip and the sample. As a function of the magnitude of these forces the vibrational characteristics of the tip change: amplitude, frequency, magnitude of the interaction force, etc. These signals can be used as feedback parameters, which allow the mapping of the sample surface.

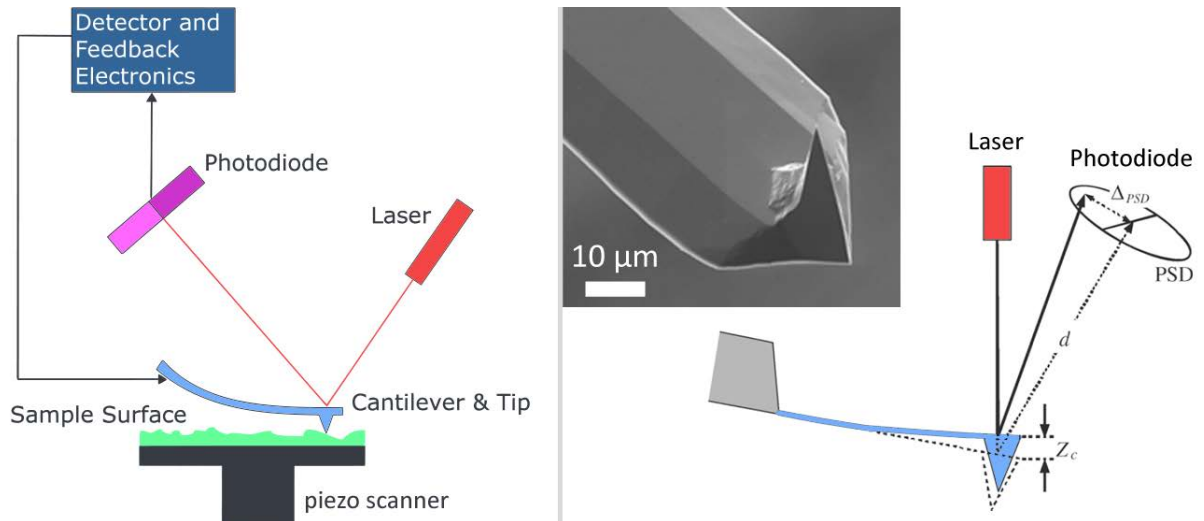


Figure 22. Operating principle of AFM. The deflection of the cantilever can be measured by a laser spot and split photodiode. The deflection (tip – sample force) is kept constant during scanning. Inset: scanning electron microscope image of a silicon TAFM tip at the end of a silicon cantilever.

One particular type of dynamic AFM technique is the so called intermittent contact, or tapping mode (TAFM) [143]. In using this method, the cantilever is vibrated at its base, with a frequency near resonance. This results in a ~5-30 nm amplitude of the tip which is reduced by tip – sample forces, if brought close to the surface. The tip amplitude can be measured by the same laser reflection method as in the case of contact AFM (Figure 22b). There are several advantages of TAFM over contact mode AFM, one of them being that the lateral forces acting on the cantilever are negligible. This results in less tip wear during imaging and allows for a much sharper tip to be used, which improves the lateral resolution of AFM images. Two of the most important parameters used for TAFM imaging are the free amplitude of the tip and the setpoint amplitude. The free amplitude is the amplitude of the tip without any interaction with the sample surface, while the setpoint is the amplitude at which the measurements are performed, usually it has a value of ~80% of the free amplitude.

As is the case with STM (Figure 20), AFM images are not a true representation of sample topography. The response of the tip amplitude is determined by the forces acting between the tip and sample and the complex dynamics of the vibrating tip – surface system. This is why a good understanding of the imaging mechanics is needed to be able to determine the true topography of a sample. I discuss this problem in detail in relation to the measurement of graphene flakes supported on a SiO₂ substrate.

3. Results and Discussion

Appropriate preparation and measurement techniques go hand in hand in the process of exploring the physical properties of carbon nanostructures, towards the ultimate goal of designing nanostructures with well defined features. The sub nanometer resolution of STM and AFM provides information that is vital to the understanding of the processes involved in the preparation of carbon nanosystems and their physical properties. Furthermore, to be able to extract any meaningful information from measurements, a good understanding of the physical interactions that occur during STM and AFM imaging is required. Herein I explore the following problems in the scanning probe imaging of carbon nanosystems: I describe a novel method that enables the mapping of the electronic structure of functionalized CNTs [T132]; provide a tip-surface interaction based explanation for the anomalous measurement results in AFM imaging of graphene [T144]; and finally, I give evidence of a graphene nanolithography process, which enables the preparation of graphene nanostructures with zigzag edges and the scanning probe exploration thereof [T129, 145].

3.1. Mapping of functionalized sites on carbon nanotubes

As discussed in earlier sections, the functionalization of CNTs modifies the nanotube surface topography and electronic structure. Changes to the nanotube electronic structure are usually investigated by optical spectroscopy, which is a global probe of CNT properties [94], meaning that we get averaged information about the sample as a whole and the nanoscale structure of the nanotubes remains unknown. On the other hand STM is uniquely suited to study both the topography and the electronic structure of CNTs with a sub nanometer

precision. As we shall see, this results in new insights into the nature of nanotube functionalization.

3.1.1. Challenges in STM measurement of functionalized CNTs

Given the advantages of STM, namely its ability to provide LDOS maps of the studied surface, it may seem strange that to date STM studies of functionalized CNTs are few and far between[†]. One reason for this may be that in the case of STM, as with any high resolution microscopy tool, good mechanical stability of the sample is of paramount importance to obtain reliable measurements. Functionalized CNTs have a problem in this regard, which obstructs their investigation by STM. Because of the presence of functional groups on the tube surface, the contact area with the substrate decreases and this leads to a weakening of the overall force (mostly van der Waals) which anchors the tubes to the support. During scanning, the metal tip of the STM can exert considerable force, mainly electrostatic in nature, on the tubes [146, 147] the result being that it can move the CNT in the fast scan direction and can effectively “clean out” the nanotubes from the scan area we want to investigate. This is illustrated in Figure 23b, where we show an AFM image of a 20x20 μm^2 area previously scanned by STM. TAFM does not perturb the CNTs on the surface, since the lateral forces exerted on the sample by the tapping AFM tip are much less than the ones during STM scanning. The STM scans the surface in a raster, moving the tip from right to left (and vice versa), this is the so called fast scan direction, and after completion of such a scan line, moving to the next line (slow scan direction). The AFM image was acquired by visually marking the area scanned by the STM, putting the sample into the AFM and placing the AFM tip, using an optical microscope, next to the marked region. From this AFM image it is clear that after only 3 passes over the same area by the STM, practically all of the CNTs have been brushed to the sides. The inset in Figure 23 shows how, during scanning of the STM tip, a nanotube can move to the side, returning to its original position after a few scan lines (fast scan direction is horizontal). Extensive movement of the CNT can be observed on the top image. Evidence of such tube movement is also present in the literature [76, 148, 149, 150]. While this problem seems to be less critical in the case of lightly functionalized tubes [151] and/or if the measurement is performed in ultra high vacuum [152, 153, 154, 155], it makes

[†] Based on the Web of Science database of publications at the time of writing.

imaging such CNTs a considerable challenge. One way around this problem is to immobilize the nanotubes, for example by binding the tubes to the substrate via strong chemical bonds. A good example for such an approach is the work of Zhang et al. [149], where they have used Au – S chemistry to anchor sulfur containing functional groups on the nanotubes to the Au substrate, effectively immobilizing them. However, this method is not applicable in all cases because of the need to have chemical binding between the nanotubes and substrate. Furthermore, the chemical bond may perturb the tube electronic structure [149]. Hence, a method is needed to immobilize CNTs on a graphitic support, which provides a sample that is stable enough to allow reproducible CITS measurements, is a well studied CNT – support system and does not perturb the functionalized nanotube structure. The solution to all of these problems can be given by incorporating the functionalized nanotubes sample into a few layer graphite (FLG) – nanotube composite.

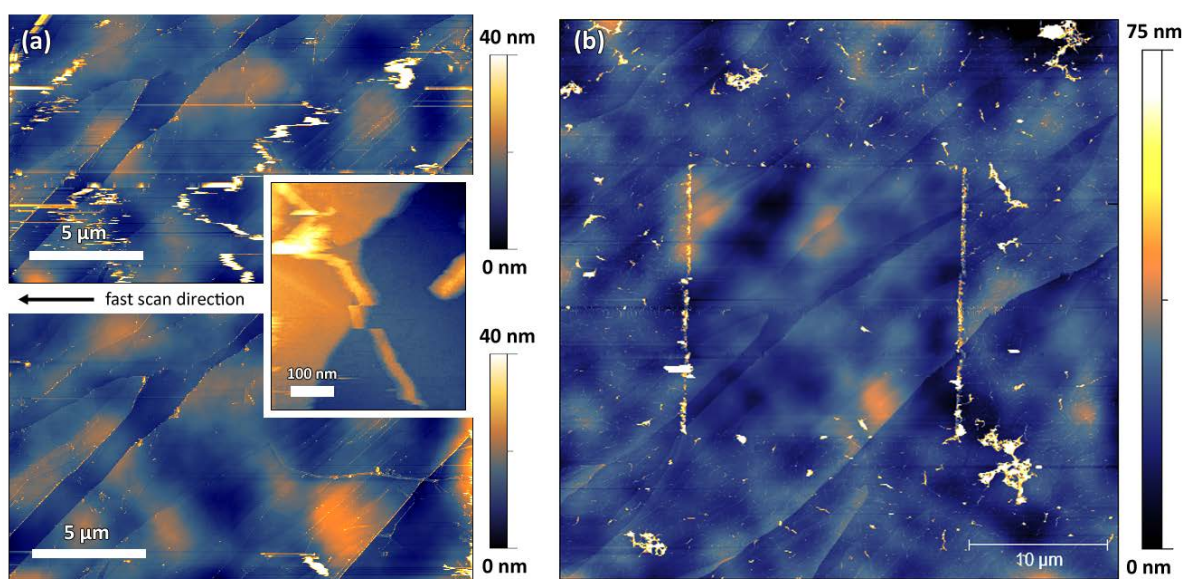


Figure 23. (a) Successive STM images (top and bottom) of a region on HOPG containing functionalized CNTs, show that nanotubes can be swept away by the STM tip. (b) Tapping mode AFM image on the HOPG surface, measured in a region where the STM tip was previously scanned (a). The AFM image is taken after the 3rd STM scan and it can be seen clearly that the CNTs have been swept to the sides and out of the STM scan area. STM scanning was performed using 300 pA current setpoint and 100 mV bias voltage.

3.1.2. Methods, sample preparation and initial characterization

The concept behind nanotube immobilization by a FLG – CNT composite is a very simple one (see Figure 24a). In a mixture of FLG and functionalized nanotubes, some of the tubes on the

composite surface will be clamped by the graphene or FLG layers in a kind of “sandwich” structure. The nanotube movement due to tip sample forces will be restricted near the region where the tube sticks out from beneath the sandwiching FLG layers. This clamping results in a degree of mechanical stability of the tube, which allows reproducible and repeated STM and CITS measurements. The measurement scheme is presented in Figure 24a, while an STM image of the such a sandwich structure can be seen in Figure 24b. One of the advantages of this sample preparation technique is that the van der Waals interaction between the nanotubes and FLG does not alter the nanotube electronic structure in a significant way, like a metal would. Furthermore, graphite and MWCNTs have nearly the same work function [156], which means that no significant charge transfer is expected between the two components.

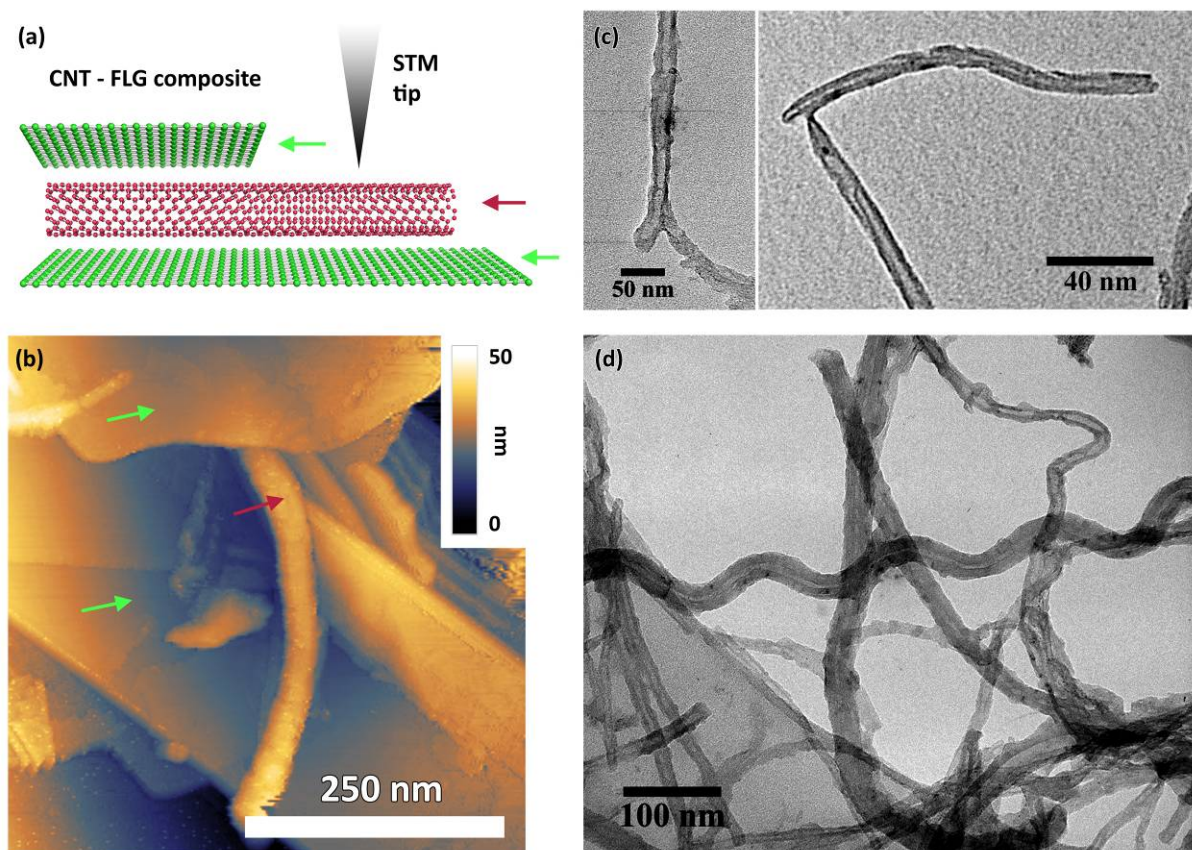


Figure 24. (a) Illustration of the CNT – FLG composite and the STM measurement. (b) STM image of a functionalized CNT sticking out from beneath a FLG layer. (c) and (d) TEM images of the functionalized CNTs. The surface of the tubes is irregular and some tubes are interconnected as seen in (c) [T132].

The growth and functionalization of the MWCNTs studied here was carried out by the group of Kiricsi and Kónya [102, 157]. A brief description of the nanotube growth, functionalization

conditions and spectroscopic evaluation of the sample will be given to provide the necessary context.

The study was conducted using MWCNTs, which have been prepared by chemical vapor deposition over alumina supported Co/Fe catalyst, using acetylene as a precursor [157]. The as obtained nanotubes were subjected to a purification treatment, which was carried out in two steps. First, the support and metal catalyst were dissolved in concentrated HF (38 wt%) resulting in nanotubes contaminated by amorphous carbon. In the second step, the amorphous carbon was eliminated by oxidation, using $\text{KMnO}_4/\text{H}_2\text{SO}_4$ aqueous solution [102, 158]. The nanotubes obtained this way are considered to be the “pristine” sample in our study, the functionalization of which was done in a three step process [102]. Briefly, in the first step the pristine CNT were treated in $\text{H}_2\text{SO}_4/\text{HNO}_3$ (3:1) mixture for 24 h at room temperature, then stirred overnight in SOCl_2 , followed by stirring in diaminopropane for 24h. This is a typical sequence of defect functionalization: the strong oxidation in the first step (due to $\text{HNO}_3/\text{H}_2\text{SO}_4$ and KMnO_4 during purification), eliminates some impurity carbon phases, induces defects on the nanotube walls [159] and attaches $-\text{OH}$ and $-\text{COOH}$ groups to these defects on the CNT outer wall and the tube ends, in addition it causes an overall p-doping of the nanotube π -electron system [99, 160] analogous to intercalated graphite nitrate [161]. In this case, the p doping means that electrons are removed from the nanotube, due to charge transfer between the tube and adsorbents, functional groups. The defect formation also affects the π -electrons: it converts carbon atoms from sp^2 into sp^3 hybridization state and in this way disrupts the conjugated electron system of the nanotube. The following two steps do not involve the tube wall and thus the π -electron system anymore; instead, the second step converts the $-\text{COOH}$ side groups into $-\text{COCl}$ and the third produces a peptide link on the two ends of the diaminopropane, thereby connecting two carboxylic groups. The two carboxylic groups can be either on the same nanotube or on adjacent ones, in the latter case forming covalently interconnected MWCNT as illustrated in Figure 25a.

The increase in defect concentration by the oxidation step can be detected by inelastic light scattering. Just like in the case of graphene and graphite, a double resonant scattering mechanism, made possible by the presence of defects, gives rise to a peak in the Raman spectra of CNTs at 1350 cm^{-1} wave number [162]. This so called “D peak” appears whenever

there is scattering of electrons between two non equivalent K valleys. This can happen near defect sites, such as an sp^3 type carbon formed due to the attachment of functional groups. The intensity ratio of the D peak to the G peak, at 1580 cm^{-1} , is considered to be a measure of the defect concentration in a sample [163]. A hallmark of all aromatic carbon systems, the G peak is an in plane bond stretching vibration mode in the honeycomb lattice [162]. The increase of the I_D/I_G ratio in the functionalized MWCNT sample can be seen in Figure 25b, indicating an increase in the defect concentration due to the oxidation treatment before functionalization.

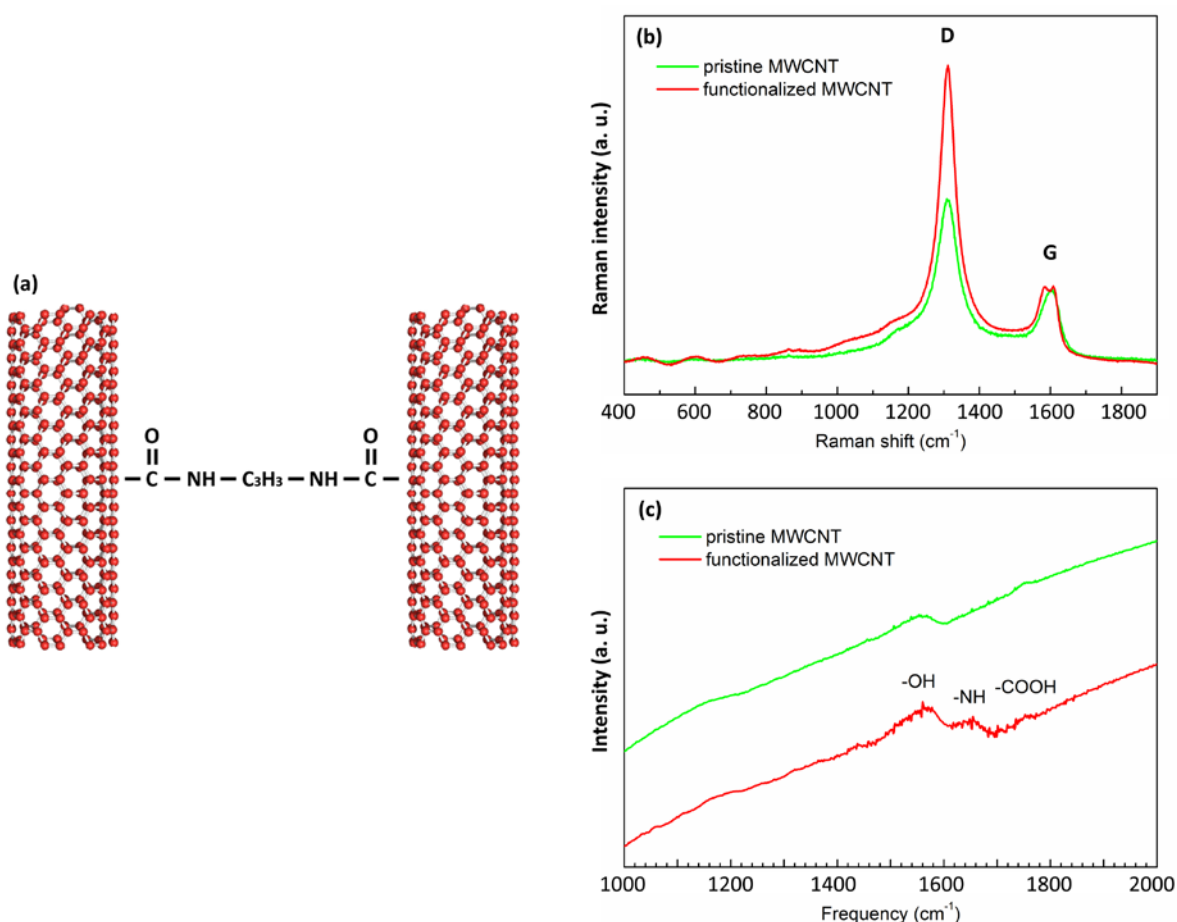


Figure 25. (a) Two MWCNTs interconnected by diaminopropane. (b) Raman spectra of the starting CNT material and of the functionalized sample. The spectra are normalized to the G peak intensity. (c) ATR-IR spectra shows peaks corresponding to $-\text{OH}$ and $-\text{COOH}$ groups (1720 cm^{-1}) in both the pristine and functionalized samples and a signature of $-\text{NH}$ (1630 cm^{-1}) in the functionalized sample [T132].

A complementary spectroscopic technique to Raman scattering is infrared spectroscopy. Attenuated total reflectance infrared (ATR-IR) spectra of the pristine and functionalized samples show signs of OH groups, which are most probably of extrinsic origin (solvent or

atmospheric water residues). The spectra of the functionalized samples contain the N-H bending vibration at $\sim 1630\text{ cm}^{-1}$, indicating the presence of the amine group in diaminopropane. The carboxyl vibration around 1720 cm^{-1} is present in the functionalized sample, indicating that the conversion to $-\text{COCl}$ groups in the second step was not complete. The carboxyl signal in the pristine sample is most probably due to the oxidation effect of the purification treatment of the nanotubes.

The CNT – FLG composite presented here is obtained by mixing the functionalized CNT with commercially available exfoliated graphite in isopropyl alcohol by ultrasonic stirring. The as obtained suspension was filtered through a polycarbonate membrane filter (200 nm pore size) and left to dry. Pieces from this so called buckypaper were cut out and placed on the STM sample holder, electrical contact to the buckypaper was made by carbon colloid paste. The STM measurements were performed under ambient conditions and room temperature. The STS data were extracted from the raw CITS data files and processed separately using Scilab (www.scilab.org) for easy extraction of individual STS curves. All the STM images and STS curves presented here were obtained using the same Pt/Ir STM probe. Tips were mechanically cut from Pt/Ir (80:20) wire and were used for characterization only if they produced reproducible STS spectra and atomic resolution on graphite. Atomic resolution images on the nanotubes were acquired using 500 pA tunneling current and 100 mV tip – sample bias voltage. STM topography and CITS images were acquired using 300 pA tunneling current and 300 mV bias voltage. TEM measurements were done using a Philips CM20 microscope operated at 200 keV.

The cross-linked carbon nanotubes, which are partially formed in the reactions described above, are an interesting avenue in improving the mechanical and electrical transport properties of nanotube networks [164, 165]. Furthermore, functionalization schemes similar to our own have been studied before [94, 166]. However, this is the first account of STM measurement on such nanotubes, probably because of the difficulties in the STM imaging detailed above.

3.1.3. Mapping of functionalized CNTs by CITS

STM and CITS measurements were performed on “sandwich-like” structures seen in Figure 24a. An STM image of a functionalized nanotube can be seen in Figure 26a, while in Figure

26b a map of the simultaneously acquired local tunneling conductance on this nanotube [T132]. This map was derived from the CITS data by taking the first derivative of the STS curves and displaying the conductance value at -160 mV bias voltage. We can observe in the same image the different conductance of the graphite support and of the nanotubes. Such dI/dV tunneling conductance maps are qualitatively proportional to the nanotube local density of states (LDOS).

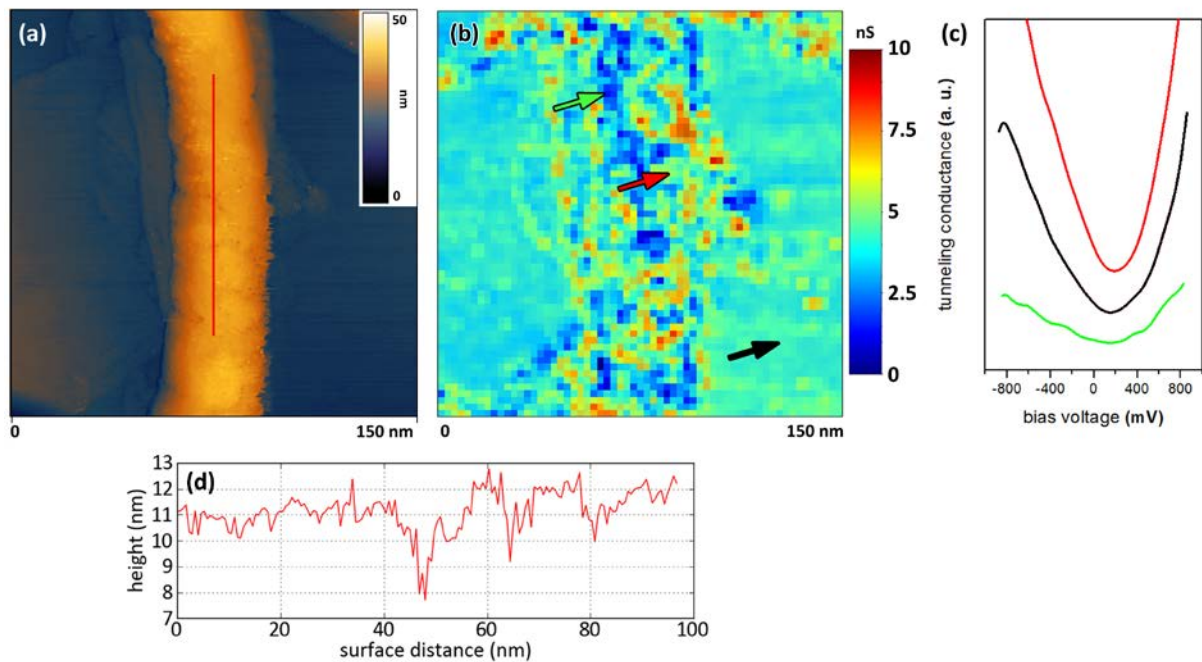


Figure 26. (a) STM image and (b) tunneling conductance map of a functionalized nanotube extending from below a FLG clamping layer (conductance units are in nano Siemens). In (c) we have the dI/dV spectra acquired at the regions marked by arrows of the same color in (b). The spectra are selected from three regions: the FLG substrate (black), regions of low (green) and high conductance (red) on the nanotube. The spectra are displaced vertically for ease of comparison. The tunneling conductance map is displayed at -160 mV bias voltage. A height profile along the red line in (a) is shown in (d). [T132]

At a first glance the dI/dV map on the nanotube surface shows regions of high and low conductance. Comparing the dI/dV curves from such selected regions we can see some similarities and some differences in the spectra. The curves from the high conductance regions (red arrow and curve) and the substrate (black arrow and curve) are similar and have a typical graphitic shape, with monotonically increasing conductance that is symmetrical with respect to the LDOS minimum (see Figure 21). Measuring a graphitic dI/dV signal on multiwalled CNT is a reasonable expectation, because at the large tube diameters in this

sample (~15 nm) the Van Hove singularities are very close together, due to the high density of allowed states along the tube circumference. They also get smoothed out, due to the spread of the Fermi function at 300K and due to disorder effects [167]. The minimum of the LDOS is shifted slightly to positive tip – sample bias voltages. This means that the chemical potential (Fermi level) is shifted away from its equilibrium position, i.e. that the sample is p-doped. It has been shown that nitric and sulfuric acid can have a strong p doping effect on CNTs [99, 160]. It can be seen in Figure 26 that the CNT is more intensely p doped than the substrate. In this particular case, acid molecules adsorbed on the nanotube surface are a result of the purification treatment. Furthermore, as the FLG flakes and the CNTs are mixed ultrasonically, some doping species may be transferred from the CNTs to the FLG. These molecules donate a positive charge to the carbon lattice, which becomes delocalized over the π electron system. This process leads to a “global” p doping of the nanotubes and has been measured previously by optical reflectivity and thermopower measurements [99, 160]. But the true power of CITS measurements comes from the local information it provides. Thus, examining the conductance maps further we can see regions with lower conductance (green arrow and curve) than the support or other regions on the tubes. dI/dV curves in these regions have a much less well defined minimum and are highly asymmetrical in places. We attributed these types of curves to defective and/or intensely functionalized regions of the CNT, where the low conductance values arise from defect functionalization which converts carbon atoms from sp^2 into sp^3 hybridization state and in this way disrupts the conjugated electron system of the nanotube [104, T132]. The STM topography of these tubes also shows a rough surface (Figure 26d), which is typical of highly defective and functionalized CNT, where the functional groups usually appear as protrusions on the nanotube surface [149, 151].

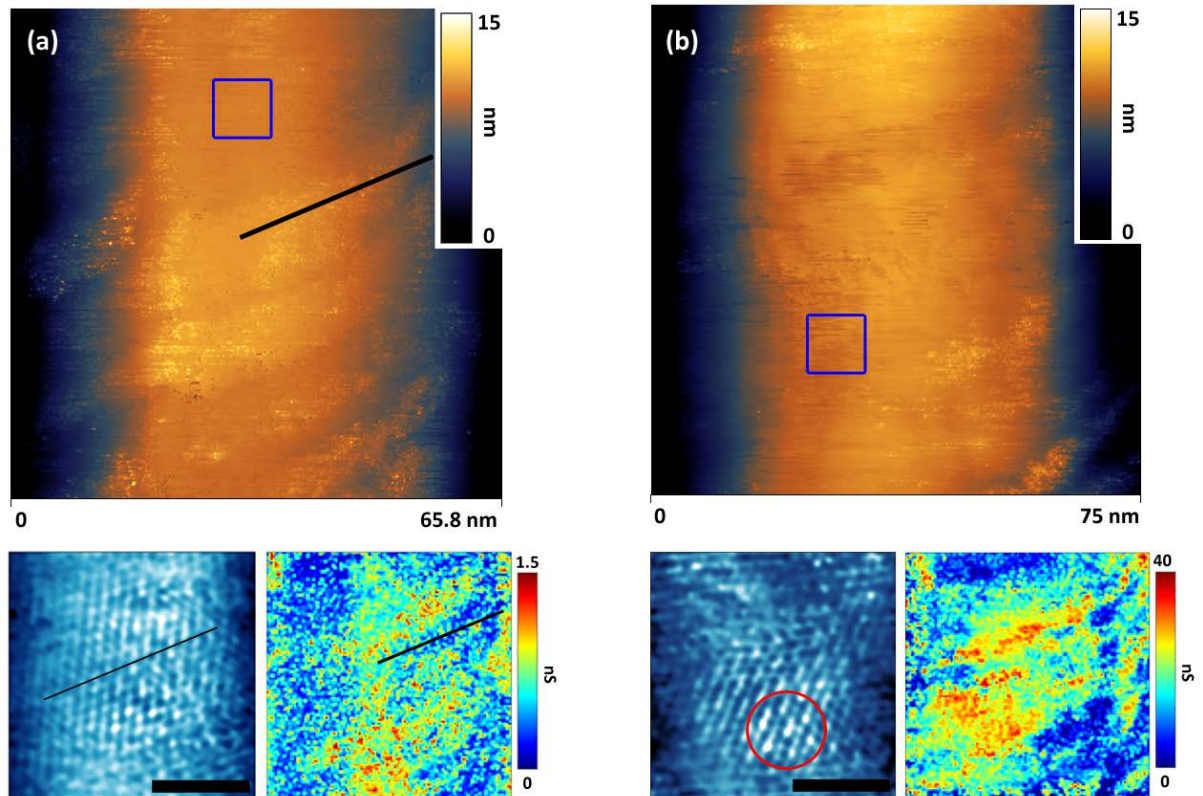


Figure 27. (a), (b) STM images of two different regions of the functionalized CNT shown in Figure 26. Panels at the bottom of the topography images show zoomed in, lattice resolved images obtained in the regions marked by blue squares and tunneling conductance maps obtained simultaneously with the topography, displayed at -225 mV bias voltage. Functionalized regions show up as protrusions on the nanotube surface and as low conductance areas in the conductance maps. Black lines mark the zigzag direction on the atomic resolution image and one of the “bands”, where functionalization is more pronounced. The functionalized regions follow the zigzag direction. The superstructure patterns on the atomic lattice are a sign of defect scattering (marked by circle). Scale bars on atomic resolution images are 2 nm [T132].

Figure 27a and b show two distinct STM topography images of a functionalized CNT. Comparing the conductance maps with the topography, we observe a degree of correlation between the low conductance regions and the protrusions on the surface [T132]. Especially in Figure 27a, bands of protrusions coincide with bands of low conductance in the corresponding dI/dV map. Furthermore, it was not possible to obtain atomic resolution images on the low conductance regions, only on the regions with high conductance. In addition to the graphitic dI/dV curves, this suggests that the regions with high conductance are mostly free of defects and functional groups. Here, alongside the atomic lattice we can observe a typical superstructure pattern, a hallmark of electron scattering between two non equivalent K points in the Brillouin zone (red circle in Figure 27) [151, 155, 168]. Because

these superstructure patterns can extend to a few nanometers from the defect site producing them [168] it is fair to say that they are due to scattering taking place on the defects created during oxidation and functionalization. If we compare the atomic resolution images with the functionalized bands, we find that these follow the zigzag direction along the nanotube circumference [T132]. To date, only a few such STM studies are available which show the correlation between crystallographic direction and functionalization, for example on fluorinated CNTs [155]. These measurements provide experimental evidence that oxidation of CNTs can prefer a specific crystallographic direction. This was presumed in recent experiments which involved the unzipping of carbon nanotubes to graphene nanoribbons [130, 169] and the chemical cutting of oxidized graphene sheets [170]. These results strengthen the evidence found in the literature that, when acidic oxidation is involved, etching takes place along the zigzag direction.

In Figure 28 the dI/dV maps of one nanotube are shown in more detail: I display six plots of the tunneling conductance map of the tube shown in Figure 27b, at different tip – sample bias voltages. These voltages have been selected to be symmetrical relative to the dI/dV minimum. We can distinguish three regions based on these maps. One region is where atomic resolution could be achieved (marked by a red arrow). Maps of such regions have symmetrical conductance values with respect to the minimum of dI/dV or in other words to the LDOS minimum. Such behavior is graphitic in nature, due to the symmetry in energy of the nanotube bands around the K points. As we have seen before, another region is where the overall conductance is low and no atomic resolution can be achieved. These changes can be attributed to heavily functionalized regions (marked with a green arrow). Further inspection of the maps reveals a third region, where the dI/dV maps are asymmetrical, here the tunneling conductance is higher for positive tip – sample bias voltages (blue arrow). The origin of this asymmetry is not clear, but it may be due to impurity states at functionalized or defect sites [92]. The regions with this asymmetry are clearly identifiable as higher conductance values in the dI/dV map plotted at 606 mV. Furthermore, these regions are highly localized on the surface, further strengthening the assumption that they are due to the presence of functional groups. Another feature of this dI/dV curve is that its minimum is shifted towards a more negative sample voltage, making this region more n-doped. We can expect such behavior if there is charge asymmetry between the nanotube and the

functional group, which leads to a local Coulomb potential and therefore to a shift in energy of the nanotube bands. In Figure 28 (right upper inset) I plot a map of the LDOS minimum on the nanotube by displaying the bias voltage value for the dI/dV minimum on a color scale. From this map we can see that the mostly functional group free regions are heavily p-doped, with a Fermi level shift of around 0.25 eV. This is the global doping level of the sample and as we discussed earlier it arises due to acid molecule adsorption. The map of LDOS minima correlates nicely with the conductance map showing the places of asymmetric dI/dV curves attributed to functionalized sites (blue arrows in Figure 28). It needs to be mentioned that the interpretation of this map is not straightforward in the low conductance regions, where the sp^2 carbon lattice is heavily damaged and the electronic structure of the surface is unknown, i.e. we do not have a model of the LDOS on which we can base our analysis. Thus, further work is needed to elucidate the significance of the features in these dI/dV curves (green curve).

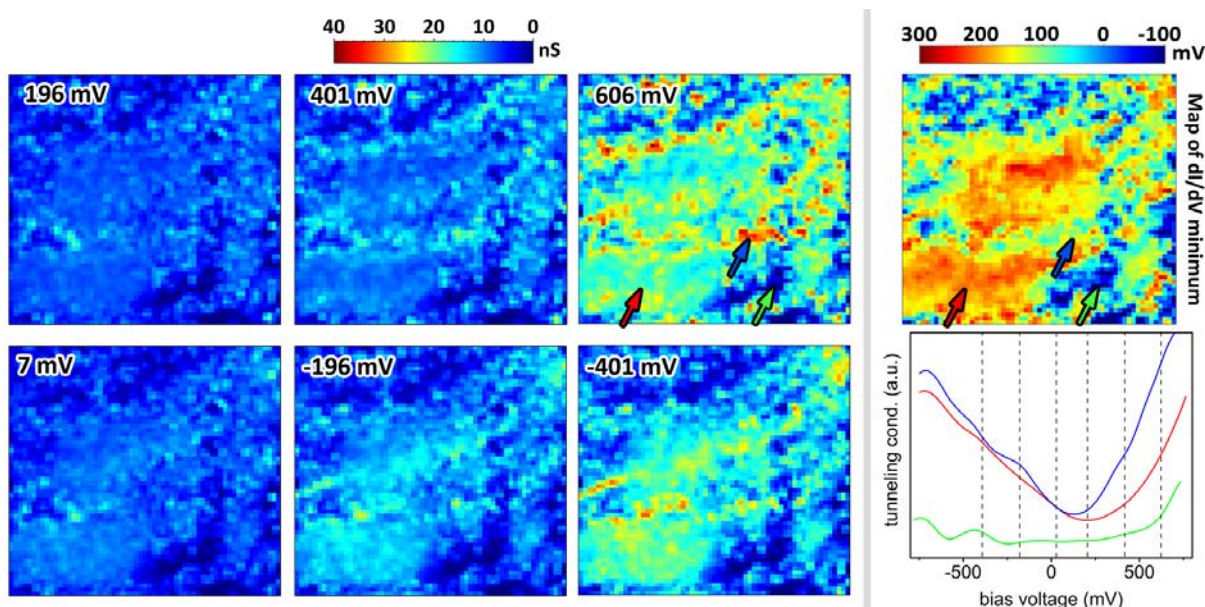


Figure 28. Tunneling conductance maps of the nanotube region seen in Figure 27b, with selected dI/dV curves. The bias voltages at which the maps were plotted are marked by dashed lines. Atomic resolution was achieved in the region marked by the red arrow. The low conductance regions show similar dI/dV curves as the ones seen in Figure 26 (green). (The dI/dV maps are 75x75 nm in size). Upper right: map of the dI/dV minimum of the same region as the conductance maps. The bias voltage value for the dI/dV minimum is displayed on a color scale. Colored arrows show the positions where the respective dI/dV curves were taken.

The CNT immobilization technique presented here is widely applicable to any type of functionalized nanotube. Using energy resolved STM measurements, I have shown for the

first time that oxidation and subsequent functionalization has a preference of advancing along the zigzag crystallographic direction on large diameter multiwalled CNTs. These measurements illustrate clearly the kind of advantage energy resolved maps can give, namely to spot sample features that are not apparent from STM topography maps and to provide information on local functionalization and doping [T132]. Furthermore, this measurement technique allows certain ‘in situ’ studies that could not be performed otherwise, for example to examine the topography and energy resolved behavior of functionalized CNTs, while being exposed to different gas or vapor environments. This may lead to a better understanding of the adsorption processes and the electronic structure variations involved in gas sensing with functionalized nanotube networks.

3.2. Measurement artefacts in AFM imaging of graphene

As we have seen in section 3.1, the scanning probe measurement of carbon nanostructures is a valuable tool in exploring these systems on the nanoscale. However, to have a full understanding of the measurement results we need a good grasp of the specific interaction and physical processes we use to map the sample. This holds true in the case of STM as well as with AFM.

Under ambient conditions the so called intermittent contact or tapping mode is most commonly used, during which the AFM tip (vibrated using a piezo actuator) is scanned over the sample surface, while the amplitude of the AFM tip is kept constant by a feedback loop and a 3D map of the sample surface is constructed by recording the feedback voltages applied to the piezo scanner regulating the tip – sample distance. While scanning, the sharp tip makes physical contact with the surface at every oscillation period and it experiences a range of repulsive and attractive forces. The variations in the tip sample forces are sudden and can range from “gentle tapping” to “hammering”[171] of the surface, which indicates that the tip behavior is a very nonlinear process [172]. In addition to the “normal” amplitude response of the cantilever due to changes in sample topography, the specific behavior of this nonlinear, coupled system of vibrating tip – surface can be rather unintuitive and can introduce deviations from the true sample topography in the final AFM image. This effect is especially important in the case of very small sample features which are comparable in size to such deviations, for example the thickness of a single atomic layer. These deviations can

occur for example due to changes in the material and/or mechanical properties of the surface on an inhomogeneous sample. Therefore, correctly measuring the size of nanoscale objects for example graphene, in tapping mode, is not as straight forward as one might first think [T144, 173]. Good control over the image acquisition parameters and understanding the imaging mechanism can go a long way to acquiring reliable data.

3.2.1. Anomalous graphene thickness measurements

Graphene layers are usually prepared on top of silicon wafers having a SiO₂ capping layer. The thickness of a single atomic layer of graphite is not easy to define, but on the SiO₂ substrate it is expected to be something very close to the Van der Waals distance of graphene layers in graphite, 0.335 nm. However, since the beginning of graphene research [5], various groups reported different thickness values for graphene layers measured by AFM, ranging from 0.35 nm to more than 1 nm, relative to the SiO₂ substrate. Novoselov et al. measured platelet thicknesses of 1-1.6 nm [5]. Gupta et al. have measured an instrumental offset induced by the AFM, of 0.33 nm, ie. 0.7 nm height for a single layer [174]. Other authors have also reported varying step heights for FLG supported on silicon oxide [175, 176, 177]. Furthermore, observations of distortions in the thickness of nanoparticles, measured with TAFM, are well known: anomalous nanoparticle height measurements, dependent on the free amplitude of the cantilever and material properties of the sample, were reported earlier [173, 178, 179].

AFM is used frequently to determine, or confirm the thickness of FLG layers measured by other techniques [180, 181]. Furthermore, a reliable way to measure the topography of graphene and other similar nanosized materials by TAFM would be welcome. The fact that the thickness of graphene films measured by different groups has a certain deviation suggests, that the data obtained are dependent on either the measurement parameters, sample preparations procedures or other laboratory conditions. The investigation into the dependence on scanning parameters of the measured thickness should be one of the first avenues of investigation.

3.2.2. Experimental methods

Graphene samples have been prepared by mechanical exfoliation. Graphene was deposited from HOPG (SPI-1 grade, purchased from SPI Supplies) onto a silicon wafer covered by a 300 nm thick layer of SiO₂. Graphene and few layer graphite crystals were identified using optical microscopy and measured by TAFM.

A Multimode Nanoscope SPM, from Veeco with a IIIa controller, was used in tapping mode to characterize the FLG samples, under ambient conditions. Silicon scanning tips used in tapping mode were purchased from Nanosensors (model: PPP-NCHR), with tip radiuses smaller than 10 nm (force constant ~42 N/m, resonance frequency in the range of 300 kHz). The cantilever drive frequency was chosen in such a way as to be 5% smaller than the resonance frequency. The free amplitudes of the AFM tips used were determined from amplitude – distance curves. Raman spectra were recorded on selected graphene films, using a Renishaw 1000 MB Raman microscope. The excitation source was the 488 nm line of an Ar⁺ laser with incident power in the mW range in order to avoid excessive heating of the sample, using a laser spot with a diameter of 2 μm.

3.2.3. Experimental investigation of the source of the artefacts

As detailed before, TAFM images are not a pure representation of topography, but depend on the material properties of the sample through the specific interaction forces between the tip and the surface. TAFM measurements of morphology, namely sample height, at constant amplitude show a surface of constant damping of the cantilever oscillation. This is why, the TAFM topography may be influenced by the specific vibrational characteristics of the AFM tip – sample surface coupled system. The amplitude of the cantilever is the main signal based on which the topography is mapped and it has been shown before that the value of the free amplitude and the setpoint amplitude have a strong influence on the imaging process [172, 173, 178], these measurement parameters were systematically varied in an attempt to experimentally reproduce the thickness values measured in the literature for graphene and FLG flakes. I have recorded the thickness values of a set of FLG flakes, using a range of values for the free amplitude and keeping the setpoint constant (Figure 29).

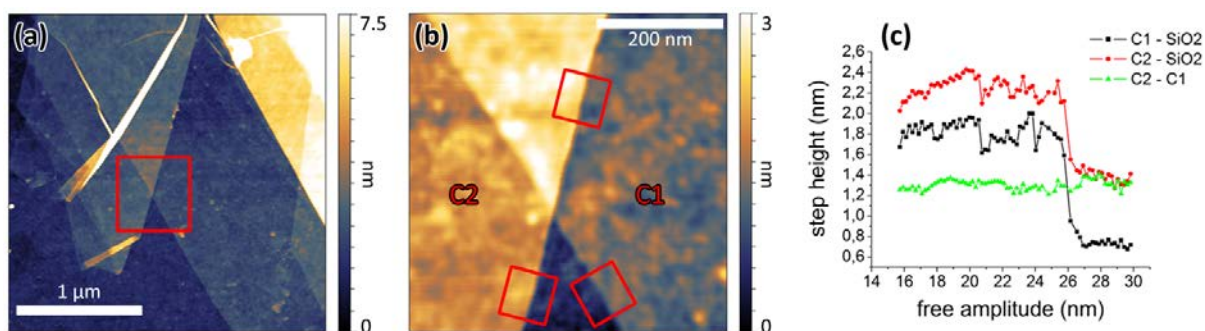


Figure 29. (a) TAFM image of two overlapping FLG films on SiO₂ (b) Zoomed in region from image (a), thickness measurements were done in the regions marked by rectangles, C1 and C2 representing each FLG film. In fig. (c), each point represents the measured thickness of the crystal C1 (black squares) and C2 (red circles) with respect to the oxide substrate, as a function of free amplitude. The thickness of crystal C2 measured where C2 is overlapping C1 is also plotted (green triangles). [T144]

In the current example, two FLG crystals were measured simultaneously, one overlapping the other. The free amplitude was varied from 16 nm to 30 nm. For each free amplitude setting a complete AFM image was acquired and the step heights in three regions were measured (marked by red squares): FLG C1 – oxide; FLG C2 – oxide and C2 overlapping C1. Starting with the 16 nm free amplitude and keeping the setpoint constant (8 nm), we can observe that at 26 nm free amplitude, the thickness measured on top of the oxide surface decreases almost instantly, by about 0.8–1 nm. However, the thickness measured at the overlapping region of FLG C2 (green triangles) stays constant. Furthermore, at such high free amplitudes, the value for the thickness of C2 corresponds to the thickness measured in the overlapping region. This indicates that the thickness at high free amplitudes corresponds to the real thickness of the flake. Furthermore, it shows that, in accordance with reports from the literature, a more reliable measure of thickness is the step height relative to another graphene or FLG substrate. It is generally accepted, that regions where the graphene folds onto itself give the most reliable measurement of thickness [15]. However, such folded regions are not always available in every experiment and most samples do not contain such regions, leaving no option, but to check the thickness relative to the oxide surface. The effect described here was checked on various FLG crystals, using different scanning tips. In each case, the effect could be observed, to a greater or lesser degree, with deviations in the thickness measured at low free amplitudes. In addition, we can also observe, that at low free amplitudes, the thickness of the flake shows much greater spread than in the case of large amplitudes (Figure 29c).

The effect of the setpoint amplitude was also investigated, with similar results as above. I have acquired AFM images on the same FLG flake with differing setpoint amplitude, keeping the drive amplitude constant (Figure 30). Here we also observe changes in the measured FLG thickness, through the stochastic changes in the measured height of the SiO₂ (see red and green line cuts in Figure 30b).

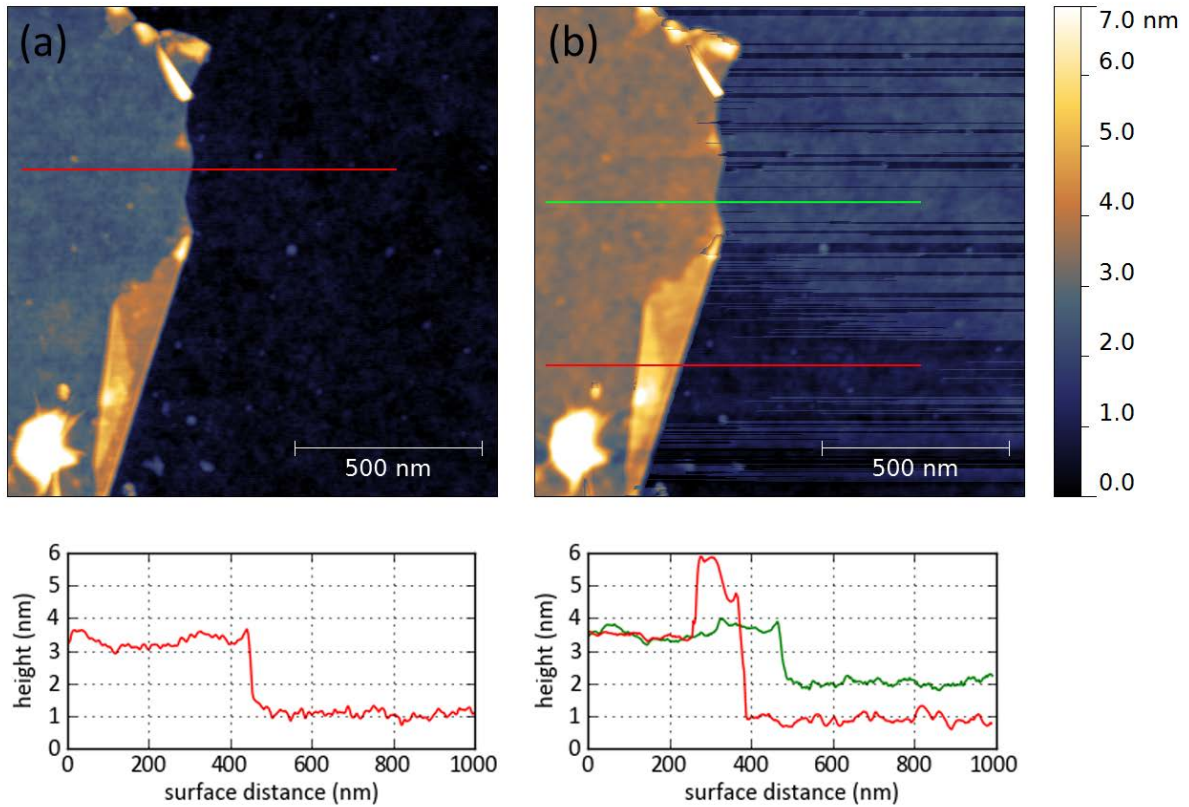


Figure 30. AFM images of the same FLG flake on SiO₂, acquired using differing setpoint amplitudes, keeping the drive amplitude constant. Figure (a) shows stable imaging while in (b) we observe stochastic changes in the measured height on the SiO₂. Red and green lines show selected height profiles on the images. In (b) the change in measured height is apparent from these graphs. Measurement parameters are, free amplitude: 23.5 nm, setpoints: (a) 17 nm, (b) 11.7 nm.

The presence of two “stable” thickness values for the flakes hints at the existence of a bistability in the measurement system. Clues to the origin of the bistability can be found if we investigate the amplitude response of the tip while changing the tip – surface distance. Such amplitude – distance curves (ADC) were obtained by reducing the tip sample distance from a value larger than the free amplitude to a minimal separation, where the amplitude

was reduced to about 10% of the free amplitude. The amplitude was not reduced all the way to zero because in this manner the reproducibility of the ADCs was poor.

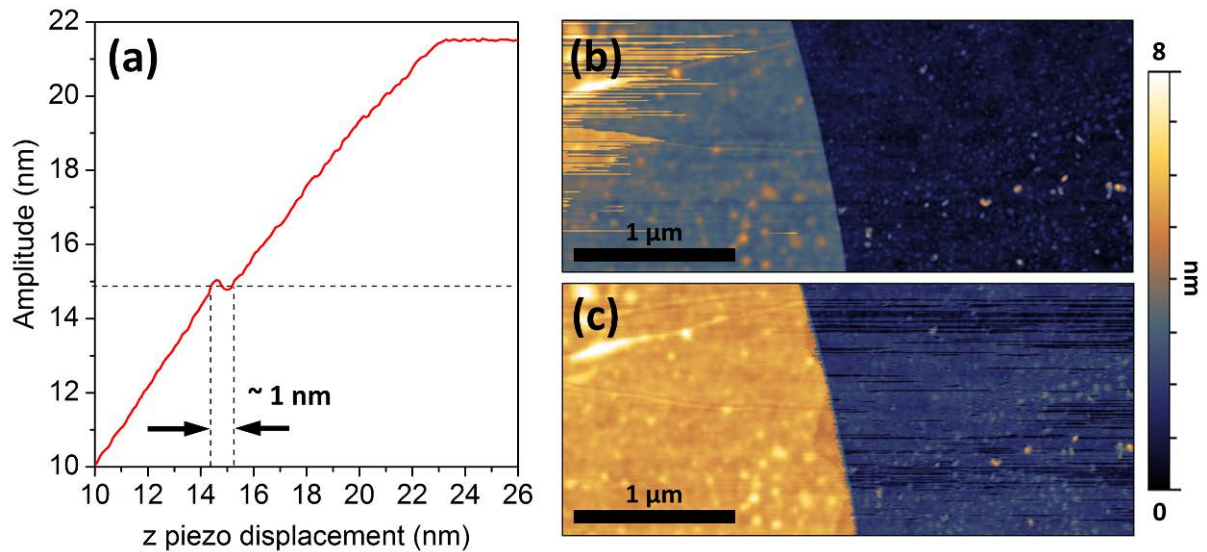


Figure 31. (a) The damping of the cantilever oscillation as a function of piezo displacement, recorded by approaching the tip towards the sample. The curve was taken on the surface of the FLG flake presented in (b). (b) TAFM image of a FLG flake, imaged at a setpoint of 15 nm and a free amplitude of 21 nm, near the bistability point in the AD curve. Random switching from one thickness to the other occurs. (c) TAFM image taken at a free amplitude of 21 nm when the instability point passes through the setpoint amplitude on the oxide. In this case, unstable imaging occurs on the oxide surface [T144].

A typical ADC is plotted on Figure 31a, recorded on a FLG surface, at 25.8 nm free amplitude. The striking feature of the amplitude curve is that at the amplitude value of 15 nm a jump can be observed. In this region, two different piezo displacement values correspond to the same amplitude, the difference being about 1 nm. This is important because the feedback electronics of the AFM works correctly only for a linear signal. If the free amplitude and setpoint value are selected in such a way that the setpoint coincides with the jump in amplitude, the feedback electronics may produce random switching from one displacement value to the other [T144]. Since the height signal is derived from the piezo displacement signal, random switching in height occurs. This behavior is presented in Figure 31. In one case Figure 31b, the imaging is stable on silicon oxide, while in Figure 31c. stable imaging is achieved over the FLG.

Changes in topography of such a magnitude (~ 1 nm) have been reported previously by Kühle et al. [173] on Cu clusters supported on a silicon oxide substrate. The origin of this change in

topography, as reported by the authors, is a jump in the amplitude response of the cantilever, with changing tip – sample separation, as seen in Figure 31a. Anczykowski et al, using time resolved numerical simulation of the tapping tip [182] pointed out, that the jump in amplitude marks a change in the sign of the tip sample interaction force. When the tip starts to approach the sample, the amplitude starts to decrease linearly. In this regime, long range attractive forces are responsible for the oscillation damping. Such forces are, the van der Waals interaction, electrostatic force, capillary force, etc. At a certain tip – sample separation a jump occurs in the amplitude (as seen in Figure 31a). This jump marks the onset of a region where, with further decreasing tip – sample distance, both long range attractive and short range repulsive forces act on the tip, i.e. the tip is in hard mechanical contact with the sample. After the jump, the damping of the oscillation increases further, but this time net repulsive forces characterize the tip sample interaction and the contact time of the tip also produces a jump [183].

Let us now investigate the onset of unstable imaging and the amplitude response of the tip simultaneously. In Figure 32 we can observe the ADC on a FLG flake seen in Figure 31b,c and the supporting oxide surface at three different free amplitude settings: 24 nm, 26 nm and 28.5 nm. The setpoint value used during TAFM image acquisition is 15 nm. We can observe the presence of net attractive and net repulsive regimes of interaction on both surfaces. One important characteristic is worth pointing out: below 21 nm free amplitude the measurement setpoint is in the net attractive regime for both the oxide and FLG surfaces. Increasing the free amplitude the ADC shifts and at 21 nm the setpoint is at the instability point on the oxide. It is exactly at this free amplitude, that the TAFM image in Figure 31c was acquired. Because of the presence of two piezo displacement values for a certain amplitude, the feedback electronics cannot distinguish between these two, as it needs a linear signal to work with. Therefore random switching of the height on the oxide surface can be seen [T144], similar to the effect observed by Kühle et al. [173, 184]. Increasing the free amplitude further, the setpoint on the oxide will be in the net repulsive regime, and on the FLG surface in the net attractive region. At 26 nm free amplitude, the setpoint is at the jump in amplitude on the FLG, leading to unstable imaging (Figure 31b). Plotting the step height dependence on the FLG as a function of free amplitude we obtain the graph in Figure 32c.

The plot shows a jump in the measured height, at each free amplitude value, where the setpoint crosses the jump in amplitude (observe the regions separated by gray lines).

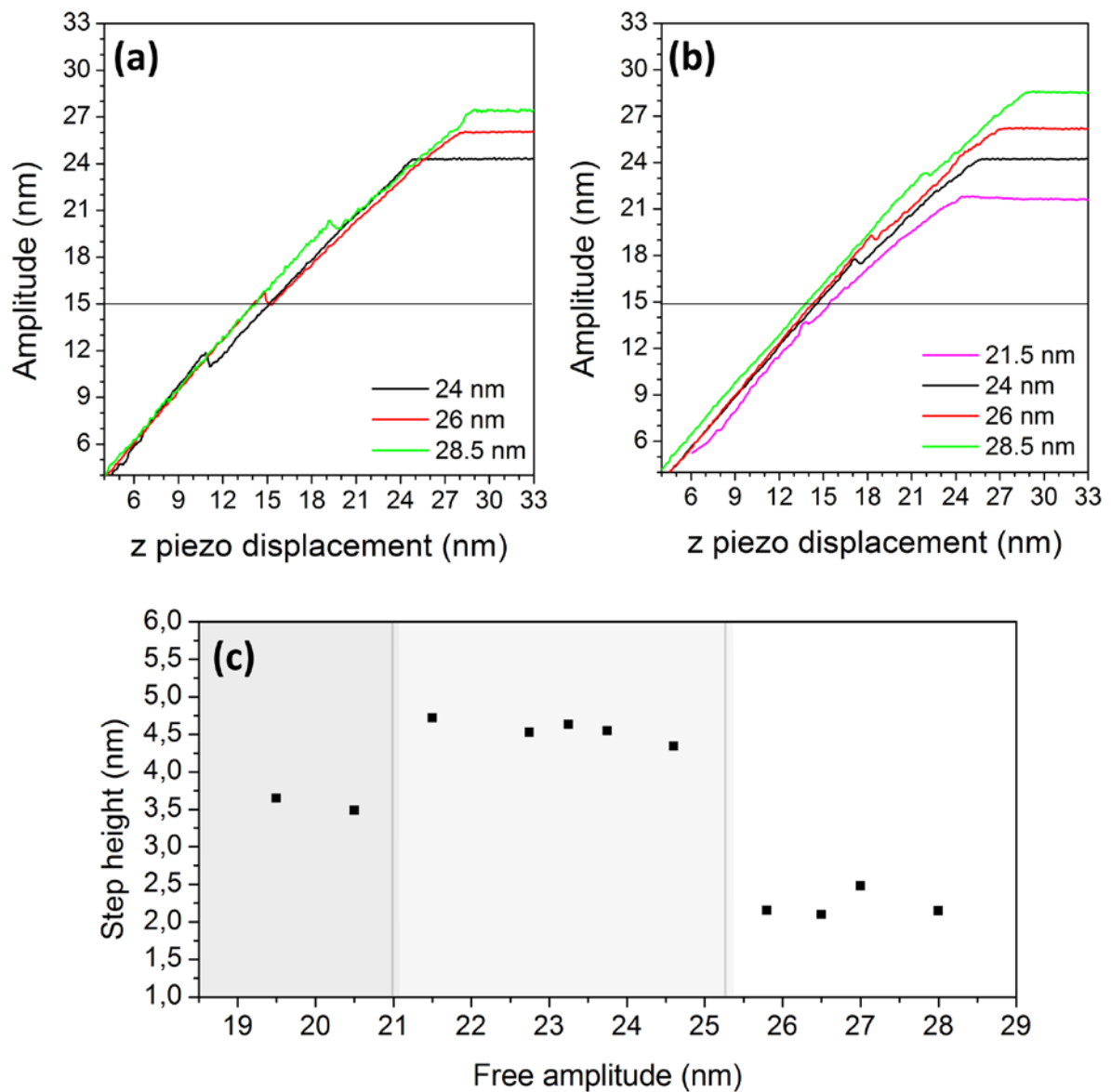


Figure 32. Amplitude - distance curves on the FLG (a) and oxide (b) surface at different free amplitudes, measured in the region presented in Figure 31b. A horizontal black line at 15 nm amplitude shows the setpoint used during measurements. At ~26 nm free amplitude the setpoint crosses the jump in amplitude for the FLG. For the oxide surface such a crossing is experienced at free amplitudes around 21 nm. (c) FLG step height plotted as a function of free amplitude. Two jumps in height can be observed: the jump at ~26 nm and at ~21 nm, the free amplitude values at which the instability crosses the setpoint amplitude. [T144]

A steep decrease in the step height at around 26 nm free amplitude from 4.5 nm to 2.25 nm shows the onset of the repulsive regime for both the oxide and FLG flake. Considering the

information in Figure 29, that at high free amplitudes the step heights measured relative to the oxide and the flake surface itself correspond, we can say that a more precise measure of the step height can be obtained, if the measurement is performed in the repulsive regime on both oxide and FLG.

I have shown that at certain setpoint or free amplitude settings of the vibrating AFM tip the measured thickness of FLG flakes changes. Furthermore, I have shown that generally the thickness of FLG flakes is correctly reproduced by the AFM at high free amplitude or at low setpoint settings. To support these claims and to get a better understanding of the reasons for the large difference in thickness, more than 1 nm in certain cases, a theoretical modeling of the tip – surface interaction can be very useful.

3.2.4. A model for the tip – surface interaction and measurement regimes

The complex behavior of the tip can be best modeled by taking into account the specific shape of the cantilever, which has multiple vibrational eigenmodes [185]. However, in this present case, such a treatment is not necessary. Taking a more simple approach of modeling the tip oscillation by a spring – point mass system has proven effective in giving a qualitative description of the kinds of behavior observed in the present experiments [143, 184, 183, 186]. In this approach, the tip motion can be modeled by a driven harmonic oscillator. We can start from Newton’s equation of motion:

$$(XIII). \quad m\ddot{z} + kz + \gamma\dot{z} = F(t)$$

Here, the mass m is a kind of effective mass of the cantilever – tip ensemble [186]. In the case of TAFM, we are interested in $z(t)$ solutions to the above differential equation for a periodic driving signal $F(t) = F_0 \sin(\omega t)$, taking into account the forces acting between the tip and sample surface (F_{TS}):

$$(XIV). \quad m\ddot{z} + kz + \frac{m\omega_0}{Q}\dot{z} = F_{TS}(z) + F_0 \sin(\omega t),$$

Where m , ω_0 , k , Q and F_0 are the cantilever effective mass, angular resonance frequency, spring constant, quality factor and the amplitude of the driving force. The angular resonance

frequency is $\omega_0 = \sqrt{k/m} = 2\pi\nu_0$ and the quality factor is defined as: $Q = m\omega_0 / \gamma_D$, it is essentially a dimensionless measure of the damping of the oscillation, where γ_D is the damping coefficient. The quality factor is usually in the 400 - 600 range in air, for the cantilevers used in the present experiments.

The forces acting between the tip and the sample (F_{TS}) can be separated into two categories: attractive forces and repulsive forces. Short range repulsive forces arise when the tip is in hard mechanical contact with the sample and their source is ionic and Pauli repulsion between the atoms and molecules of the tip and surface. Long range attractive forces are for example the van der Waals force and the capillary force, which arises due to the ever present water layer on the sample surface when measuring under ambient conditions [187, 188]. When not in mechanical contact with the sample surface, the contribution to F_{TS} comes from these long range attractive forces. Once in contact with the surface, the force is modeled by simple contact mechanics. The force acting on deformable bodies in mechanical contact was first described in a continuum model by Hertz in 1881 [143]. The AFM tip studied here is made out of silicon and has a tip radius of curvature smaller than 10 nm. An approximation that is suitable to model this hard, but compressible tip with a similarly hard and compressible surface, i.e. the SiO₂ or SiO₂ supported graphene is the Derjaguin-Muller-Toporov (DMT) model [189]. This model is based on hertzian contact mechanics, but adds the effects of adhesion forces acting outside the contact area, between the tip and sample in contact. This model has proven very successful in describing the behavior of AFM under the present experimental circumstances [143, 172, 182, 183, 188] and has become one of the standard ways of calculating tip surface interaction forces in AFM [143, 186]. The repulsive force in the DMT model is given by:

$$(XV). \quad F_{rep}(z(t), z_{TS}) = \frac{4E\sqrt{R}}{3-3\eta_S^2} (a_0 - z(t) - z_{TS})^{3/2}$$

$$\frac{1}{E} = \frac{1-\eta_T^2}{E_T} + \frac{1-\eta_S^2}{E_S}$$

where E_T and E_S are the tip and sample elastic modulus and η_T and η_S are the Poisson's ratios. The relevant quantities, for the tip sample separation z_{TS} and the position of the tip

at a given time $z(t)$ are shown in Figure 33. The constant a_0 is comparable to interatomic distances and is introduced to avoid divergence (see below). The adhesion force is given by $F_{adh} = 4\pi R\varepsilon$, where R is the tip radius of curvature and ε is the surface energy. The van der Waals force for a sphere – flat surface geometry is:

$$(XVI). \quad F_{vdW}(z(t), z_{TS}) = -\frac{HR}{6(z(t) + z_{TS})^2},$$

where H is the Hamaker constant. The van der Waals force diverges if the tip comes into contact with the sample. Therefore, for tip sample separations smaller than atomic distances ($z(t) + z_{TS} \leq a_0$) F_{vdW} is made to be equivalent to the adhesion force from DMT theory. A plot of this force can be seen in Figure 33b. Using this force and evaluating the equation of motion numerically we get the amplitude response of the TAFM tip at a given tip sample separation (z_{TS}).

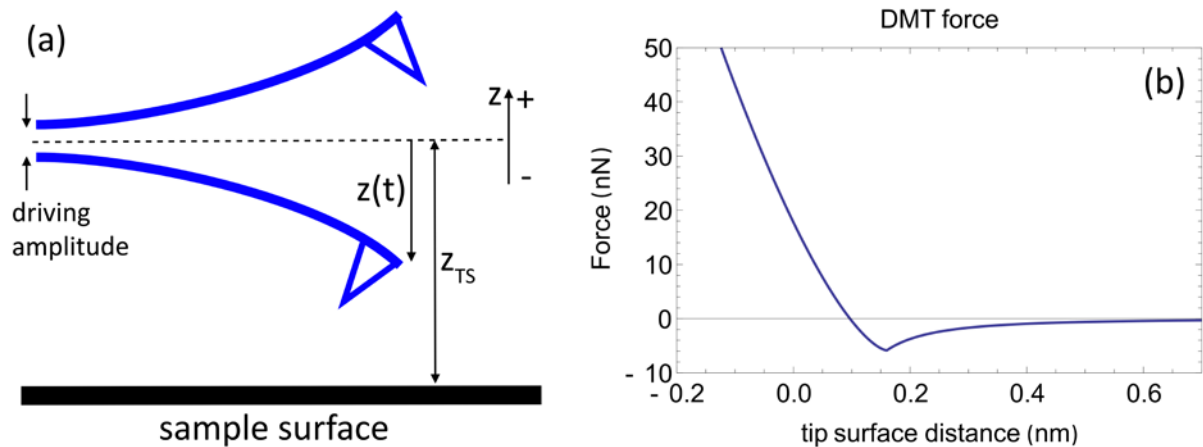


Figure 33. (a) Scheme of the AFM tapping, with relevant quantities noted. Arrow shows the coordinate system used during this study. (b) Plot of the force acting between the tip and surface, as a function of tip – sample separation.

Based on the model described above, I have calculated ADCs for a tip sample configuration used for measurements, namely a single crystal silicon tip, with a 10 nm tip radius and a SiO₂ surface, using only contact and van der Waals forces (Figure 33b). In Figure 34a I have plotted the ADC for a tip vibrating with a 15.7 nm free amplitude. The parameters used for calculations are as follows: $H = 6.4 \cdot 10^{-20}$ J, $\varepsilon = 31$ mJ/m², $E_T = 130$ GPa, $E_S = 70$ GPa, $\eta_T \approx \eta_S = 0.17$; with the tip and cantilever properties being: $R = 10$ nm, $k = 40$ N/m, with the

tip driven at the resonance frequency of $\nu_0 = 300$ kHz. We can see from the ADC, that the numerical calculations reproduce the discontinuity in the amplitude response observed in experiments (see Figure 32a,b). By plotting the average force, that the tip experiences during an oscillation cycle it becomes apparent that, as discussed before, the net force changes from attractive to repulsive, at the point where the instability occurs in the ADC. In the net attractive region (negative average force) the amplitude reduction occurs mostly due to attractive forces (van der Waals, etc.). This is sometimes called “soft tapping”, since the tip sample forces are minimal. Further reducing the tip – sample distance, the tip comes into hard mechanical contact with the sample at each oscillation period, making the net force repulsive in nature (positive average force). At even smaller tip – sample distances, the damping of the amplitude is due to the strong repulsive forces acting between the atoms of the tip and surface. At the discontinuity, alongside the jump in the amplitude, the contact time of the tip with the sample increases in a step like fashion as well, as shown by Garcia et al. [183].

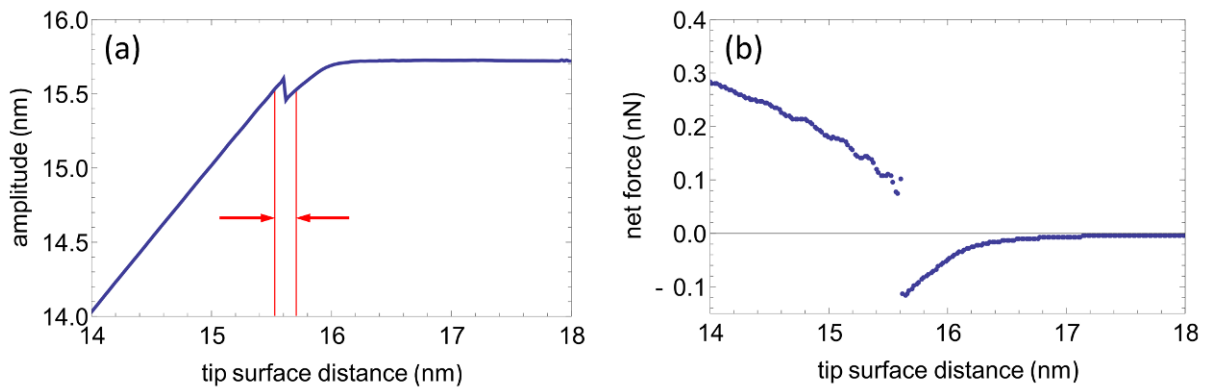


Figure 34. (a) Numerically calculated ADC for an AFM tip of 10 nm tip radius and a cantilever of 40 N/m spring constant. The forces acting between the tip and sample are the DMT contact force and van der Waals interaction. The free amplitude of the oscillation is 15.7 nm. Red arrows show the size of the difference in tip sample separation, at the jump in amplitude. (b) Plot of the mean force experienced by the tip during an oscillation period. There is a marked jump from attractive to repulsive net force, exactly where the jump in amplitude occurs.

The model described above does not give an exact quantitative description of the tip amplitude response. Still, it can be used in elucidating some of the physical processes responsible for the very large difference in the thickness of graphene, when measuring in the net attractive and net repulsive regime, respectively. Plugging in the parameters for the

tip and sample material, tip radius of curvature, etc. the plots of the ADC look like the one in Figure 34a. The ADC curves reproduce the discontinuity in amplitude, but the size of the z_{TS} difference separating the two amplitude solutions is only a fraction of a nanometer (see Figure 34a). This can in no way be responsible for the very large z_{TS} difference, sometimes more than 1 nm, observed during experiments (see Figure 31a), which leads to the large differences seen in the thickness. Parameters like the free amplitude have some influence over the position and magnitude of the calculated amplitude jump - z_{TS} difference, but do not significantly change the behavior. As also pointed out by Garcia et al [183] and shown in the present calculations, the size of the amplitude jump diminishes with increasing free amplitude (Figure 35b). I have also calculated the dependence on the tip radius of curvature, from a 5 nm tip radius to a 25 nm tip radius (Figure 35a). We can see that in this case the magnitude of the z_{TS} difference increases with increasing tip radius but the effect is still subtle and the largest tip radius, 25 nm, being about twice as large as the typical single crystal silicon AFM tip radius. We can get a better description of the tip amplitude response by making a refinement to the current model.

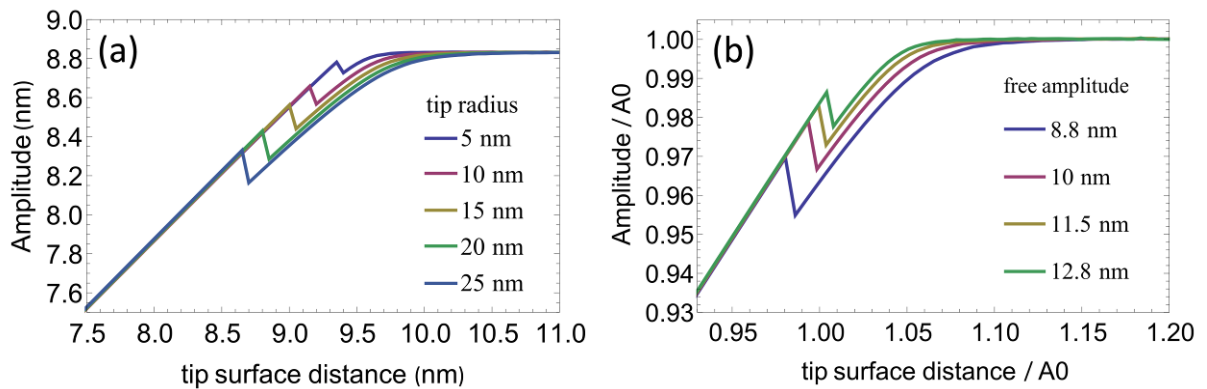


Figure 35. Changes in the onset and magnitude of the jump in amplitude for different values of the tip radius of curvature (a) and for different values of the free amplitude (b). For easier comparison, the ADC curves in (b) have been normalized to the free amplitude (A_0). The tip radius in the case of (b) is 10 nm.

When examining the long range forces acting on the tip in the vicinity of the sample, we have neglected nearly all forces, except for the van der Waals. But there can be other forces at play, from electrostatic and magnetic interaction, to capillary forces [143, 186]. In our particular case, the capillary forces may play an important role in the damping, due to the ever present water layer on SiO_2 , under ambient conditions [190, 191]. Verdaguer et al. have

shown that on SiO₂, 6 to 7 monolayers of water can form above 75% relative humidity [190]. There is evidence that even graphene or graphite, which is a hydrophobic material, can support a water layer [192, 193]. To get a more accurate picture of the physical processes leading to the measurement of anomalous thickness values, the presence of a water layer on the sample must be taken into account.

Since the objective of this work is to reveal the kinds of physical processes responsible for the large thickness jumps observed experimentally and not a quantitative description of the AFM measurement process, the capillary force is taken into account using a simple model. I have implemented a model for the capillary force used by Zitzler et al. to successfully explain the relative humidity dependence of the onset of the jump in amplitude [188]. The source of the capillary force is the formation of a capillary neck if the AFM tip touches the sample surface which has a water layer of thickness h (see Figure 36). The meniscus is considered to form upon approaching the tip to the surface at a distance of $d_1 = 2h$. Since we are striving to a qualitative description, we neglect the presence of the water as a dielectric, which would influence the magnitude of the van der Waals force and capillary condensation due to the presence of the sharp AFM tip near the sample [186, 187]. However it needs to be mentioned that due to capillary condensation the amount of water present around the tip would certainly increase [187]. As the tip starts to retract from the surface, the meniscus breaks at a distance d_2 , which is larger than d_1 . The break distance d_2 is given by Willet et al. [194] for a sphere plane geometry as:

$$(XVII). \quad d_2 = \sqrt[3]{V} - \frac{V^{2/3}}{5R}, \text{ where}$$

$$(XVIII). \quad V = 4\pi R h^2 + 4\pi h^3 / 3 + 2\pi r^2 h$$

$$r = \sqrt[3]{\frac{3\pi\epsilon R^2}{E}}$$

In the above expressions V is the volume of the displaced water, as the tip touches the sample surface and from the DMT model we have r , the radius of the contact area.

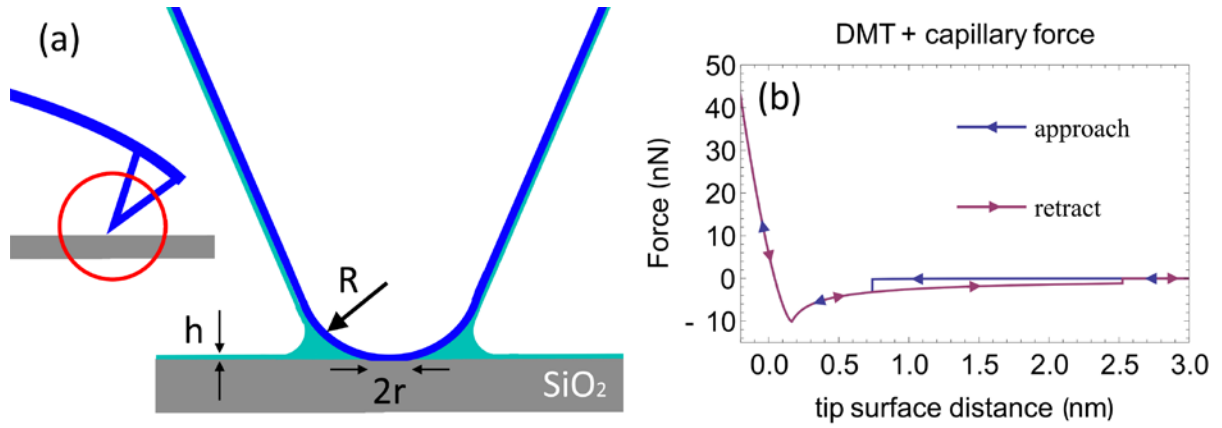


Figure 36. (a) Formation of a capillary neck around the AFM tip in contact with the sample surface, due to the water displaced by the tip. The thickness of the water layer is h , the tip radius of curvature is: R and r is the radius of the contact area. (b) Plot of the force acting between the tip and sample, for a water layer thickness of 3.7 \AA .

When the meniscus is present around the tip a capillary force is added,

$$F_{TS} = F_{DMT} + F_{vdW} + F_{cap} \quad [195]:$$

$$(XIX). \quad F_{cap} = -\frac{4\pi g_{water} R}{1 + \frac{z_{TS} + z(t)}{h}}$$

Here, g_{water} is the liquid – vapor interfacial energy of water, equal to 72 mJ/m^2 [188]. A plot of the tip – surface force can be seen in Figure 36. An estimate of the water layer thickness can be obtained from the work of Xu et al. [191], who have directly measured the thickness of a single monolayer of water on a mica surface, which added up to 0.37 nm . Figure 37a shows the ADC plotted in Figure 34a and four other curves, calculated using three different values for h : 0.18 nm , 0.37 nm and 0.5 nm . It becomes immediately clear that if we take into account the capillary force, the difference in z_{TS} at the instability between the two amplitude solutions increases dramatically to about 1 nm , as observed in experiments.

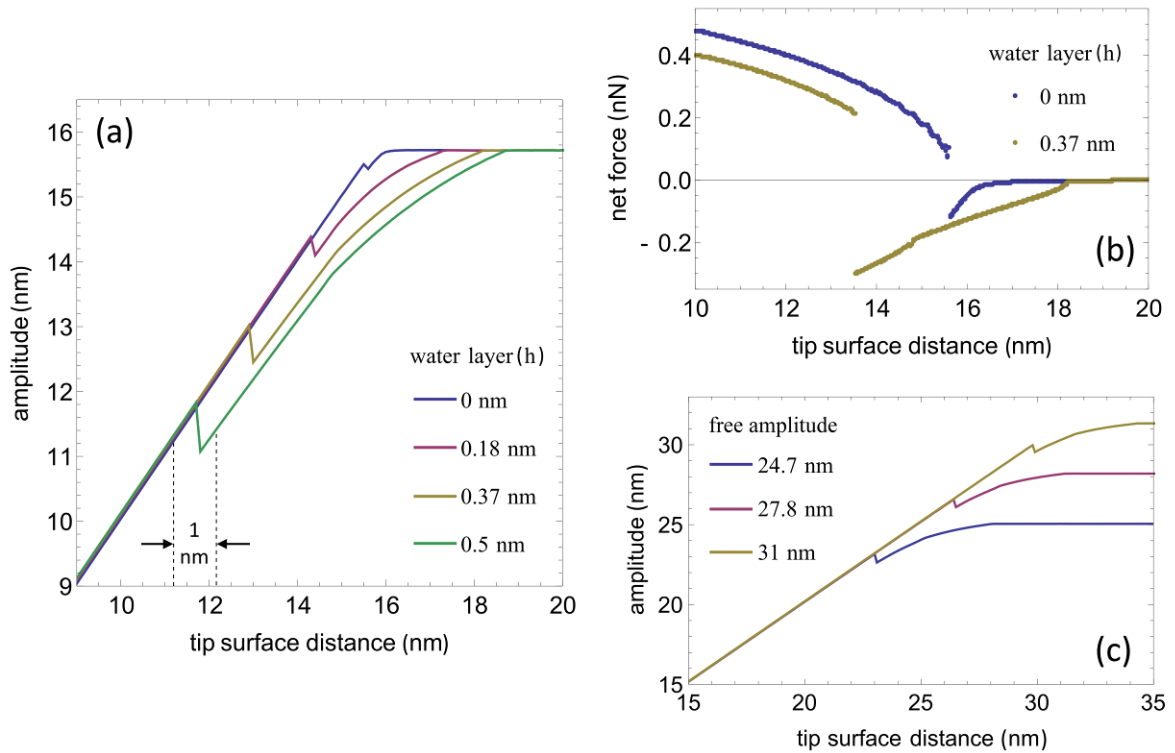


Figure 37. (a) ADC plotted for different values of the water layer thickness. (b) Plot of the net force experienced by the tip over an oscillation cycle, for a range of tip sample separations. In the presence of the capillary force, the attractive forces are much larger than if we don't have a water layer. (c) ADCs for free amplitude values similar to experiments (see Figure 32a).

As expected, the net force experienced by the tip over an oscillation cycle (Figure 37b) is much larger than in the case of no capillary force. Furthermore, the tip oscillation state jumps to the net repulsive regime at much smaller tip sample distances. For large water layer thicknesses and small free amplitudes of the tip, the amplitude can be reduced to all the way to zero without a jump to the repulsive regime (data not shown). However, for a fixed water layer thickness and changing free amplitude, the instability occurs at roughly the same $z_{TS}/\text{free amplitude}$ ratio, displacing the instability in amplitude (Figure 37c and Figure 35b). Therefore, at a given measurement setpoint the amplitude jump can be offset with changing the free amplitude of the tip, as we have seen in experiments (Figure 32).

One more important insight is that the amplitude response of the tip in the attractive regime is strongly dependent on the nature and strength of the tip - surface forces (Figure 37a) and is influenced considerably by measurement parameters, such as the tip radius of curvature and free amplitude (Figure 35a, b). This becomes important if the measurement is done in

the attractive regime and certain parameters, such as the water layer thickness, may change during scanning. Such an instance occurs when the tip moves from graphene to the supporting SiO₂, which has a differing hydrophobicity and as a result, most likely different adsorbed water thickness. Thus, we can say that it is more prudent to measure the thickness of nanosized objects, such as graphene, in the repulsive measurement regime, simply because the amplitude response is less prone to be perturbed by the particular experimental conditions during measurement.

It needs to be stressed that the above calculations have been done only for the SiO₂ surface – silicon tip ensemble and not for a SiO₂ – graphene – tip system. To study the latter system theoretically, we would need to know the mechanical properties of the graphene – SiO₂ support. Since graphene is only a single atomic layer on top of the support, in a rough approximation we could handle this system as having the mechanical properties (Young's modulus, Poisson ratio) of SiO₂, with the Hamaker constant, surface energy and hydrophobicity of graphite. Since the mechanical properties are the ones that largely determine the repulsive force, we would not expect much difference in the amplitude response of graphene and SiO₂ in the repulsive regime. However, the behavior of the tip in the attractive regime would be markedly different on graphene. The correct description of the mechanical properties of the graphene – support system is beyond the scope of this work, but two general conclusions related to graphene thickness measurements can be drawn. One is that the contribution of capillary forces determines the large jump in tip – sample separation, when the tip switches from the net attractive to the net repulsive regime. Second, the amplitude response of the tip is much more sensitively affected by specific measurement conditions in the attractive regime, making thickness measurements in this regime prone to unforeseen perturbances. This can be observed in Figure 29c, where the spread of thickness values for the FLG flakes, measured relative to the support shows a higher spread when measured in the net attractive regime, than when the measurement is performed in the net repulsive regime.

3.2.5. Reproducible thickness measurements of FLG

Calculations have shown that performing measurements in the net attractive regime can lead to unreliable thickness measurements. This is because the tip amplitude response is

strongly affected by the specific material characteristics of the sample, for example the hydrophobicity. We have two solutions to this conundrum. Either the thickness measurement is performed over a sample region which is homogeneous, like the case of a graphene flake folding onto itself. We have observed that in this case, the thickness value measured is unaffected by the free amplitude or the amplitude setpoint chosen (Figure 29 and Figure 30). A second option is to choose the free amplitude and setpoint in such a way as to have the setpoint below the jump in amplitude on both the oxide support and the graphene – FLG , i.e. to measure in the net repulsive regime. Experiments show that in this case the thickness measured, relative to the SiO₂ is the same as the one measured in a region where the thickness is measured relative to another FLG surface (Figure 29c and Figure 30). This means that the thickness measured in the repulsive regime is the true thickness of the graphene - FLG flake. As further evidence for the correctness of measuring thickness in the net repulsive regime, I have cross checked the thickness values measured by TAFM with measurements of thickness using Raman spectroscopy.

Soon after the discovery of graphene it became apparent that the Raman spectra of FLG is very sensitive to the number of graphene layers [162, 196]. The three prominent peaks of graphene and FLG are the so called D (~1350 cm⁻¹), G (1580 cm⁻¹) and 2D (~2700 cm⁻¹) bands. The 2D peak is especially sensitive to the number of graphene layers. It stems from a double resonant process, during which an excited electron suffers inter-valley scattering by two phonons, with opposite momentum [162]. This peak is a well defined single peak for a single layer of graphene and has four components for bilayer graphene. Above two layers, three to five layers can still be distinguished from the bulk signal of graphite. This method became the gold – standard of graphene thickness determination. For the sake of clarity it needs to be mentioned that in the literature the 2D peak is sometimes referred to as G', for historical reasons [162], or D* [197]. However, the 2D notation is the most prevalent.

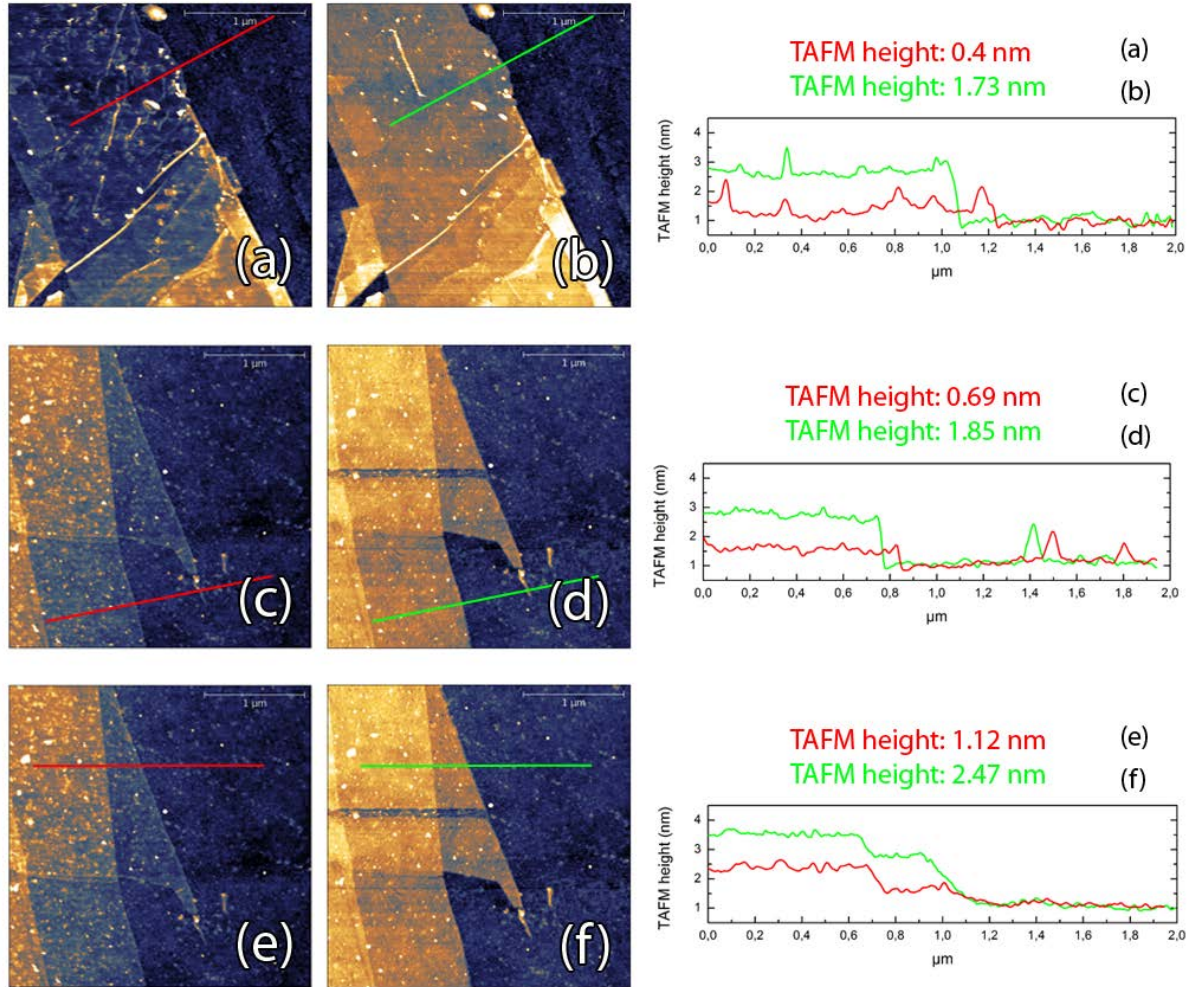


Figure 38. TAFM images of single layer (a, b); bilayer (c, d); three layer (e, f) flakes (each image is $2.5 \mu\text{m} \times 2.5 \mu\text{m}$). The images were acquired using a constant setpoint amplitude and two different free amplitudes, one higher (a, c, e) and another one lower (b, d, f). In the first case (a, c, e) the setpoint is in the repulsive regime for both oxide and FLG, while in the latter case (b, d, f) imaging is in the attractive regime. Line cuts (colored markers) taken on each image show the thickness in each measurement region [T144].

Figure 38 shows TAFM images of FLG flakes, with different thicknesses. The thickness of the flakes was measured in both the net repulsive and net attractive regimes. In the repulsive regime, the thickness of the flakes turned out to be: 0.4 nm, 0.69 nm and 1.12 nm. These thickness values would correspond to single layer, bilayer and three layers of graphene. To cross check the thickness values, the Raman spectra on these flakes was measured, using a laser with a 488 nm wavelength and a Raman spot size of $2 \mu\text{m}$ [T144]. 2D peaks of the Raman spectra are plotted in Figure 39. The spectra for the flake having 0.4 nm thickness can be fitted with a single Lorentzian, which shows that it is indeed a single layer of graphene [196]. The next flake which has a thickness of 0.69, or roughly two times the van der Waals

spacing of graphite (0.335 nm), shows a 2D peak which has four components, indicating that it is indeed a bilayer [196]. In accordance with the measurements of Ferrari et al. [196] the flake having 1.12 nm thickness, or a three layer graphite has a 2D peak similar to bulk graphite.

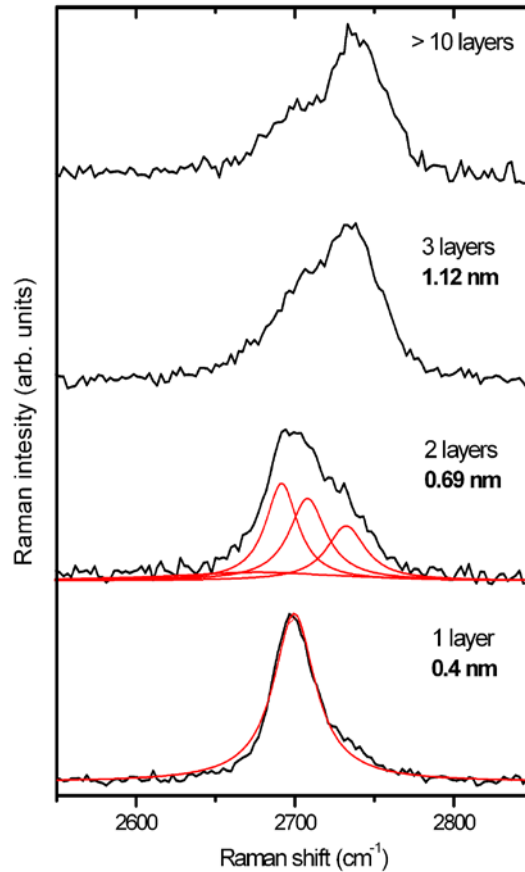


Figure 39. Raman spectra of FLG having 1, 2, 3 and >10 layers (scaled to have similar height of the 2D peak). The spectra are displaced for easy comparison. For each sample, I show the height measured by TAFM, in the net repulsive regime. The four components of the 2D peak in bilayer graphite are plotted.

The systematic AFM measurements and calculations have shown us that the TAFM measurement of graphene is best performed in the net repulsive interaction regime. Usually the amplitude setpoint is chosen in such a way as to be as near as possible to the free amplitude in order to minimize the forces acting on the tip and sample in order to minimize tip – sample damage, but as we have seen this may not be the correct setting. The evidence presented here points to the fact that the variation of the reported thickness of graphene among different research groups is largely due to the unreliability of TAFM measurements in the attractive regime. It is worth noting here, that during our measurements at high free

amplitude and low setpoint settings, no damage to either the sample or tip were encountered. The results presented here may be extended to the measurement of other nanostructures where the deviation induced by the difference between the two stable states of vibration may be comparable to the size of the nanostructure. Furthermore, this study has shown us what kinds of factors one needs to take into account when measuring and interpreting topography and size measurements of nanostructures with TAFM:

- one has to consider the influence of changing surface material properties, such as hydrophobicity and mechanical properties,
- the measurement setpoint and free amplitude of the tip have to be chosen in such a way that the measurement is performed in the net repulsive tip – sample interaction region.

3.3. Preparing graphene nanoarchitectures with zigzag edges

The electronic properties of GNRs are predicted to depend on their size and the crystallographic structure of the ribbon edges (see chapter 1.4.2). Chemical routes of GNR preparation that are able to differentiate between the zigzag and armchair type edge terminations of graphene are highly sought after as an alternative to standard lithography methods like electron beam lithography [120], due to the scalability of such chemical processes. Several theoretical investigations show that the armchair and zigzag edges of graphene have differing reactivity [198, 199] and energetic stability [200], these studies all point to the possibility of anisotropic etching. Indeed, recently the crystallographic orientation dependent etching of graphite by metal nanoparticles [201] has been successfully implemented on graphene samples [133]. In the case of graphite etching, Ci et al. have shown evidence that zigzag edges are produced [134]. However, up to now control over the patterning has not been demonstrated, as the catalytic particle trajectories cannot be guided at will. Furthermore, any lithographic technique would need to be implemented on an insulating substrate, to facilitate the study and use of the as prepared graphene nanostructures in electronic devices. In this study, I present a controllable and anisotropic etching process which circumvents all these problems and I show that we can use it to obtain graphene ribbons with zigzag edges.

The etching of graphite surfaces in an anisotropic manner has been achieved more than a decade ago by simply heating the sample in air at 650°C [202]. After such a treatment the surface of graphite shows a range of hexagonal pits. These pits form through the etching of the graphite basal plane by the oxygen in the atmosphere. Such etch pits have a hexagonal structure and were shown to have armchair type edge terminations [202]. This type of oxidation technique shows promise to pattern the surface of graphene layers in a crystallographically selective way. Starting from this premise, I have studied the oxidation of graphene layers in an oxygen containing atmosphere.

3.3.1. Sample preparation and experimental methods

For all patterning experiments the graphene samples were prepared by micromechanical cleavage [5], and supported on single crystal silicon wafers having a 90 nm thick SiO₂ capping layer. After preparing graphene samples in this way, they were exposed to an oxygen – nitrogen atmosphere at 500 °C. The treatment was carried out in quartz tube inside a resistively heated furnace. During the 40 minute oxidation, a mixture of high purity O₂ (99.9995%) and N₂ (99.999%) was used, with a flow rate of 700 ml/min and 1300 ml/min, respectively. A TAFM image of such an etched graphene layer can be seen in Figure 40a. As also shown by Li et al [203], this treatment produces circular etch pits on the graphene surface [T129]. If compared with the results reported in ref. 202, this indicates that oxidation of graphene is different as compared to that of HOPG. A possible source of the differences can be the interaction with the substrate.

It is well documented that when heating graphite in the presence of molecular oxygen, at temperatures below 875°C, oxidation only occurs at defect sites [204]. At these defect sites the carbon gasification reaction has lower activation energy, determined by the specific structure of the defect [205]: vacancy, pentagon-heptagon pair, grain boundary, etc. The temperature used in this study is far away from the gasification temperature of the basal plane of graphite (875°C) [204] but still, etch holes are generated in the basal plane of the graphene flake in a stochastic manner all throughout the oxidation process. This is apparent from the fact that the etch pits have different diameters (Figure 40a). A large spread in the diameter happens when, assuming a constant etch rate, new pits are generated throughout the oxidation time interval [204]. This stands in contrast to defect oxidation, where the size

of the etch pits remains the same and grows monotonously as a function of etch time [204]. The surprising fact that on graphene these etch pits are generated in a stochastic manner throughout the basal plane, at such low temperatures (500°C), may be due to interaction with the SiO₂ support. The mechanism for increased pit nucleation may be a localized reduction in the energy barrier for carbon removal due to two factors, one of these being a high local curvature of the graphene layer conformed to a rough SiO₂ support [206], or the presence of charged impurities in the oxide [125, 203]. The fact that the etch pits are circular and that they get generated in a stochastic manner make this kind of oxidation unsuitable for crystallographically oriented, well controlled patterning. To overcome these drawbacks, a novel graphene patterning process was attempted [T129].

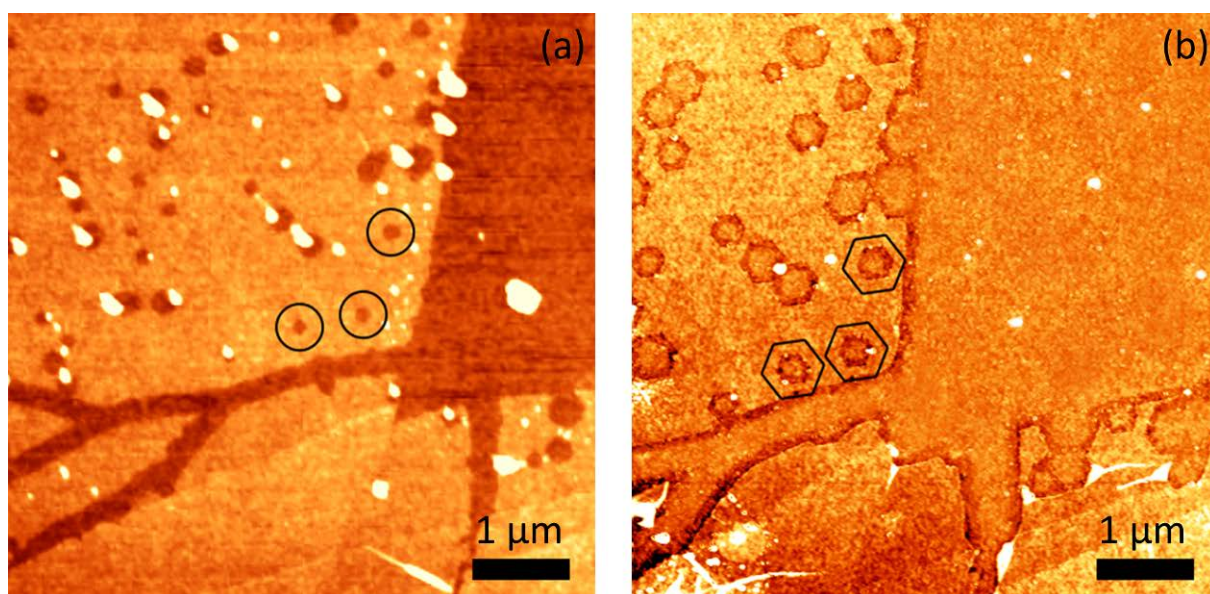
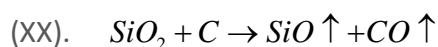


Figure 40. (a) AFM images of a graphene layer oxidized in a mixture of O₂ and N₂ gas, at 500°C for 40 min and (b) the subsequent growth of hexagonal holes in the graphene, after annealing at 700°C in an Ar atmosphere. Specific oxidation holes are marked by black circles, and the same etch pits are marked by hexagons after carbothermal etching. The long, branching etch marks are due to the etching out of grain boundaries. White spots on the AFM images are the remnants of the Scotch tape material and have no observable effect on the oxidation or annealing processes [T129].

The oxidation of carbon can occur even in the absence of molecular oxygen in the presence of SiO₂. The reaction of SiO₂ and C is used to form SiC at a temperature of 1754°C [207]. However, Byon et al. have shown that a partial reduction of SiO₂ and oxidation of carbon can occur at much lower temperature of 830°C [208]. They have used CNTs to etch nanosized

trenches into a SiO₂ surface. During this process the SiO₂ is partially reduced to SiO and the carbon oxidized to CO:



Both reaction products of this so called “carbothermal” etching, CO and SiO, are volatile at high temperatures and thus get swept away from the reaction site by applying a gas flow over the sample, enabling the very slow removal of carbon [208]. This procedure was adapted to etch graphene flakes supported on SiO₂. In the initial experiment, the flakes etched by oxidation in a N₂/O₂ mixture (Figure 40a) were subjected to another annealing treatment, this time in inert, Ar gas (99.99%), with a flow rate of 1000 ml/min. The result of the carbothermal etching is shown in Figure 40b and the temperature profile of the annealing in Figure 41.

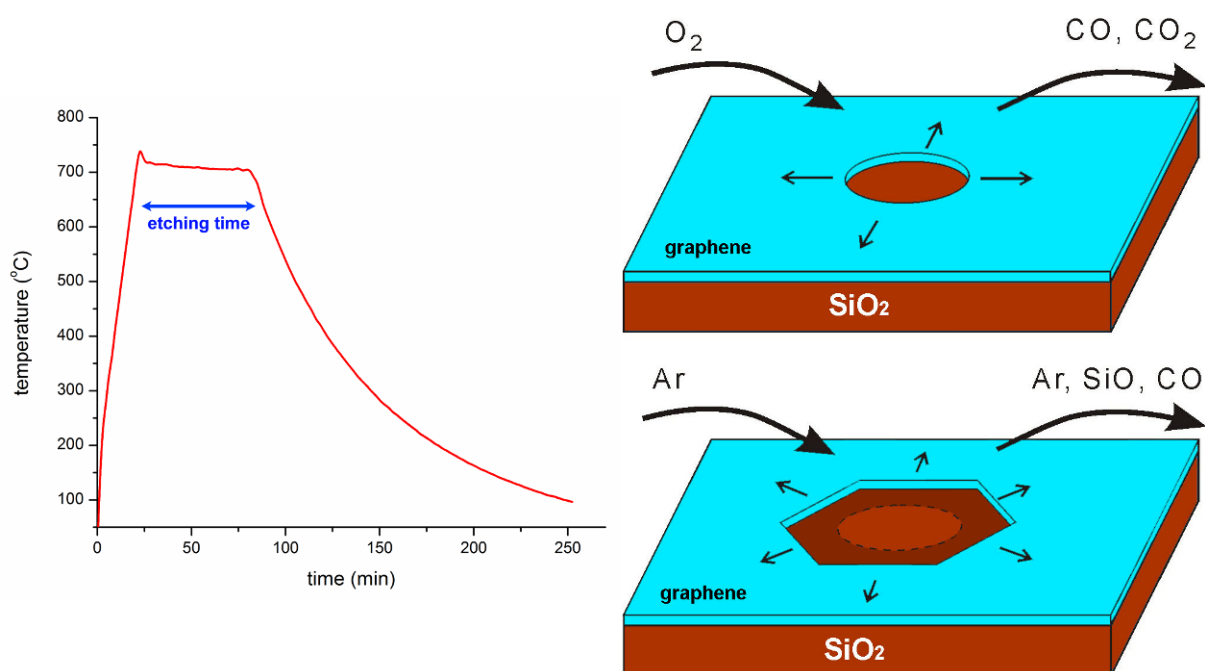


Figure 41. (left) Graph showing the heating and cooling cycle of the annealing. The etching time referred to in the text is the region of 700°C of the treatment time. (right) Outline of the oxidation with molecular oxygen at 500°C (top) and subsequent carbothermal etching process at 700°C (bottom).

After this second treatment step, the existing circular etch pits continued to grow in size but we can observe that their shape changed from circular to hexagonal and—importantly—after careful comparison of Figure 40a and b, we observe that no new etch pits were formed. A scheme of the etching processes can be seen in Figure 41. The fact that the etch

pits are hexagonal and that they all have the same orientation relative to one another means that carbon removal from either the zigzag or armchair type edges has a very different reaction rate [202]. A closer examination of the etch pits reveals evidence that indeed the carbothermal oxidation of graphene edges has taken place. AFM images of the etch pits reveal that, in depth, roughly 1 nm of the SiO₂ substrate was consumed, where the graphene has receded during the 700°C annealing step. This appears as a depression of the substrate beside the edges of the hexagonal holes (see Figure 40b and the line cut in Figure 42). This AFM based evidence shows us that carbothermal etching does indeed take place, but we cannot rule out the role of trace amounts of oxygen in this graphene etching process. Indeed, when studying the etching of CNTs on SiO₂, Byon et al. [208] have reported the necessity of having very small amounts of oxygen (a few parts per million) in the reaction chamber as a catalyst for carbothermal etching. The role of such minute amounts of oxygen in the reaction are the focus of further studies.

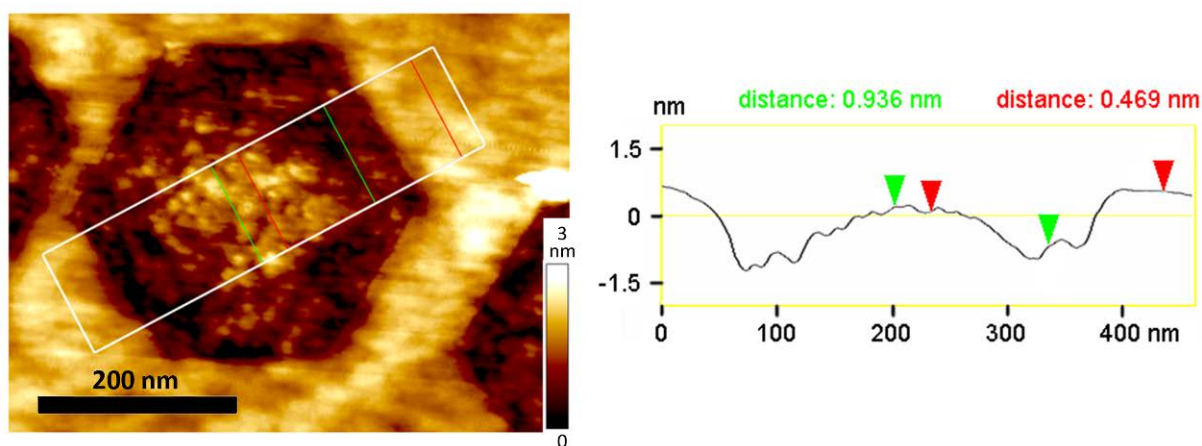


Figure 42. AFM image of a hexagonal etch pit from the sample shown in Figure 40. In the height profile we can clearly identify that the SiO₂ substrate has been etched away along with the graphene at the oxidation hole edges [T129].

The fact that the edges are so well formed shows that the above reaction has a high crystallographic selectivity under these annealing conditions, i.e., there is a much higher reaction rate for the removal of carbon from one type of graphene edge than from the other. Theoretical studies of armchair and zigzag edges have shown that they do indeed have different reactivity [198, 199], and different chemical processes favor etching of different edge orientations [134, 202].

3.3.2. Controlled patterning of graphene

One important characteristic of carbothermal graphene etching is that the carbon removal only occurs at the sample edges, or defect sites and in the places defined by the circular oxidation pits. This is a random network of defects, which gives little control over the resulting hexagonal hole distribution and architecture. A major advantage of the carbothermal etching process is that the distribution of the hexagonal holes is directly linked to the sample defect distribution, so by tailoring the defect positions one should be able to control the arrangement of the pattern composed of hexagonal holes.

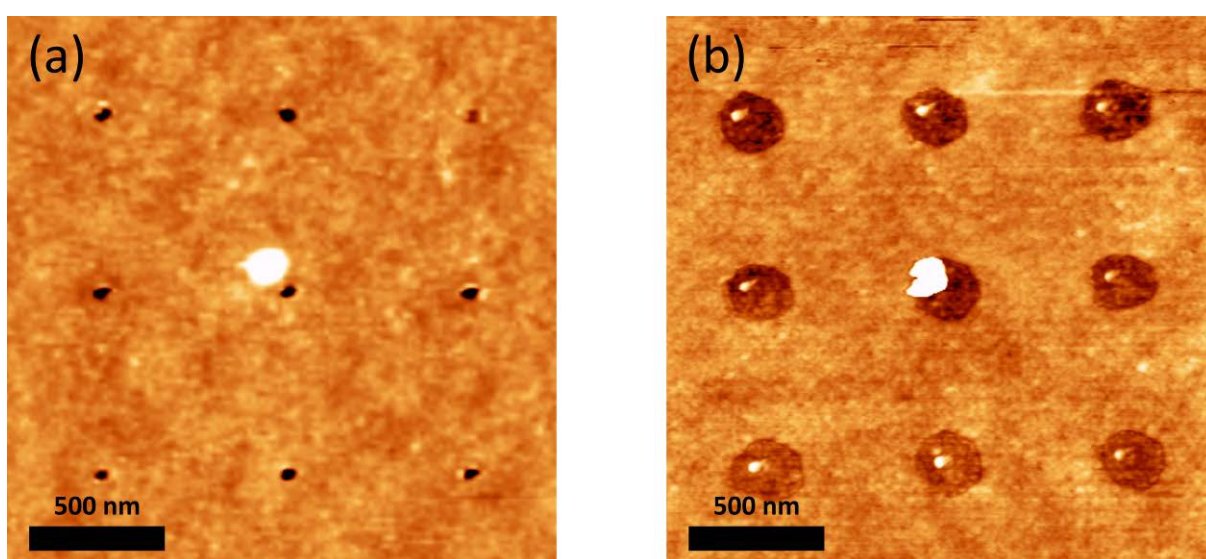


Figure 43. (a) The result of AFM indentation of a 3×3 matrix of holes in graphene. (b) AFM micrograph of the etch holes grown from the defects induced by indentation. Protrusions inside the hexagons are remnants of the AFM indentation process [T129].

The pre-patterning of defect sites may be achieved in many ways, through e-beam- or photolithography for example. Patterning was demonstrated by a very simple technique, that of using the tip of an AFM probe as an indentation tool [T129]. During AFM indentation one can puncture the graphene flake at predefined positions and thus create an ordered array of defects. The benefit of using AFM is its precision in the X–Y direction and the ability to quickly pattern periodic structures onto the graphene. An example of this can be seen in Figure 43a, where we have prepared a 3×3 matrix of indentation holes. By subsequent annealing, hexagonal pits can be grown by carbothermal etching starting from the puncture holes introduced by the AFM tip (Figure 43b).

Having demonstrated control over the position of the etch pits, controlling their size becomes the next issue at hand. Luckily, the size of these hexagonal pits can be adjusted by changing the annealing time. This is nicely illustrated in Figure 44, where three etch pits can be seen, after successive two hour carbothermal etch cycles. Starting out with etch pits of 300 nm size, the pits can be grown in size by 50 nm after each two hour etching cycle. This gives a growth rate of about 12 nm/h, allowing for a good control of pit dimensions.

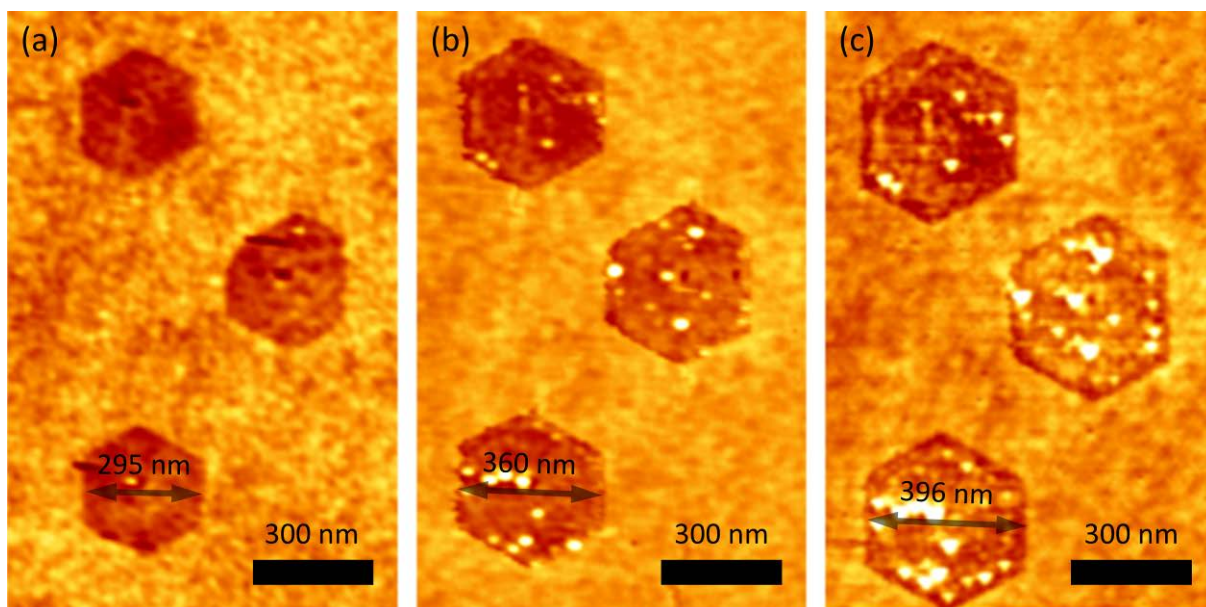


Figure 44. AFM images showing the controllability of carbothermal etching. (a) Three hexagons produced by AFM indentation and subsequent etching, of about 300 nm size. Images (b) and (c) show the same etch pits after an additional 2 and 4 h of etching, respectively. Small holes in the centers of the hexagons are the remnants of AFM indentation [T129].

3.3.3. Revealing the orientation of the etch pits

After showing that crystallographic orientation control and controllable positioning of the etch pits can be achieved, an important question still remains: what exact crystallographic orientation do the edges of these structures have? Some kind of information is needed on the atomic lattice directions in the sample, to reveal which of the two most stable edge orientations is etched in a preferential manner. This has been achieved by STM measurements on a graphene flake having pre-patterned hexagonal holes by carbothermal etching. To enable STM measurements, an electrical contact needs to be established with the graphene flake. This has been achieved by placing a metallic contact on the sample, in the form of an indium spike [209]. An atomic resolution STM image of the sample can be

seen in Figure 45b. The lattice directions deduced from the STM images have been matched to the AFM images of the etch pits. Thus, it was possible to show that the edge orientation of these pits is of zigzag type (Figure 45) [T129]. Matching the STM and AFM images was accomplished by using certain sample features as markers, for example the thicker graphene edge of the sample seen in Figure 45a. It needs to be emphasized at this point that the STM measurements were not obtained exactly at the hexagonal pit edges, but rather a few hundred nanometers further away, making possible the identification of the crystallographic axes of the sample and therefore the edge orientation, but without any information about the atomic structure of the edge itself. Measuring exactly at the edge of the hexagonal holes with STM is rather difficult, because of the transition from the graphene to the insulating SiO_2 damages the STM tip and severely hinders imaging.

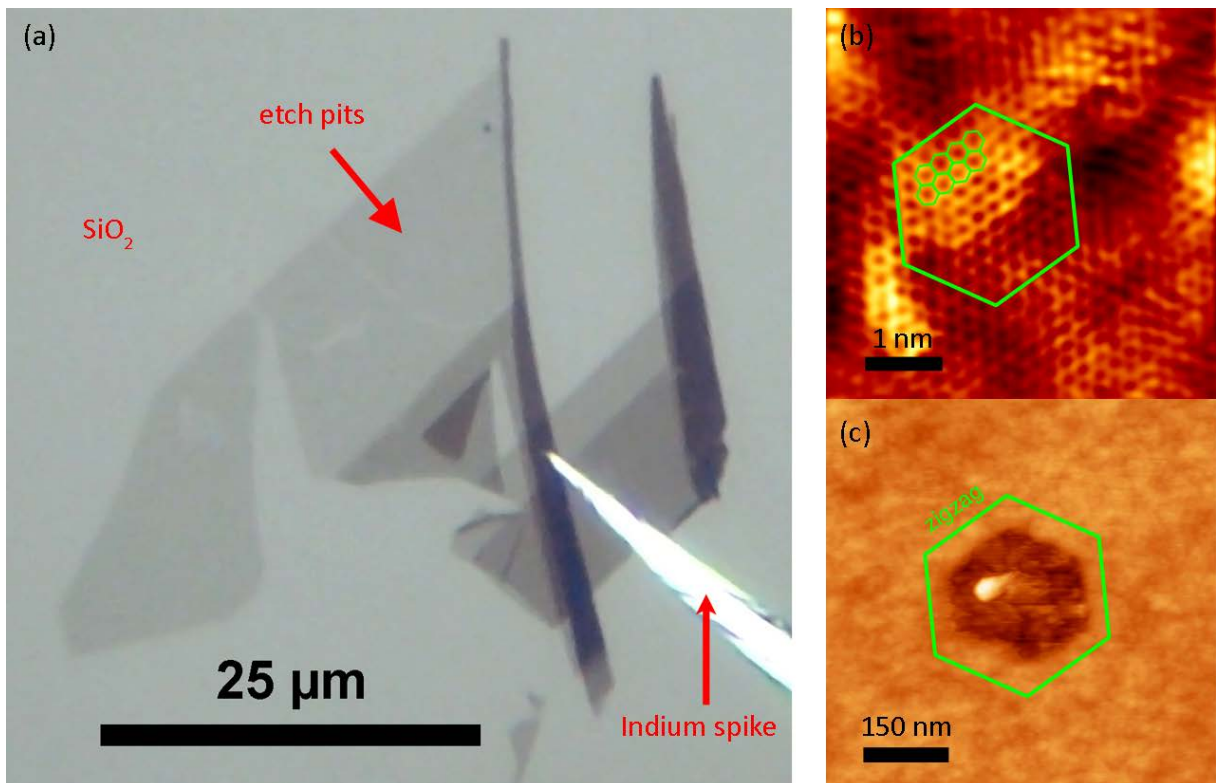


Figure 45. (a) Optical micrograph of the patterned graphene sample contacted by an indium spike for STM measurements. (b) STM image and (c) AFM image side by side, showing the atomic lattice of the graphene sample and the orientation of the etch pit. The hexagons help to visualize the orientation relationship between the two images [T129].

3.3.4. Crystallinity and edge roughness

Having demonstrated precise patterning of the etch pits and size controllability of these nanostructures we need to address another crucial issue. Oxidative chemical processing can damage the basal plane of graphene. Albeit the solid – solid reaction described here is much milder than other solution based techniques [170] it needs to be clarified if the etching only takes place at the sample edges, as suggested by AFM measurements, or if the basal plane of graphene gets damaged as well. An estimate of the defect concentration and the edge roughness of the hexagonal etch pits are very important factors, since the physical properties of crystallographically oriented graphene nanostructures is strongly influenced by this kind of disorder (see chapter 1.4.2).

Defect sites induce scattering between two non equivalent K valleys in graphene, which leads to $\sqrt{3}x\sqrt{3}R30^\circ$ type superstructures [210], also observed on CNTs with defect sites (Figure 27). A good indication that no additional defects were created during the carbothermal etching process is that atomic resolution STM measurements (Figure 45b) show no sign of the $\sqrt{3}x\sqrt{3}R30^\circ$ type superstructure, thus intervalley scattering is absent. However, STM can only give local information about the defect structure of the sample. This is why Raman spectroscopy was used to estimate the crystallinity of the graphene layers before and after carbothermal etching. Similarly to the case of carbon nanotubes (Figure 25b), the intensity ratio of the D peak and G peak in the Raman spectra of graphene is proportional to the defect concentration [162, 163]. In Figure 46 Raman spectra of the pristine graphene sample, and etched samples are shown. On the sample oxidized in air and the one subjected to carbothermal etching, the laser spot was kept clear of the sample edges and etch holes as much as possible in order to record spectra from only the graphene basal plane. We can observe the absence of the D peak of graphene at around 1350 cm^{-1} for both the pristine and etched samples. This finding strengthens the conclusions drawn by AFM and STM measurements, that although the graphene layer gets etched out at the edges, it retains its nearly perfect crystal structure. This means that during carbothermal etching, the dissociation of carbon bonds only occurs at the sample edges where the carbon

atoms have less than three neighbors and the binding energy of the atoms is therefore lower than for lattice positions having three nearest neighbors.

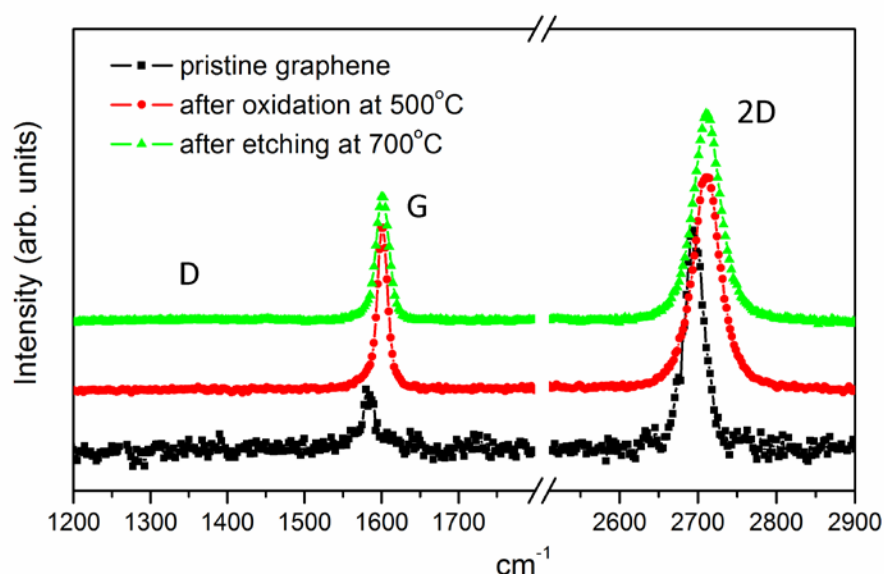


Figure 46. Raman spectra of the pristine sample, oxidized sample and the sample after carbothermal etching. Positions of the D, G and 2D peaks is shown. The spectra are displaced vertically for easier comparison [T129].

Further examination of the Raman spectra gives us more insight into the changes that have been induced during carbothermal etching. By following the evolution of the Raman spectra acquired for the pristine sample, the oxidized sample at 500°C and the sample annealed at 700 °C we can observe a significant upshift of the frequency of the G and 2D peaks, normally found at 1580 cm⁻¹ and 2700 cm⁻¹, respectively (Figure 46). This shift of the Raman peaks has also been observed by Liu et al [203]. Such changes in the Raman frequencies are most likely due to a convolution of two effects. According to the work of Das et al. this upshift of about 20 cm⁻¹ can be attributed to a strong hole doping of the graphene layer [211]. From the electrochemical top-gate doping experiments of Das et al. we can estimate the Fermi level shift to be around 0.48 eV with a hole density of $1.5 \times 10^{13} \text{ cm}^{-2}$. Graphene samples prepared under ambient conditions usually show p-type doping [212]. In our case the p doping originates from the adsorption of oxygen and water at the highly reactive graphene edges and basal plane during annealing [213]. Nevertheless, the very large doping level deduced this way is not usually seen in experiments and is very hard to obtain [211]. Therefore, another contribution to the observed G and 2D shifts needs to be considered. It has been shown that due to the very different thermal expansion coefficients of graphene

and its substrate, compressive stress can build up in supported graphene layers [213, 214, 215], giving rise to an upshift in the G and 2D frequencies.

Finally, another important issue to explore is the roughness of the etch pit edges. STM measurements have not determined the exact structure of the edge carbon chains, but only the crystallographic direction of the edges. Since disorder at the edges of graphene nanostructures can strongly perturb the specific physical properties of the zigzag (or armchair) edge [116, 117, 121] it is important to try to characterize the disorder at the edges of the hexagonal pits. Here, disorder is defined as the percentage of pure zigzag edges to other edge structures.

Once more we turn to the analysis of the D peak in graphene, and this time we're interested in the scattering processes that occur at the graphene edges. Cançado et al. have suggested that the D peak should vanish for atomically perfect zigzag edges, while it should be present in armchair graphene edges [216]. The scheme of the scattering mechanism which results in the graphene D peak can be seen in Figure 47.

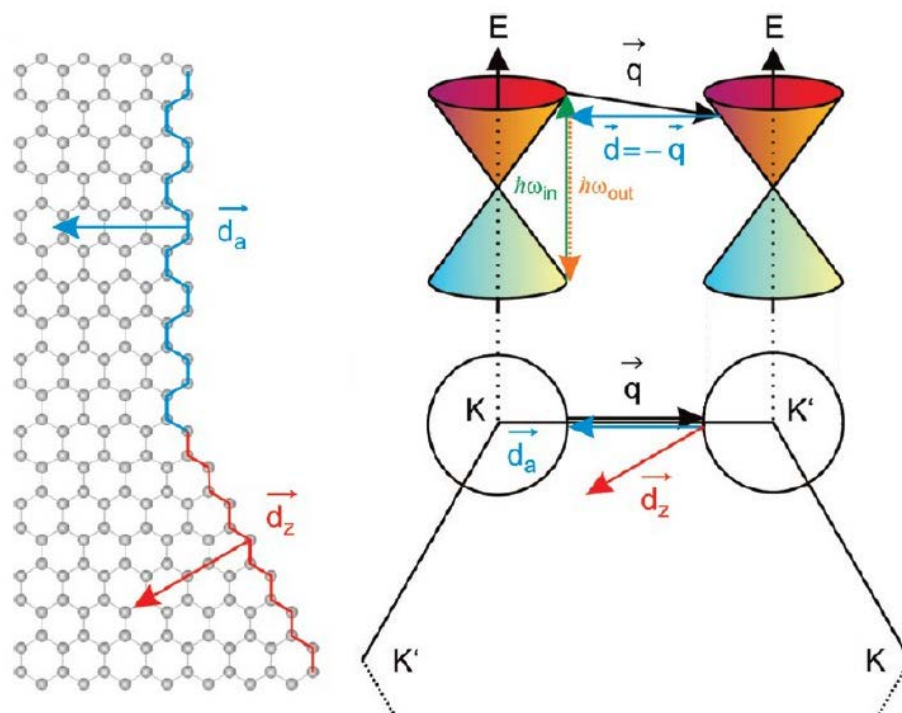


Figure 47. Scheme of the scattering process in reciprocal space, which leads to the D peak in the Raman spectra of graphene and at the zigzag and armchair edges. Figure adapted from ref. 145

An electron hole pair is created by an incident photon of the laser source, with the energy of $\hbar\omega_{in}$. This electron (or hole) gets scattered in an inelastic manner by a phonon of momentum \vec{q} from one K valley to another non equivalent K' valley at the Brillouin zone boundary. The electron (or hole) gets backscattered elastically to the original K valley by scattering on a defect, say in this case the graphene edge, and recombines to emit a photon of energy $\hbar\omega_{out}$. This double scattering process only occurs if the backscattering is such that the momentum gets conserved, thus with a momentum $-\vec{q}$. The momentum gets conserved along the crystallographic direction and backscattering can only occur in a perpendicular direction relative to the edge. On the zigzag edge backscattering cannot proceed in the proper direction, therefore a perfect zigzag edge does not contribute to the D peak formation, whereas the momentum transfer in the armchair case makes the appearance of the D peak possible (Figure 47) [216].

Various research groups have attempted to measure this proposed disappearance of the D peak for zigzag edges, with mixed success [127, 217]. These authors have measured the D peak of exfoliated graphene flakes having edge corners with relative angles of odd multiples of 30 degrees. In an ideal case such a configuration should contain edges with a zigzag and an armchair direction (see Figure 5). In these studies the intensity of the D peaks for these two edge types was very similar and their ratio was less than a factor of 2 [127, 217]. This has been attributed to the large edge roughness of graphene flakes prepared by micromechanical cleaving [217].

In order to investigate the suppression of the D peak in the hexagonal etch pits obtained by carbothermal etching, the Raman spectra of hexagonal etch pits prepared by carbothermal etching was measured in a collaboration, by Krauss et al. [145]. Raman spectra of individual etch pits were obtained with a laser spot size of ~ 400 nm, which could be positioned on the surface with high precision. The Raman spectra of individual hexagonal etch holes shows a highly diminished D peak, which is virtually equal in intensity to the D peak of the sample bulk (Figure 48f-g). We can compare this result to spectra measured on circular etch pits produced by oxidation in air (Figure 48a). Contrary to hexagonal etch holes, circular pits should have a mixture of zigzag and armchair edge sections, see sketch in Figure 48d. Therefore, circular pits should have a significant D peak intensity relative to the graphene

bulk and our measurements reflect this perfectly, exhibiting a sizeable D peak (Figure 48b-c). Comparing the D to G peak intensity ratios measured on circular etch pits and hexagonal zigzag edged pits, we observe a difference of one order of magnitude. This shows that the zigzag edges prepared by carbothermal etching have the least edge disorder obtained to date [145], making this study the first to clearly demonstrate experimentally the predicted inelastic light scattering behavior a pure graphene zigzag edges.

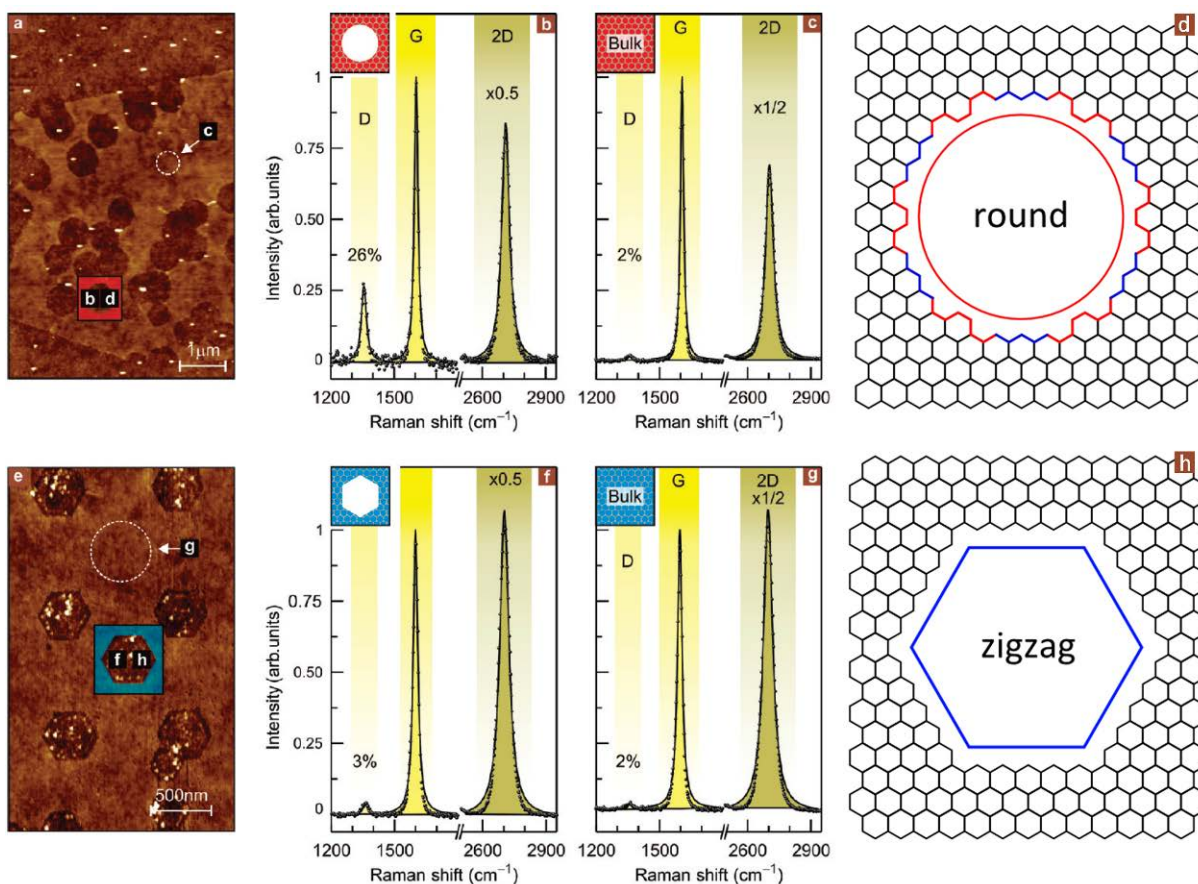


Figure 48. Scheme of circular and zigzag edged holes in graphene. Raman spectra of a graphene sample having round holes (upper panel) and hexagonal holes (lower panel). AFM images of the positions where the Raman spectra on the right-hand side were obtained (a, e). The Raman spectrum of a round hole has a strong D peak (b), whereas the D peak for a hexagonal hole (f) is minimal and only slightly higher than the surrounding bulk value (c and g). Figure reproduced from ref. 145.

I have shown that with the use of carbothermal etching, graphene samples with well defined zigzag edges can be prepared. This is among the first studies which shows that samples can be prepared in which disorder does not disrupt the edge specific physics to a degree that renders it unobservable. This raises the hope that, among other things, the charge transport properties of zigzag edged graphene nanostructures, such as GNRs, can be observed in the

laboratory, bringing this field of research into the realm of experimental investigation. Figure 49 shows a GNR prepared by growing two etch pits close together. At the time of publishing [T129] this was the first example of a graphene nanoribbon with well-defined zigzag orientation of the edges, being produced on an insulating substrate, using a well controlled patterning process. In addition, more complex architectures, such as nanoribbon “Y” junctions may also be obtained without much difficulty.

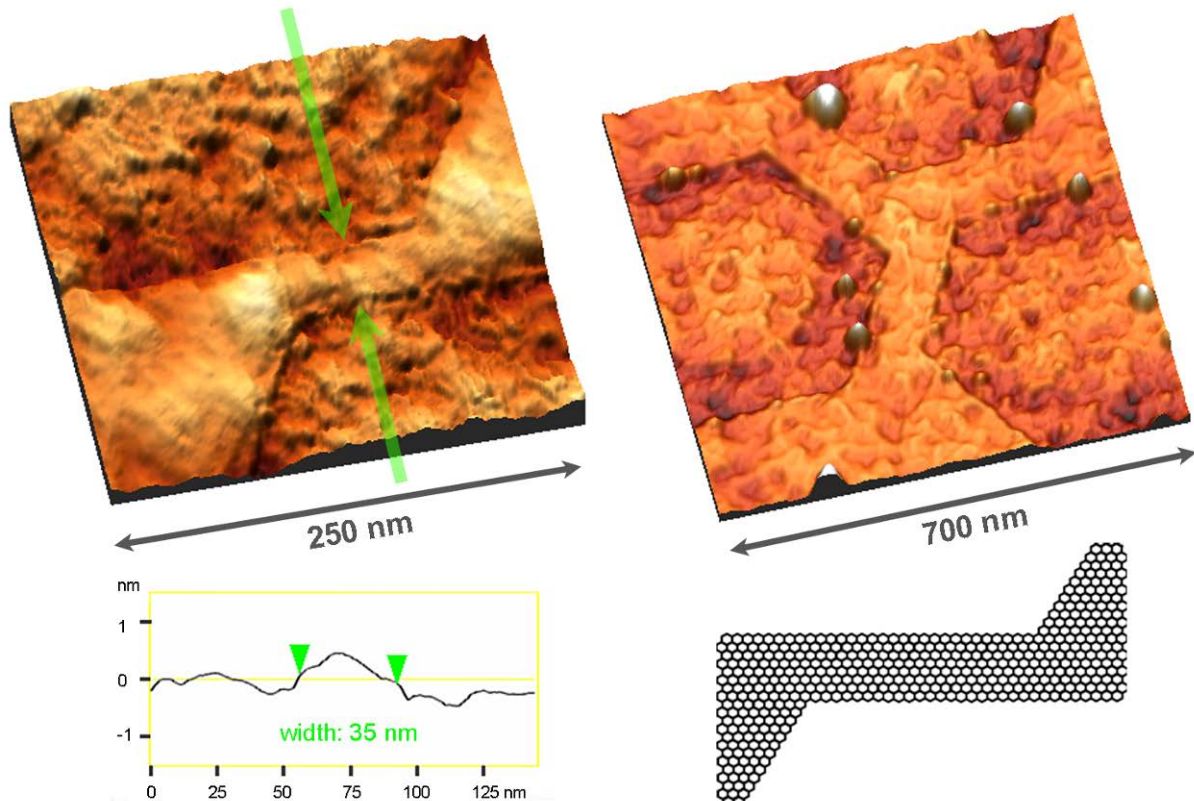


Figure 49. The left image shows a three-dimensional (3-D) AFM image of a graphene nanoribbon of about 35 nm width. The AFM height profile has been acquired between the places marked by green arrows. The inset in the right lower corner shows a scheme of the corresponding atomic structure. The right image shows a “Y” junction of three nanoribbons, with the ribbons having widths of 93, 100, and 101 nm (starting from the upper left ribbon, going clockwise) [T129].

4. Summary

In this thesis I have explored the preparation of graphene nanostructures, having crystallographically well defined edges and the scanning probe measurements of graphene and functionalized carbon nanotubes. The results of my research can be summarized in three main parts.

I have developed a sample preparation technique, based on a carbon nanotube – few layer graphite composite that provides a simple and effective solution to sample stability issues encountered when measuring functionalized carbon nanotubes with STM. Such a composite has enabled for the first time to measure functionalized carbon nanotubes in atomic resolution, as well as to acquire energy resolved STM images of the tubes. Functionalized and pristine regions of the nanotube surface were made visible and the positions of the functional groups could be correlated with crystal lattice directions. The ease of the sample preparation allows the use of my method to study the properties of other types of functionalized carbon nanotubes. This adds STM to the toolbox of functionalized carbon nanotube characterization techniques, complementing optical spectroscopic methods.

I have investigated the source of anomalous thickness measurements of graphene and few layer graphite, obtained by tapping mode AFM. The physical origin of these artefacts was elucidated by measurements and theoretical modeling of the AFM tip oscillation and tip – sample interaction. Numerical calculations and experiments have been used to show the correct experimental parameters needed to image the true thickness of graphene layers on a supporting substrate. The conclusions are general enough so that they can be applied to the measurements of other nanosized objects by AFM.

I have demonstrated the existence of a chemical etching procedure that discriminates between the armchair and zigzag type edge termination of graphene layers. Coupled with AFM patterning, I have used this chemical process to pattern graphene sheets into nanostructures having zigzag edges. Raman measurements show that the edge roughness of these nanostructures is low enough that inelastic light scattering processes specific to the zigzag edge could be measured. This is the first study which shows that zigzag edged

graphene nanostructures can be prepared in the laboratory in a controlled manner, which have a low enough edge disorder to enable the experimental observation of zigzag edge specific physical processes.

5. Thesis points

1. I have developed a simple procedure that improves the sample stability during measurement of functionalized carbon nanotubes by STM and have performed energy resolved STM mapping on the nanotubes.
 - a. I have demonstrated that incorporating the functionalized carbon nanotubes into a nanotube – few layer graphite composite significantly reduced the, STM tip induced movement, of the nanotubes on the surface. I have shown that the sample is stable for the long periods of time needed to acquire repeated CITS measurements.
 - b. I was able to achieve nanometer resolution conductivity maps of the functionalized nanotube surface. I have shown that the functionalized regions on the nanotubes correspond to low conductivity regions.
 - c. I have shown that functionalization on the nanotubes can occur in bands of functional groups. A correlation between the layout of the functionalized bands and the zigzag direction on the nanotube surface has been shown to exist, with the functionalized bands extending along the zigzag direction.
 - d. Through CITS measurements, I have demonstrated the possibility of mapping the local shift in the Fermi level on the nanotube surface.
2. I have explored the source of anomalous thickness values reported in the literature for tapping mode AFM measurements of graphene layers supported on a SiO₂ substrate.
 - a. I have shown that the origin of this measurement artefact is a discontinuity in the amplitude response of the vibrating AFM tip at certain setpoint and free amplitude values of the vibrating tip.

- b. I have demonstrated that measuring the thickness of graphene and few layer graphite in the net attractive tip – sample interaction regime produces unreliable thickness values.
 - c. Through numerical modeling of the tip oscillation, I have shown that water adsorbed on the supporting SiO₂ surface has significant effects on imaging in the net attractive tip – sample interaction regime.
 - d. Through AFM and Raman spectroscopic validation I have demonstrated that if the height measurement of graphene is made in the net repulsive tip – sample interaction regime, the thickness of graphene is reproducible and corresponds to the true thickness of the nanostructure.
3. I have shown that the preparation of graphene nanostructures with crystallographically well oriented edges is possible with the carbothermal etching of graphene layers on a SiO₂ substrate.
- a. Using STM measurements I have shown that the hexagonal etch pits prepared by carbothermal etching have a zigzag orientation.
 - b. Using Raman spectroscopy and STM measurements I have demonstrated that the carbothermal etching at 700°C etches only the edges of the graphene layers, leaving the graphene basal plane unaffected.
 - c. Through pre-patterning of defect sites with an AFM tip into the graphene layer, I have demonstrated that the positions of the etch pits can be controlled.
 - d. I have shown that graphene nanoribbons with zigzag edges can be prepared by the carbothermal etching of graphene.

6. List of publications

6.1. Publications used to compose the thesis points

- [1] P. Nemes-Incze, Z. Kónya, I. Kiricsi, A. Pekker, Z.E. Horváth, K. Kamarás, et al., Mapping of Functionalized Regions on Carbon Nanotubes by Scanning Tunneling Microscopy, **J. Phys. Chem. C.** 115 (2011) 3229–3235. Impakt factor: 4.224; citations: 1
- [2] P. Nemes-Incze, G. Magda, K. Kamarás, L.P. Biró, Crystallographically Selective Nanopatterning of Graphene on SiO₂, **Nano Res.** 3 (2010) 110-116. Impakt factor: 4.37; citations: 16
- [3] P. Nemes-Incze, Z. Osváth, K. Kamarás, L.P. Biró, Anomalies in thickness measurements of graphene and few layer graphite crystals by tapping mode atomic force microscopy, **Carbon.** 46 (2008) 1435-1442. Impakt factor: 4.504; citations: 63

6.2. Other publications

- [1] L.P. Biro, P. Nemes-Incze, P. Lambin, Graphene: nanoscale processing and recent applications, *Nanoscale.* 4 (2012) 1824-39
- [2] L. Tapasztó, P. Nemes-Incze, G. Dobrik, K. Jae Yoo, C. Hwang, L.P. Biró, Mapping the electronic properties of individual graphene grain boundaries, *Appl. Phys. Lett.* 100 (2012) 053114.
- [3] L.P. Biró, P. Nemes-Incze, G. Dobrik, C. Hwang, L. Tapasztó, Graphene nanopatterns with crystallographic orientation control for nanoelectronic applications, *Diamond and Related Materials.* 20 (2011) 1212-1217.
- [4] I. Tamáska, G. Dobrik, P. Nemes-Incze, K. Kertész, E. Horváth, G.I. Márk, et al., Bioinspired photonic nanoarchitectures from graphitic thin films, *Thin Solid Films.* 519 (2011) 4078-81.

- [5] P. Nemes-Incze, K.J. Yoo, L. Tapasztó, G. Dobrik, J. Lábár, Z.E. Horváth, et al., Revealing the grain structure of graphene grown by chemical vapor deposition, *Appl. Phys. Lett.* 99 (2011) 023104.
- [6] P. Nemes-Incze, G. Magda, K. Kamarás, L.P. Biró, Crystallographic orientation dependent etching of graphene layers, *Physica Status Solidi (c)*. 7 (2010) 1241-1245.
- [7] G. Dobrik, P. Nemes-Incze, L. Tapasztó, P. Lambin, L.P. Biró, Nanoscale lithography of graphene with crystallographic orientation control, *Physica E.* (2010).
- [8] P.L. Neumann, Z.E. Horváth, P. Nemes-Incze, G. Molnár, G. Vértesy, L.P. Biró, Electrical behavior of indium contacted graphene flakes, *Nanopages*. 5 (2010) 1-8.
- [9] G. Dobrik, L. Tapasztó, P. Nemes-Incze, P. Lambin, L.P. Biró, Crystallographically oriented high resolution lithography of graphene nanoribbons by STM lithography, *Phys. Status Solidi B*. 247 (2010) 896 - 902.
- [10] B. Krauss, P. Nemes-Incze, V. Skakalova, L.P. Biró, K.V. Klitzing, J.H. Smet, Raman Scattering at Pure Graphene Zigzag Edges., *Nano Lett.* 10 (2010) 4544-4548.
- [11] P. Nemes-Incze, L. Tapasztó, A. Darabont, P. Lambin, L.P. Biró, Scanning tunneling microscopy observation of circular electronic superstructures on multiwalled carbon nanotubes functionalised by nitric acid, *Carbon*. 47 (2009) 764-768.
- [12] Z. Osváth, P. Nemes-Incze, L. Tapasztó, Z.E. Horváth, L.P. Biró, Thermal oxidation of few-layer graphite plates: an SPM study, *Physica Status Solidi (a)*. 205 (2008) 1419-1423.
- [13] L. Tapasztó, P. Nemes-Incze, Z. Osváth, M. Bein, A. Darabont, L.P. Biró, Complex superstructure patterns near defect sites of carbon nanotubes and graphite, *Physica E*. 40 (2008) 2263-2267.
- [14] Z. Sárközi, K. Kertész, A.A. Koós, Z. Osváth, L. Tapasztó, Z.E. Horváth, et al., Synthesis of carbon nanotubes from liquid hydrocarbons using a spray-pyrolysis method, *J. Optoelectron. Adv. M.* 10 (2008) 2307 - 2310.

- [15] L. Tapasztó, G. Dobrik, P. Nemes-Incze, G. Vertesy, P. Lambin, L.P. Biró, Tuning the electronic structure of graphene by ion irradiation, *Phys. Rev. B.* 78 (2008) 233407.
- [16] Z. Osváth, A. Darabont, P. Nemes-Incze, Z.E. Horváth, L.P. Biró, Graphene layers from thermal oxidation of exfoliated graphite plates, *Carbon.* 45 (2007) 3022-3026.
- [17] O. Tipriğan, A.A. Koós, P. Nemes-Incze, Z.E. Horváth, Z. Sárközi, S. Simon, et al., Obtaining bamboo-structured, multiwalled carbon nanotubes using the spray pyrolysis method, *J. Optoelectron. Adv. M.* 9 (2007) 617 - 620.
- [18] P. Nemes-Incze, N.S. Daróczy, Z. Sárközi, A.A. Koós, K. Kertész, O. Tipriğan, et al., Synthesis of bamboo-structured multiwalled carbon nanotubes by spray pyrolysis method, using a mixture of benzene and pyridine, *J. Optoelectron. Adv. M.* 9 (2007) 1525 - 1529.
- [19] Z. Szekrényes, P. Nemes-Incze, A. Darabont, N.S. Daróczy, A.A. Koós, Z.E. Horváth, et al., Synthesis and Raman characterization of single-walled carbon nanotubes growth by injection chemical vapour deposition, *J. Optoelectron. Adv. M.* 9 (2007) 605 - 609.
- [20] Z.E. Horváth, K. Kertész, L. Pethő, A.A. Koós, L. Tapasztó, Z. Vértesy, et al., Inexpensive, upscalable nanotube growth methods, *Current Applied Physics.* 6 (2006) 135-140.
- [21] L. Tapasztó, P. Nemes-Incze, Z. Osváth, A. Darabont, P. Lambin, L.P. Biró, Electron scattering in a multiwall carbon nanotube bend junction studied by scanning tunneling microscopy, *Phys. Rev. B.* 74 (2006) 235422.
- [22] A. Darabont, P. Nemes-Incze, K. Kertész, L. Tapasztó, A.A. Koós, Z. Osváth, et al., Synthesis of carbon nanotubes by spray pyrolysis and their investigation by electron microscopy, *J. Optoelectron. Adv. M.* 7 (2005) 631 - 636.

7. Acknowledgements

The help and support of my advisor Prof. Dr. Biró László Péter is greatly appreciated, his wisdom and the infrastructural background he provided, through the Nanostructures lab at MFA, made this thesis possible. I am also thankful to all of my colleagues the Nanostructures laboratory of MFA for helpful advice and guidance. I am thankful to Dr. Kamarás Katalin, who was always helpful regarding Raman measurements, for Dr. Veres Miklós for allowing access to the Raman facility of the MTA – SZFKI and for Dr. Vértesy Zofia for SEM measurements of AFM tips. I am also grateful for the work and collaboration of scientists of the Max-Planck-Institute for Solid State Research, especially Benjamin Krauss who measured the Raman spectra of individual graphene etch holes.

I would also thank the director of the MFA, Prof. Dr. Bársony István and to the past director of the MFA, Prof. Dr. Gyulai József, members of the Hungarian Academy of Sciences, for their support and for providing the necessary background to my research.

I am very grateful to the support and encouragement of my former advisor, Prof. Dr. Darabont Sándor, who started off my career in carbon nanostructure research and who helped me become the person I am today.

References

¹ M.E. Davis, J.E. Zuckerman, C.H.J. Choi, D. Seligson, A. Tolcher, C. a Alabi, et al., Evidence of RNAi in humans from systemically administered siRNA via targeted nanoparticles., *Nature*. 464 (2010) 1067-70.

² L. Kalaugher, Nanotube bike enters Tour de France, *Nanotechweb.org*. (2005)
<http://nanotechweb.org/cws/article/tech/22597>

³ A. Eitan, K. Jiang, D. Dukes, R. Andrews, L.S. Schadler, Surface Modification of Multiwalled Carbon Nanotubes: Toward the Tailoring of the Interface in Polymer Composites, *Chem. Mater.* 15 (2003) 3198-3201.

⁴ C. Lok, Nanotechnology: Small wonders., *Nature*. 467 (2010) 18-21.

⁵ K.S. Novoselov, A.K. Geim, S.V. Morozov, D. Jiang, Y. Zhang, S.V. Dubonos, et al., Electric field effect in atomically thin carbon films, *Science*. 306 (2004) 666-9.

⁶ P.R. Wallace, The band theory of graphite, *Phys. Rev.* 71 (1947) 622-634.

-
- ⁷ X. Du, I. Skachko, A. Barker, E.Y. Andrei, Approaching ballistic transport in suspended graphene., *Nat. Nanotechnol.* 3 (2008) 491-5.
- ⁸ M.S. Fuhrer, C.N. Lau, A.H. Macdonald, Graphene: Materially Better Carbon, *MRS Bulletin.* 35 (2010).
- ⁹ T. Dürkop, S. a Getty, E. Cobas, M.S. Fuhrer, Extraordinary Mobility in Semiconducting Carbon Nanotubes, *Nano Lett.* 4 (2004) 35-39.
- ¹⁰ B. Peng, M. Locascio, P. Zapol, S. Li, S.L. Mielke, G.C. Schatz, et al., Measurements of near-ultimate strength for multiwalled carbon nanotubes and irradiation-induced crosslinking improvements., *Nat. Nanotechnol.* 3 (2008) 626-31.
- ¹¹ I.W. Frank, D.M. Tanenbaum, A.M. van Der Zande, P.L. McEuen, Mechanical properties of suspended graphene sheets, *Journal Of Vacuum Science & Technology B: Microelectronics and Nanometer Structures.* 25 (2007) 2558.
- ¹² A.K. Geim, K.S. Novoselov, The rise of graphene, *Nat. Mater.* 6 (2007) 183-191.
- ¹³ H.W. Kroto, J.R. Heath, S.C. O'Brien, R.F. Curl, R.E. Smalley, C60: Buckminsterfullerene, *Nature.* 318 (1985) 162-163.
- ¹⁴ S. Iijima, Helical microtubules of graphitic carbon, *Nature.* 354 (1991) 56-58.
- ¹⁵ K.S. Novoselov, D. Jiang, F. Schedin, T.J. Booth, V.V. Khotkevich, S.V. Morozov, et al., Two-dimensional atomic crystals., *Pnas.* 102 (2005) 10451-3.
- ¹⁶ W.J. Cantwell, J. Morton, The impact resistance of composite materials - a review, *Composites.* 22 (1991) 347-362.
- ¹⁷ J. Gorss, High Performance Carbon Fibers, URL:
http://portal.acs.org/portal/PublicWebSite/education/whatischemistry/landmarks/industrial/CTP_004458
- ¹⁸ J. Cami, J. Bernard-Salas, E. Peeters, S.E. Malek, Detection of C60 and C70 in a Young Planetary Nebula, *Science.* 329 (2010) 1180-1182.
- ¹⁹ T.W. Ebbesen, Carbon Nanotubes, *Annual Review Of Materials Science.* 24 (1994) 235-264.
- ²⁰ M. Monthioux, V.L. Kuznetsov, Who should be given the credit for the discovery of carbon nanotubes?, *Carbon.* 44 (2006) 1621.
- ²¹ B.Q. Wei, R. Vajtai, P.M. Ajayan, no title, *Appl. Phys. Lett.* 79 (2001) 1172-1174.
- ²² M. Terrones, SCIENCE AND TECHNOLOGY OF THE TWENTY-FIRST CENTURY: Synthesis, Properties, and Applications of Carbon Nanotubes, *Annual Review Of Materials Research.* 33 (2003) 419-501.
- ²³ K. Lau, D. Hui, The revolutionary creation of new advanced materials-carbon nanotube composites, *Composites: Part B.* 33 (2002) 263-277.
- ²⁴ M.C. Hersam, Progress towards monodisperse single-walled carbon nanotubes, *Nat. Nanotechnol.* 3 (2008) 387-394.
- ²⁵ T. Tanaka, H. Jin, Y. Miyata, S. Fujii, H. Suga, Y. Naitoh, et al., Simple and scalable gel-based separation of metallic and semiconducting carbon nanotubes., *Nano Lett.* 9 (2009) 1497-500.

-
- ²⁶ L.P. Biró, P. Lambin, Nanopatterning of graphene with crystallographic orientation control, *Carbon*. 48 (2010) 2677-2689.
- ²⁷ A.H. Castro Neto, S.Y. Zhou, G.-H. Gweon, A.V. Fedorov, P.N. First, W.A. de Heer, et al., Substrate-induced bandgap opening in epitaxial graphene., *Nat. Mater.* 6 (2007) 770-5.
- ²⁸ A.H. Castro Neto, V.M. Pereira, Strain Engineering of Graphene's Electronic Structure, *Phys. Rev. Lett.* 103 (2009) 046801.
- ²⁹ J.M. Blakely, J.S. Kim, H.C. Potter, Segregation of Carbon to the (100) Surface of Nickel, *J. Appl. Phys.* 41 (1970) 2693-2697.
- ³⁰ M. Eizenberg, J.M. Blakely, Carbon interaction with nickel surfaces: Monolayer formation and structural stability, *J. Chem. Phys.* 71 (1979) 3467.
- ³¹ J.C. Hamilton, J.M. Blakely, Carbon layer formation on the Pt (111) surface as a function of temperature, *J. Vac. Sci. Tech.* 15 (1978) 559-562.
- ³² W.S.J. Hummers, R.E. Offeman, Preparation of Graphitic Oxide, *J. Am. Chem. Soc.* 80 (1958) 80 (6), p 1339.
- ³³ D.R. Dreyer, R.S. Ruoff, C.W. Bielawski, From Conception to Realization: An Historical Account of Graphene and Some Perspectives for Its Future, *Angewandte Chemie International Edition*. 71 (2010) 9336-9344.
- ³⁴ H.P. Boehm, R. Setton, E. Stumpp, Nomenclature and terminology of graphite intercalation compounds, *Carbon*. 24 (1986) 241-245.
- ³⁵ N.D. Mermin, Crystalline order in two dimensions, *Phys. Rev.* 176 (1968) 250-254.
- ³⁶ K.S. Novoselov, A.K. Geim, S.V. Morozov, D. Jiang, M.I. Katsnelson, I.V. Grigorieva, et al., Two-dimensional gas of massless Dirac fermions in graphene, *Nature*. 438 (2005) 197-200.
- ³⁷ K.S. Novoselov, Z. Jiang, Y. Zhang, S.V. Morozov, H.L. Stormer, U. Zeitler, et al., Room-temperature quantum Hall effect in graphene., *Science*. 315 (2007) 1379.
- ³⁸ Y. Zhang, Y.-W. Tan, H.L. Stormer, P. Kim, Experimental observation of the quantum Hall effect and Berry's phase in graphene., *Nature*. 438 (2005) 201-4.
- ³⁹ C. Berger, Z. Song, T. Li, X. Li, A.Y. Ogbazghi, R. Feng, et al., Ultrathin Epitaxial Graphite: 2D Electron Gas Properties and a Route toward Graphene-based Nanoelectronics, *J. Phys. Chem. B*. 108 (2004) 19912-19916.
- ⁴⁰ T.J. Booth, J.C. Meyer, A.K. Geim, M.I. Katsnelson, K.S. Novoselov, S. Roth, The structure of suspended graphene sheets, *Nature*. 446 (2007) 60-63.
- ⁴¹ W. Cullen, M. Yamamoto, K. Burson, J. Chen, C. Jang, L. Li, et al., High-Fidelity Conformation of Graphene to SiO₂ Topographic Features, *Phys. Rev. Lett.* 105 (2010) 215504.
- ⁴² L. Brey, J.J. Palacios, Exchange-induced charge inhomogeneities in rippled neutral graphene, *Phys. Rev. B*. 77 (2008) 041403(R).
- ⁴³ L. Covaci, M. Berciu, Survival of the Dirac Points in Rippled Graphene, *Phys. Rev. Lett.* 100 (2008) 256405.
- ⁴⁴ A. Castro Neto, F. Guinea, N. Peres, K.S. Novoselov, A. Geim, The electronic properties of graphene, *Rev. Mod. Phys.* 81 (2009) 109-162.

-
- ⁴⁵ S. Reich, J. Maultzsch, C. Thomsen, P. Ordejón, Tight-binding description of graphene, *Phys. Rev. B.* 66 (2002) 035412.
- ⁴⁶ C.W.J. Beenakker, Colloquium: Andreev reflection and Klein tunneling in graphene, *Rev. Mod. Phys.* 80 (2008) 1337-1354.
- ⁴⁷ P.M. Ostrovsky, I.V. Gornyi, A.D. Mirlin, Theory of anomalous quantum Hall effects in graphene, *Phys. Rev. B.* 77 (2008) 195430.
- ⁴⁸ A. Rycerz, J. Tworzydło, C.W.J. Beenakker, Valley filter and valley valve in graphene, *Nat. Phys.* 3 (2007) 172-175.
- ⁴⁹ D.P. DiVincenzo, E.J. Mele, Self-consistent effective-mass theory for intralayer screening in graphite intercalation compounds, *Physical Review B.* 29 (1984) 1685-1694.
- ⁵⁰ R.R. Nair, P. Blake, A.N. Grigorenko, K.S. Novoselov, T.J. Booth, T. Stauber, et al., Fine structure constant defines visual transparency of graphene, *Science.* 320 (2008) 1308.
- ⁵¹ M.S. Dresselhaus, G. Dresselhaus, R. Saito, Physics of carbon nanotubes, *Carbon.* 33 (1995) 883-891.
- ⁵² R. Saito, M. Fujita, G. Dresselhaus, M.S. Dresselhaus, Electronic structure of chiral graphene tubules, *Appl. Phys. Lett.* 60 (1992) 2204-2206.
- ⁵³ M.S. Dresselhaus, G. Dresselhaus, R. Saito, Physics of carbon nanotubes, *Carbon.* 33 (1995) 883-891.
- ⁵⁴ J.W.G. Wildöer, L.C. Venema, A.G. Rinzler, R.E. Smalley, C. Dekker, Electronic structure of atomically resolved carbon nanotubes, *Nature.* 391 (1998) 59.
- ⁵⁵ G. Seol, Y. Yoon, J.K. Fodor, J. Guo, A. Matsudaira, D. Kienle, et al., CNTbands, (2006). DOI: 10254/nanohub-r1838.7
- ⁵⁶ L. Van Hove, The occurrence of singularities in the elastic frequency distribution of a crystal, *Phys. Rev.* 89 (1953) 1189-1193.
- ⁵⁷ H. Kataura, Y. Kumazawa, Y. Maniwa, I. Umezū, S. Suzuki, Y. Ohtsuka, et al., Optical properties of single-wall carbon nanotubes, *Synthetic Metals.* 103 (1999) 2555-2558.
- ⁵⁸ V. Zólyomi, J. Kürti, First-principles calculations for the electronic band structures of small diameter single-wall carbon nanotubes, *Phys. Rev. B.* 70 (2004) 085403.
- ⁵⁹ J. Kürti, V. Zólyomi, M. Kertész, G. Sun, R.H. Baughman, H. Kuzmany, Individualities and average behavior in the physical properties of small diameter single-walled carbon nanotubes, *Carbon.* 42 (2004) 971-978.
- ⁶⁰ S. Iijima, T. Ichihashi, Single-shell carbon nanotubes of 1-nm diameter, *Nature.* 363 (1993) 603-605.
- ⁶¹ D.S. Bethune, C.H. Klang, M.S. de Vries, G. Gorman, R. Savoy, J. Vazquez, et al., Cobalt-catalysed growth of carbon nanotubes with single-atomic-layer walls, *Nature.* 363 (1993) 605-607.
- ⁶² J.-C. Charlier, J.-P. Michenaud, Energetics of multilayered carbon tubules, *Phys. Rev. Lett.* 70 (1993) 1858-1861.
- ⁶³ P. Nemes-Incze, N.S. Daróczy, Z. Sárközy, A.A. Koós, K. Kertész, O. Tipriğan, et al., Synthesis of bamboo-structured multiwalled carbon nanotubes by spray pyrolysis method, using a mixture of benzene and pyridine, *J. Optoelectron. Adv. M.* 9 (2007) 1525 - 1529.

-
- ⁶⁴ A. Darabont, P. Nemes-Incze, K. Kertész, L. Tapasztó, A.A. Koós, Z. Osváth, et al., Synthesis of carbon nanotubes by spray pyrolysis and their investigation by electron microscopy, *J. Optoelectron. Adv. M.* 7 (2005) 631 - 636.
- ⁶⁵ T. Guo, P. Nikolaev, A.G. Rinzler, D. Tomanek, D.T. Colbert, R.E. Smalley, Self-Assembly of Tubular Fullerenes, *J. Phys. Chem.* 99 (1995) 10694-10697.
- ⁶⁶ T. Guo, P. Nikolaev, A. Thess, D.T. Colbert, R.E. Smalley, Catalytic growth of single-walled nanotubes by laser vaporization, *Chemical Physics Letters.* 243 (1995) 49-54.
- ⁶⁷ T. Baird, J.R. Fryer, B. Grant, Structure of fibrous carbon., *Nature.* 233 (1971) 329-30.
- ⁶⁸ M. Jose-Yacaman, M. Miki-Yoshida, L. Rendon, J.G. Santiesteban, Catalytic growth of carbon microtubules with fullerene structure, *Applied Physics Letters.* 62 (1993) 202-204.
- ⁶⁹ Y. Yao, C. Feng, J. Zhang, Z. Liu, "Cloning" of single-walled carbon nanotubes via open-end growth mechanism., *Nano Lett.* 9 (2009) 1673-7.
- ⁷⁰ Z. Ghorannevis, T. Kato, T. Kaneko, R. Hatakeyama, Narrow-chirality distributed single-walled carbon nanotube growth from nonmagnetic catalyst., *J. Am. Chem. Soc.* 132 (2010) 9570-2.
- ⁷¹ W. Zhou, L. Ding, S. Yang, J. Liu, Synthesis of High Density, Large-Diameter and Aligned Single-Walled Carbon Nanotubes by Multiple-Cycle Growth Methods., *ACS Nano.* (2011).
- ⁷² K. Hata, D.N. Futaba, K. Mizuno, T. Namai, M. Yumura, S. Iijima, Water-Assisted Highly Efficient Synthesis of Impurity-Free Single-Walled Carbon Nanotubes, *Science.* 306 (2004) 1362-1364.
- ⁷³ B.H. Hong, J.Y. Lee, T. Beetz, Y. Zhu, P. Kim, K.S. Kim, Quasi-continuous growth of ultralong carbon nanotube arrays., *J. Am. Chem. Soc.* 127 (2005) 15336-7.
- ⁷⁴ M. Terrones, A. Jorio, M. Endo, A.M. Rao, Y.A. Kim, T. Hayashi, et al., New direction in nanotube science, *Mater. Today.* 7 (2004) 30-45.
- ⁷⁵ A. Fonseca, K. Hernadi, P. Piedigrosso, J.-F. Colomer, K. Mukhopadhyay, R. Doome, et al., Synthesis of single- and multi-wall carbon nanotubes over supported catalysts, *Applied Physics A: Materials Science & Processing.* 67 (1998) 11-22.
- ⁷⁶ Z. Kónya, I. Vesselenyi, K. Niesz, A. Kukovecz, A. Demortier, A. Fonseca, et al., Large scale production of short functionalized carbon nanotubes, *Chem. Phys. Lett.* 360 (2002) 429-435.
- ⁷⁷ A. Dupuis, The catalyst in the CCVD of carbon nanotubes—a review, *Progress In Materials Science.* 50 (2005) 929-961.
- ⁷⁸ P. Nikolaev, M.J. Bronikowski, R.K. Bradley, F. Rohmund, D.T. Colbert, K.A. Smith, et al., Gas-phase catalytic growth of single-walled carbon nanotubes from carbon monoxide, *Chem. Phys. Lett.* 313 (1999) 91-97.
- ⁷⁹ P. Blake, A.H. Castro Neto, T.J. Booth, E.W. Hill, K.S. Novoselov, D. Jiang, et al., Making graphene visible, *Appl. Phys. Lett.* 91 (2007) 063124.
- ⁸⁰ G.M. Rutter, J.N. Crain, N.P. Guisinger, T. Li, P.N. First, J.A. Stroscio, Scattering and interference in epitaxial graphene., *Science.* 317 (2007) 219-22.

-
- ⁸¹ S. Bae, H. Kim, Y. Lee, X. Xu, J.-S. Park, Y. Zheng, et al., Roll-to-roll production of 30-inch graphene films for transparent electrodes, *Nat. Nanotechnol.* 5 (2010) 574-578.
- ⁸² X. Li, W. Cai, J. An, S. Kim, J. Nah, D. Yang, et al., Large-area synthesis of high-quality and uniform graphene films on copper foils., *Science.* 324 (2009) 1312-4.
- ⁸³ P. Nemes-Incze, K.J. Yoo, L. Tapasztó, G. Dobrik, J. Lábár, Z.E. Horváth, et al., Revealing the grain structure of graphene grown by chemical vapor deposition, *Appl. Phys. Lett.* 99 (2011) 023104.
- ⁸⁴ A.K. Geim, Graphene: status and prospects, *Science.* 324 (2009) 1530-4.
- ⁸⁵ A. Barreiro, M. Lazzeri, J. Moser, F. Mauri, A. Bachtold, Transport Properties of Graphene in the High-Current Limit, *Phys. Rev. Lett.* 103 (2009) 076601.
- ⁸⁶ A. a Balandin, S. Ghosh, W. Bao, I. Calizo, D. Teweldebrhan, F. Miao, et al., Superior thermal conductivity of single-layer graphene., *Nano Lett.* 8 (2008) 902-7.
- ⁸⁷ F. Schwierz, Graphene transistors, *Nat. Nanotechnol.* 5 (2010) 487-496.
- ⁸⁸ Y.-M. Lin, C. Dimitrakopoulos, K.A. Jenkins, D.B. Farmer, H.-Y. Chiu, A. Grill, et al., 100-GHz Transistors from Wafer-Scale Epitaxial Graphene., *Science.* 327 (2010) 662.
- ⁸⁹ R. Sordan, F. Traversi, V. Russo, Logic gates with a single graphene transistor, *Appl. Phys. Lett.* 94 (2009) 073305.
- ⁹⁰ M. Burghard, Electronic and vibrational properties of chemically modified single-wall carbon nanotubes, *Surf. Sci. Rep.* 58 (2005) 1-109.
- ⁹¹ K. Balasubramanian, M. Burghard, Chemically functionalized carbon nanotubes., *Small.* 1 (2005) 180-92.
- ⁹² H. Park, J. Zhao, J.P. Lu, Distinct properties of single-wall carbon nanotubes with monovalent sidewall additions, *Nanotechnology.* 16 (2005) 635-638.
- ⁹³ M.S. Strano, C.A. Dyke, M.L. Usrey, P.W. Barone, M.J. Allen, H. Shan, et al., Electronic structure control of single-walled carbon nanotube functionalization, *Science.* 301 (2003) 1519-22.
- ⁹⁴ H. Hu, B. Zhao, M.A. Hamon, K. Kamaras, M.E. Itkis, R.C. Haddon, Sidewall functionalization of single-walled carbon nanotubes by addition of dichlorocarbene., *J. Am. Chem. Soc.* 125 (2003) 14893-900.
- ⁹⁵ A. López-Bezanilla, F. Triozon, S. Latil, X. Blase, S. Roche, Effect of the chemical functionalization on charge transport in carbon nanotubes at the mesoscopic scale., *Nano Lett.* 9 (2009) 940-4.
- ⁹⁶ E.Y. Li, N. Poilvert, N. Marzari, Switchable Conductance in Functionalized Carbon Nanotubes via Reversible Sidewall Bond Cleavage., *ACS Nano.* (2011).
- ⁹⁷ Z.E. Horváth, A.A. Koós, K. Kertész, G. Molnár, G. Vértesy, M.C. Bein, et al., The role of defects in chemical sensing properties of carbon nanotube films, *Appl. Phys. A.* 93 (2008) 495-504.
- ⁹⁸ K. Keren, R.S. Berman, E. Buchstab, U. Sivan, E. Braun, No Title, *Science.* 302 (2003) 1380–1382.
- ⁹⁹ K. Kamarás, Á. Pekker, B. Botka, H. Hu, S. Niyogi, M.E. Itkis, et al., The effect of nitric acid doping on the optical properties of carbon nanotube films, *Phys. Status Solidi B.* 247 (2010) 2754-2757.

-
- ¹⁰⁰ H. Hu, P. Bhowmik, B. Zhao, M.A. Hamon, M.E. Itkis, R.C. Haddon, Determination of the acidic sites of purified single-walled carbon nanotubes by acid–base titration, *Chem. Phys. Lett.* 345 (2001) 25-28.
- ¹⁰¹ H.F. Bettinger, Experimental and computational investigations of the properties of fluorinated single-walled carbon nanotubes., *Chemphyschem.* 4 (2003) 1283-9.
- ¹⁰² I. Kiricsi, Z. Kónya, K. Niesz, A.A. Koos, L.P. Biró, Synthesis procedures for production of carbon nanotube junctions, in: R. Vajtai, X. Aymerich, L.B. Kish, A. Rubio (Eds.), *Nanotechnology*, SPIE, 2003: pp. 280-287.
- ¹⁰³ Y.-P. Sun, K. Fu, Y. Lin, W. Huang, Functionalized Carbon Nanotubes: Properties and Applications, *Acc. Chem. Res.* 35 (2002) 1096-1104.
- ¹⁰⁴ K. Kamarás, M.E. Itkis, H. Hu, B. Zhao, R.C. Haddon, Covalent bond formation to a carbon nanotube metal, *Science.* 301 (2003) 1501.
- ¹⁰⁵ K. Kudin, H. Bettinger, G. Scuseria, Fluorinated single-wall carbon nanotubes, *Phys. Rev. B.* 63 (2001) 045413.
- ¹⁰⁶ K. Nakada, M. Fujita, G. Dresselhaus, M.S. Dresselhaus, Edge state in graphene ribbons: Nanometer size effect and edge shape dependence, *Phys. Rev. B.* 54 (1996) 17954-17961.
- ¹⁰⁷ M. Ezawa, Peculiar width dependence of the electronic properties of carbon nanoribbons, *Phys. Rev. B.* 73 (2006) 045432.
- ¹⁰⁸ Y. Niimi, T. Matsui, H. Kambara, K. Tagami, M. Tsukada, H. Fukuyama, Scanning tunneling microscopy and spectroscopy studies of graphite edges, *Appl. Surf. Sci.* 241 (2005) 43-48.
- ¹⁰⁹ Y.-W. Son, M.L. Cohen, S.G. Louie, Energy Gaps in Graphene Nanoribbons, *Phys. Rev. Lett.* 97 (2006) 216803.
- ¹¹⁰ Y.-W. Son, M.L. Cohen, S.G. Louie, Half-metallic graphene nanoribbons., *Nature.* 444 (2006) 347-9.
- ¹¹¹ A. Rycerz, J. Tworzydło, C.W.J. Beenakker, Valley filter and valley valve in graphene, *Nat. Phys.* 3 (2007) 172-175.
- ¹¹² Z.F. Wang, Q.W. Shi, Q. Li, X. Wang, J.G. Hou, H. Zheng, et al., Z-shaped graphene nanoribbon quantum dot device, *Appl. Phys. Lett.* 91 (2007) 053109.
- ¹¹³ F. Cervantes-Sodi, G. Csányi, S. Piscanec, A.C. Ferrari, Edge-functionalized and substitutionally doped graphene nanoribbons: Electronic and spin properties, *Phys. Rev. B.* 77 (2008) 165427.
- ¹¹⁴ S.M.-M. Dubois, A. Lopez-Bezanilla, A. Cresti, F. Triozon, B. Biel, J.-C. Charlier, et al., Quantum transport in graphene nanoribbons: effects of edge reconstruction and chemical reactivity, *ACS Nano.* 4 (2010) 1971-6.
- ¹¹⁵ A. Ramasubramaniam, Electronic structure of oxygen-terminated zigzag graphene nanoribbons: A hybrid density functional theory study, *Phys. Rev. B.* 81 (2010) 245413.
- ¹¹⁶ A. Cresti, S. Roche, Range and correlation effects in edge disordered graphene nanoribbons, *New J. Phys.* 11 (2009) 095004.
- ¹¹⁷ A.H. Castro Neto, E.R. Mucciolo, C.H. Lewenkopf, Conductance quantization and transport gaps in disordered graphene nanoribbons, *Phys. Rev. B.* 79 (2009) 075407.
- ¹¹⁸ A. Seitsonen, A. Saitta, T. Wassmann, M. Lazzeri, F. Mauri, Structure and stability of graphene nanoribbons in oxygen, carbon dioxide, water, and ammonia, *Phys. Rev. B.* 82 (2010) 115425.

-
- ¹¹⁹ D. Gunlycke, J. Li, J.W. Mintmire, C.T. White, Edges Bring New Dimension to Graphene Nanoribbons, *Nano Lett.* (2010).
- ¹²⁰ M.Y. Han, B. Özyilmaz, Y. Zhang, P. Kim, Energy Band-Gap Engineering of Graphene Nanoribbons, *Phys. Rev. Lett.* 98 (2007) 206805.
- ¹²¹ M.Y. Han, J.C. Brant, P. Kim, Electron Transport in Disordered Graphene Nanoribbons, *Phys. Rev. Lett.* 104 (2010) 056801.
- ¹²² B. Özyilmaz, P. Jarillo-Herrero, D. Efetov, P. Kim, Electronic transport in locally gated graphene nanoconstrictions, *Appl. Phys. Lett.* 91 (2007) 192107.
- ¹²³ K.A. Ritter, J.W. Lyding, The influence of edge structure on the electronic properties of graphene quantum dots and nanoribbons., *Nat. Mater.* 8 (2009) 235-42.
- ¹²⁴ Y.-M. Lin, V. Perebeinos, Z. Chen, P. Avouris, Electrical observation of subband formation in graphene nanoribbons, *Phys. Rev. B.* 78 (2008) 161409(R).
- ¹²⁵ Y. Zhang, V.W. Brar, C. Girit, A. Zettl, M.F. Crommie, Origin of spatial charge inhomogeneity in graphene, *Nat. Phys.* 5 (2009) 722-726.
- ¹²⁶ P. Gallagher, K. Todd, D. Goldhaber-Gordon, Disorder-induced gap behavior in graphene nanoribbons, *Phys. Rev. B.* 81 (2010) 115409.
- ¹²⁷ C. Casiraghi, A. Hartschuh, H. Qian, S. Piscanec, C. Georgi, A. Fasoli, et al., Raman spectroscopy of graphene edges., *Nano Lett.* 9 (2009) 1433-41.
- ¹²⁸ D. a Areshkin, C.T. White, Building blocks for integrated graphene circuits., *Nano Lett.* 7 (2007) 3253-9.
- ¹²⁹ P. Nemes-Incze, G. Magda, K. Kamarás, L.P. Biró, Crystallographically Selective Nanopatterning of Graphene on SiO₂, *Nano Res.* 3 (2010) 110-116.
- ¹³⁰ D.V. Kosynkin, A.L. Higginbotham, A. Sinitskii, J.R. Lomeda, A. Dimiev, B.K. Price, et al., Longitudinal unzipping of carbon nanotubes to form graphene nanoribbons., *Nature.* 458 (2009) 872-6.
- ¹³¹ L. Jiao, X. Wang, G. Diankov, H. Wang, H. Dai, Facile synthesis of high-quality graphene nanoribbons., *Nat. Nanotechnol.* 5 (2010) 321-325.
- ¹³² P. Nemes-Incze, Z. Kónya, I. Kiricsi, A. Pekker, Z.E. Horváth, K. Kamarás, et al., Mapping of Functionalized Regions on Carbon Nanotubes by Scanning Tunneling Microscopy, *J. Phys. Chem. C.* 115 (2011) 3229–3235.
- ¹³³ L.C. Campos, V.R. Manfrinato, J.D. Sanchez-Yamagishi, J. Kong, P. Jarillo-Herrero, Anisotropic etching and nanoribbon formation in single-layer graphene., *Nano Lett.* 9 (2009) 2600-4.
- ¹³⁴ L. Ci, Z. Xu, L. Wang, W. Gao, F. Ding, K.F. Kelly, et al., Controlled nanocutting of graphene, *Nano Res.* 1 (2008) 116-122.
- ¹³⁵ L. Tapasztó, G. Dobrik, P. Lambin, L.P. Biró, Tailoring the atomic structure of graphene nanoribbons by scanning tunnelling microscope lithography., *Nat. Nanotechnol.* 3 (2008) 397-401.
- ¹³⁶ J. Cai, P. Ruffieux, R. Jaafar, M. Bieri, T. Braun, S. Blankenburg, et al., Atomically precise bottom-up fabrication of graphene nanoribbons, *Nature.* 466 (2010) 470-473.

-
- ¹³⁷ L.P. Biró, P. Nemes-Incze, P. Lambin, Graphene: nanoscale processing and recent applications., *Nanoscale*. 4 (2012) 1824-39.
- ¹³⁸ G. Binnig, H. Rohrer, C. Gerber, E. Weibel, Surface studies by scanning tunneling microscopy, *Phys. Rev. Lett.* 49 (1982) 57-61.
- ¹³⁹ N.D. Lang, Spectroscopy of single atoms in the scanning tunneling microscope, *Phys. Rev. B*. 34 (1986) 5947-5950.
- ¹⁴⁰ J. Tersoff, D.R. Hamann, Theory of the scanning tunneling microscope, *Phys. Rev. B*. 31 (1985) 805-813.
- ¹⁴¹ T.O. Wehling, I. Grigorenko, A.I. Lichtenstein, A.V. Balatsky, Phonon mediated tunneling into graphene, *Phys. Rev. Lett.* 101 (2008) 216803.
- ¹⁴² G. Binnig, C.F. Quate, C. Gerber, Atomic Force Microscope, *Phys. Rev. Lett.* 56 (1986) 930-933.
- ¹⁴³ R. García, R. Pérez, Dynamic atomic force microscopy methods, *Surface Science Reports*. 47 (2002) 197-301.
- ¹⁴⁴ P. Nemes-Incze, Z. Osváth, K. Kamarás, L.P. Biró, Anomalies in thickness measurements of graphene and few layer graphite crystals by tapping mode atomic force microscopy, *Carbon*. 46 (2008) 1435-1442.
- ¹⁴⁵ B. Krauss, P. Nemes-Incze, V. Skakalova, L.P. Biró, K.V. Klitzing, J.H. Smet, Raman Scattering at Pure Graphene Zigzag Edges., *Nano Lett.* 10 (2010) 4544-4548.
- ¹⁴⁶ S. Curran, D.L. Carroll, P.M. Ajayan, P. Redlich, S. Roth, M. Rühle, et al., Picking Needles from Nano-Haystacks, *Adv. Mater.* 10 (1998) 311-313.
- ¹⁴⁷ L.P. Biró, J. Gyulai, P. Lambin, J. B.Nagy, S. Lazarescu, G.I. Márk, et al., Scanning tunnelling microscopy (STM) imaging of carbon nanotubes, *Carbon*. 36 (1998) 689-696.
- ¹⁴⁸ L. Zhang, J. Zhang, N. Schmandt, J. Cratty, V.N. Khabashesku, K.F. Kelly, et al., AFM and STM characterization of thiol and thiophene functionalized SWNTs: pitfalls in the use of chemical markers to determine the extent of sidewall functionalization in SWNTs., *Chem. Commun.* (2005) 5429-31.
- ¹⁴⁹ J. Zhang, L. Zhang, V.N. Khabashesku, A.R. Barron, K.F. Kelly, Self-assembly of Sidewall Functionalized Single-walled Carbon Nanotubes Investigated by Scanning Tunneling Microscopy, *J. Phys. Chem. C*. 112 (2008) 12321-12325.
- ¹⁵⁰ Z. Osváth, A.A. Koós, N. Grobert, Z. Vértesy, Z.E. Horváth, L.P. Biró, Scanning Tunneling Microscopy and Spectroscopy of Nitrogen Doped Multi-Walled Carbon Nanotubes Produced by the Pyrolysis of Ferrocene and Benzylamine, *J. Nanosci. Nanotechnol.* 9 (2009) 6139-6143.
- ¹⁵¹ P. Nemes-Incze, L. Tapasztó, A. Darabont, P. Lambin, L.P. Biró, Scanning tunneling microscopy observation of circular electronic superstructures on multiwalled carbon nanotubes functionalised by nitric acid, *Carbon*. 47 (2009) 764-768.
- ¹⁵² R. Graupner, J. Abraham, D. Wunderlich, A. Vencelová, P. Lauffer, J. Röhl, et al., Nucleophilic-alkylation-reoxidation: a functionalization sequence for single-wall carbon nanotubes, *J. Am. Chem. Soc.* 128 (2006) 6683-9.
- ¹⁵³ D. Bonifazi, C. Nacci, R. Marega, S. Campidelli, G. Ceballos, S. Modesti, et al., Microscopic and spectroscopic characterization of paintbrush-like single-walled carbon nanotubes., *Nano Lett.* 6 (2006) 1408-14.

-
- ¹⁵⁴ P. Lauffer, A. Jung, R. Graupner, A. Hirsch, L. Ley, Functionalization of single-walled carbon nanotubes by aromatic molecules studied by scanning tunneling microscopy, *Phys. Status Solidi B.* 243 (2006) 3213-3216.
- ¹⁵⁵ K.F. Kelly, I.W. Chiang, E.T. Mickelson, R.H. Hauge, J.L. Margrave, X. Wang, et al., Insight into the mechanism of sidewall functionalization of single-walled nanotubes: an STM study, *Chem. Phys. Lett.* 313 (1999) 445-450.
- ¹⁵⁶ M. Shiraishi, M. Ata, Work function of carbon nanotubes, *Carbon.* 39 (2001) 1913-1917.
- ¹⁵⁷ I. Willems, Z. Konya, J.F. Colomer, G.V. Tendeloo, N. Nagaraju, A. Fonseca, et al., Control of the outer diameter of thin carbon nanotubes synthesized by catalytic decomposition of hydrocarbons, *Chem. Phys. Lett.* 317 (2000) 71-76.
- ¹⁵⁸ K. Hernadi, A. Fonseca, J.B. Nagy, D. Bemaerts, A. Fudala, A.A. Lucas, Catalytic synthesis of carbon nanotubes using zeolite support, *Zeolites.* 17 (1996) 416-423.
- ¹⁵⁹ M. Monthieux, B.W. Smith, B. Burtiaux, A. Claye, J.E. Fischer, D.E. Luzzi, Sensitivity of single-wall carbon nanotubes to chemical processing: an electron microscopy investigation, *Carbon.* 39 (2001) 1251-1272.
- ¹⁶⁰ W. Zhou, J. Vavro, N. Nemes, J. Fischer, F. Borondics, K. Kamarás, et al., Charge transfer and Fermi level shift in p-doped single-walled carbon nanotubes, *Phys. Rev. B.* 71 (2005) 205423.
- ¹⁶¹ W.C. Forsman, F.L. Vogel, D.E. Carl, J. Hoffman, Chemistry of graphite intercalation by nitric acid, *Carbon.* 16 (1978) 269-271.
- ¹⁶² A.C. Ferrari, Raman spectroscopy of graphene and graphite: Disorder, electron-phonon coupling, doping and nonadiabatic effects, *Solid State Commun.* 143 (2007) 47-57.
- ¹⁶³ M.S. Dresselhaus, A. Jorio, A.G. Souza Filho, R. Saito, Defect characterization in graphene and carbon nanotubes using Raman spectroscopy, *Phil. Trans. R. Soc. A.* 368 (2010) 5355-5377.
- ¹⁶⁴ N.M. Pugno, Graded cross-links for stronger nanomaterials, *Mater. Today.* 13 (2010) 40-43.
- ¹⁶⁵ S.I. Cha, K.T. Kim, K.H. Lee, C.B. Mo, Y.J. Jeong, S.H. Hong, Mechanical and electrical properties of cross-linked carbon nanotubes, *Carbon.* 46 (2008) 482-488.
- ¹⁶⁶ P.W. Chiu, G.S. Duesberg, U. Dettlaff-Weglikowska, S. Roth, Interconnection of carbon nanotubes by chemical functionalization, *Appl. Phys. Lett.* 80 (2002) 3811.
- ¹⁶⁷ S. Hügler, R. Egger, van Hove singularities in disordered multichannel quantum wires and nanotubes, *Phys. Rev. B.* 66 (2002) 193311.
- ¹⁶⁸ L. Tapasztó, P. Nemes-Incze, Z. Osváth, A. Darabont, P. Lambin, L.P. Biró, Electron scattering in a multiwall carbon nanotube bend junction studied by scanning tunneling microscopy, *Phys. Rev. B.* 74 (2006) 235422.
- ¹⁶⁹ M.C. Paiva, W. Xu, M. Fernanda Proença, R.M. Novais, E. Lægsgaard, F. Besenbacher, Unzipping of Functionalized Multiwall Carbon Nanotubes Induced by STM, *Nano Lett.* (2010) 1764-1768.
- ¹⁷⁰ S. Fujii, T. Enoki, Cutting of oxidized graphene into nanosized pieces., *J. Am. Chem. Soc.* 132 (2010) 10034-41.
- ¹⁷¹ O.P. Behrend, F. Oulevey, D. Gourdon, E. Dupas, A.J. Kulik, G. Gremaud, et al., Intermittent contact: tapping or hammering?, *Appl. Phys. A.* 66 (1998) S219-S221.

-
- ¹⁷² R. García, A. San Paulo, Dynamics of a vibrating tip near or in intermittent contact with a surface, *Phys. Rev. B.* 61 (2000) R13381-R13384.
- ¹⁷³ A. Kühle, A.H. Sørensen, J.B. Zandbergen, J. Bohr, Contrast artifacts in tapping tip atomic force microscopy, *Appl. Phys. A.* 66 (1998) S329-S332.
- ¹⁷⁴ A. Gupta, G. Chen, P. Joshi, S. Tadigadapa, P.C. Eklund, Raman scattering from high-frequency phonons in supported n-graphene layer films., *Nano Letters.* 6 (2006) 2667-73.
- ¹⁷⁵ Z. Chen, Y.-M. Lin, M.J. Rooks, P. Avouris, Graphene nano-ribbon electronics, *Physica E.* 40 (2007) 228-232.
- ¹⁷⁶ A.N. Sidorov, M.M. Yazdanpanah, R. Jalilian, P.J. Ouseph, R.W. Cohn, G.U. Sumanasekera, Electrostatic deposition of graphene, *Nanotechnology.* 18 (2007) 135301.
- ¹⁷⁷ D. Graf, F. Molitor, K. Ensslin, C. Stampfer, A. Jungen, C. Hierold, et al., Spatially Resolved Raman Spectroscopy of Single- and Few-Layer Graphene, *Nano Lett.* 7 (2007) 238-242.
- ¹⁷⁸ Á. Mechler, J. Kopniczky, J. Kokavecz, A. Hoel, C.-G. Granqvist, P. Heszler, Anomalies in nanostructure size measurements by AFM, *Phys. Rev. B.* 72 (2005) 125407.
- ¹⁷⁹ Á. Mechler, J. Kokavecz, P. Heszler, R. Lal, Surface energy maps of nanostructures: Atomic force microscopy and numerical simulation study, *Appl. Phys. Lett.* 82 (2003) 3740.
- ¹⁸⁰ C. Casiraghi, A. Hartschuh, E. Lidorikis, H. Qian, H. Harutyunyan, T. Gokus, et al., Rayleigh imaging of graphene and graphene layers, *Nano Lett.* 7 (2007) 2711-7.
- ¹⁸¹ S. Stankovich, S. Watcharotone, M. Hausner, Simple Approach for High-Contrast Optical Imaging and Characterization of Graphene-Based Sheets, *Nano Lett.* 7 (2007) 3569-3575.
- ¹⁸² B. Anczykowski, D. Krüger, K.L. Babcock, H. Fuchs, Basic properties of dynamic force spectroscopy with the scanning force microscope in experiment and simulation, *Ultramicroscopy.* 66 (1996) 251-259.
- ¹⁸³ R. García, A. San Paulo, Attractive and repulsive tip-sample interaction regimes in tapping-mode atomic force microscopy, *Phys. Rev. B.* 60 (1999) 4961-4967.
- ¹⁸⁴ A. Kühle, A.H. Sørensen, J. Bohr, Role of attractive forces in tapping tip force microscopy, *J. Appl. Phys.* 81 (1997) 6562-6569.
- ¹⁸⁵ A. Raman, J. Melcher, R. Tung, Cantilever dynamics in atomic force microscopy, *Nano Today.* 3 (2008) 20-27.
- ¹⁸⁶ H. Butt, B. Cappella, M. Kappl, Force measurements with the atomic force microscope: Technique, interpretation and applications, *Surface Science Reports.* 59 (2005) 1-152.
- ¹⁸⁷ L. Xu, A. Lio, J. Hu, D.F. Ogletree, M. Salmeron, Wetting and Capillary Phenomena of Water on Mica, *J. Phys. Chem. B.* 102 (1998) 540-548.
- ¹⁸⁸ L. Zitzler, S. Herminghaus, F. Mugele, Capillary forces in tapping mode atomic force microscopy, *Phys. Rev. B.* 66 (2002) 155436.
- ¹⁸⁹ B.V. Derjaguin, V.M. Muller, V.P. Toporov, Effect of contact deformations on the adhesion of particles, *Journal Of Colloid and Interface Science.* 53 (1975) 314-326.

-
- ¹⁹⁰ A. Verdager, C. Weis, G. Oncins, G. Ketteler, H. Bluhm, M. Salmeron, Growth and structure of water on SiO₂ films on Si Investigated by Kelvin probe microscopy and in Situ X-ray spectroscopies., *Langmuir*. 23 (2007) 9699-703.
- ¹⁹¹ K. Xu, P. Cao, J.R. Heath, Graphene Visualizes the First Water Adlayers on Mica at Ambient Conditions, *Science*. 329 (2010) 1188-1191.
- ¹⁹² Q. Ouyang, K. Ishida, K. Okada, Investigation of micro-adhesion by atomic force microscopy, *Appl. Surf. Sci.* 169-170 (2001) 644-648.
- ¹⁹³ J. Moser, A. Verdager, D. Jiménez, A. Barreiro, A. Bachtold, The environment of graphene probed by electrostatic force microscopy, *Appl. Phys. Lett.* 92 (2008) 123507.
- ¹⁹⁴ C.D. Willett, M.J. Adams, S.A. Johnson, J.P.K. Seville, Capillary Bridges between Two Spherical Bodies, *Langmuir*. 16 (2000) 9396-9405.
- ¹⁹⁵ J.N. Israelachvili, Intermolecular and surface forces, Second ed, Academic Press, 1992.
- ¹⁹⁶ A. Ferrari, J. Meyer, V. Scardaci, C. Casiraghi, M. Lazzeri, F. Mauri, et al., Raman Spectrum of Graphene and Graphene Layers, *Phys. Rev. Lett.* 97 (2006) 187401.
- ¹⁹⁷ S. Reich, C. Thomsen, Raman spectroscopy of graphite., *Phil. Trans. R. Soc. A.* 362 (2004) 2271-88.
- ¹⁹⁸ R. Sharma, N. Nair, M.S. Strano, Structure–Reactivity Relationships for Graphene Nanoribbons, *J. Phys. Chem. C*. 113 (2009) 14771-7.
- ¹⁹⁹ D.-en Jiang, B.G. Sumpter, S. Dai, Unique chemical reactivity of a graphene nanoribbon’s zigzag edge, *J. Chem. Phys.* 126 (2007) 134701.
- ²⁰⁰ P. Koskinen, S. Malola, H. Häkkinen, Self-Passivating Edge Reconstructions of Graphene, *Phys. Rev. Lett.* 101 (2008) 115502.
- ²⁰¹ S. Konishi, W. Sugimoto, Y. Murakami, Y. Takasu, Catalytic creation of channels in the surface layers of highly oriented pyrolytic graphite by cobalt nanoparticles, *Carbon*. 44 (2006) 2338-40.
- ²⁰² D. Tandon, E.J. Hippo, H. Marsh, E. Sebok, Surface topography of oxidized HOPG by scanning tunneling microscopy, *Carbon*. 35 (1997) 35-44.
- ²⁰³ L. Liu, S. Ryu, M.R. Tomasik, E. Stolyarova, N. Jung, M.S. Hybertsen, et al., Graphene oxidation: thickness-dependent etching and strong chemical doping, *Nano Lett.* 8 (2008) 1965-70.
- ²⁰⁴ J.R. Hahn, Kinetic study of graphite oxidation along two lattice directions, *Carbon*. 43 (2005) 1506-1511.
- ²⁰⁵ J.M. Carlsson, F. Hanke, S. Linic, M. Scheffler, Two-Step Mechanism for Low-Temperature Oxidation of Vacancies in Graphene, *Phys. Rev. Lett.* 102 (2009) 166104.
- ²⁰⁶ V. Geringer, M. Liebmann, T. Echtermeyer, S. Runte, M. Schmidt, R. Rückamp, et al., Intrinsic and extrinsic corrugation of monolayer graphene deposited on SiO₂, *Phys. Rev. Lett.* 102 (2009) 076102.
- ²⁰⁷ R. Koc, S.V. Cattamanchi, Synthesis of beta silicon carbide powders using carbon coated fumed silica, *J. Mat. Sci.* 33 (1998) 2537-2549.
- ²⁰⁸ H.R. Byon, H.C. Choi, Carbon nanotube guided formation of silicon oxide nanotrenches., *Nat. Nanotechnol.* 2 (2007) 162-6.

-
- ²⁰⁹ C.Ö. Girit, A. Zettl, Soldering to a single atomic layer, *Appl. Phys. Lett.* 91 (2007) 193512.
- ²¹⁰ L. Tapasztó, G. Dobrik, P. Nemes-Incze, G. Vertesy, P. Lambin, L.P. Biró, Tuning the electronic structure of graphene by ion irradiation, *Phys. Rev. B.* 78 (2008) 233407.
- ²¹¹ A. Das, S. Pisana, B. Chakraborty, S. Piscanec, S.K. Saha, U.V. Waghmare, et al., Monitoring dopants by Raman scattering in an electrochemically top-gated graphene transistor., *Nat. Nanotechnol.* 3 (2008) 210-5.
- ²¹² K. Bolotin, Y.-W. Tan, Y. Zhang, Y. Zhao, S. Adam, E.H. Hwang, et al., Measurement of Scattering Rate and Minimum Conductivity in Graphene, *Phys. Rev. Lett.* 99 (2007) 246803.
- ²¹³ Z. Cheng, Q. Zhou, C. Wang, Q. Li, C. Wang, Y. Fang, Toward Intrinsic Graphene Surfaces: A Systematic Study on Thermal Annealing and Wet-Chemical Treatment of SiO₂ -Supported Graphene Devices, *Nano Lett.* (2011).
- ²¹⁴ C.-C. Chen, W. Bao, J. Theiss, C. Dames, C.N. Lau, S.B. Cronin, Raman Spectroscopy of Ripple Formation in Suspended Graphene., *Nano Lett.* 9 (2009) 4172-6.
- ²¹⁵ K.S. Novoselov, G. Tsoukleri, J. Parthenios, K. Papagelis, R. Jalil, A.C. Ferrari, et al., Subjecting a graphene monolayer to tension and compression., *Small.* 5 (2009) 2397-402.
- ²¹⁶ L.G. Cançado, M.A. Pimenta, B.R.A. Neves, M.S.S. Dantas, A. Jorio, Influence of the Atomic Structure on the Raman Spectra of Graphite Edges, *Phys. Rev. Lett.* 93 (2004) 247401.
- ²¹⁷ A.K. Gupta, T.J. Russin, H.R. Gutiérrez, P.C. Eklund, Probing graphene edges via Raman scattering., *ACS Nano.* 3 (2009) 45-52.